

# **Fatigue Life Assessment of Sandwich Composite Hulls under Repeated Slamming Loads**

by

Andres Cecchini Brigi

A dissertation submitted in partial fulfillment of the requirements for the degree of

DOCTOR OF PHILOSOPHY  
in  
CIVIL ENGINEERING

UNIVERSITY OF PUERTO RICO  
MAYAGÜEZ CAMPUS  
2014

Approved by:

---

David Serrano, ScD  
President, Graduate Committee

---

Date

---

Frederick Just, PhD  
Member, Graduate Committee

---

Date

---

Luis E. Suárez, PhD  
Member, Graduate Committee

---

Date

---

Ricardo R. López , PhD  
Member, Graduate Committee

---

Date

---

Víctor A. Huérfano, PhD  
Representative of Graduate Studies

---

Date

---

Ismael Pagán Trinidad, Prof.  
Chairperson of the Department

---

Date

## ABSTRACT

Slamming loads induced by waves on ships can cause severe damages on structural members which may compromise integrity and safety. Therefore, better understanding of the slamming problem is a topic of interest in marine applications. In addition, sandwich composite structures are being widely used in the marine industry due to their extremely high flexural stiffness and light weight. This thesis presents a novel predictive computational technique for fatigue life assessment of sandwich composite hulls subject to repeated slamming loads. The slamming modeling was approached in the framework of the two dimensional water entry problem, in which, the fluid is assumed ideal and potential, the angle of incidence between the fluid and the structure is small and gravitational effects are neglected. Numerical models based on explicit finite element analysis (FEA) were developed in LS-DYNA to simulate a single impact event. The multimaterial Arbitrary-Lagrangian-Eulerian (ALE) formulation and the Eulerian-Lagrangian penalty coupling algorithm were used. Initially, the study focused on the impact of rigid hulls with constant velocity. Pressure distribution on the contact surface was investigated and compared with analytical solutions and experimental data. Later, the analysis was extended to include metallic and sandwich composite hulls. As a result, stress time histories for a single impact were obtained at critical locations. To simulate the effect of multiple impacts, these stresses were extrapolated using Peak Over Threshold (POT) analysis assuming a gamma distribution for the exceedances. Then, the Rainflow cycle counting method was used to reduce the complex slamming stresses to a series of simple cyclic stresses. For each stress level, the degree of damage induced in the structure was calculated from the S-N curves and the individual contributions were combined using a damage accumulation model. For metallic hulls, linear Miner's rule was used. For sandwich composite hulls two damage models were investigated: Miner's rule, based on number of cycles, and the non-linear stiffness degradation approach, based on reduction of fatigue (shear) modulus. The selection of damage accumulation models was based on the predominant mode of failure of the structure's material. As a result of this study, it was found that sandwich composite hulls are more susceptible to fatigue failure due to slamming loads than steel hulls. Fatigue life of sandwich hulls was limited by the high shear stresses in the core.

## **RESUMEN**

Las fuerzas producidas por el impacto de olas en embarcaciones pueden causar daños severos en componentes estructurales comprometiendo la integridad y la seguridad de la misma. Por lo tanto conocer el comportamiento de estas fuerzas es muy importante en aplicaciones marinas. Además, las estructuras de materiales compuestos tipo sándwich están siendo ampliamente usadas en la actualidad en aplicaciones marinas debido a su alta rigidez a la flexión y a su bajo peso. En esta tesis se presenta una nueva metodología de predicción numérica de vida de fatiga de cascos de embarcaciones hechos de materiales compuestos tipo sándwich bajo la acción de cargas de impacto hidrodinámico repetitivas. El problema se modeló en base al método de entrada de cuerpos en agua en dos dimensiones. En este método, el fluido se asume ideal y potencial, el ángulo de incidencia entre el agua y el cuerpo es pequeño y se desprecian los efectos gravitacionales. De esta manera, se desarrollaron modelos de elementos finitos usando LS-DYNA con el fin de realizar simulaciones de un solo impacto. Estos modelos incorporaron la formulación multimaterial Arbitrary-Lagrangian-Eulerian (ALE) y el método de contacto ponderado de Euler-Lagrange. En su primera parte, esta tesis se enfoca en el impacto de cascos rígidos en agua con velocidad constante. Se calculó la presión hidrodinámica en la superficie de contacto para varios casos y se comparó con soluciones analíticas y datos experimentales. Luego, el estudio se extendió a cascos metálicos y a cascos tipo sándwich. En estos casos se obtuvieron historiales de esfuerzos en el tiempo para un solo impacto en localizaciones identificadas como críticas. Para considerar el efecto de múltiples impactos, dicho esfuerzos fueron extrapolados usando el método “Peak Over Threshold” (POT) asumiendo que los valores extremos siguen una distribución de probabilidades Gama. Los históricos de esfuerzos extrapolados fueron simplificados a una serie de esfuerzos cíclicos más simples utilizando el método de conteo de ciclos llamado “Rainflow”. Para cada nivel de esfuerzo, se calculó el daño producido en la estructura usando las curvas S-N del material y las contribuciones individuales se combinaron aplicando modelos de acumulación de daño. Para el caso de cascos metálicos, se utilizó la regla de Miner. Para cascos de tipo sándwich, dos modelos diferentes de acumulación de daño fueron considerados: la regla de Miner, basada en el número de ciclos y el método no lineal de degradación de rigidez, el cual se basa en la reducción del módulo de fatiga (corte). La selección de cada modelo se hizo en base al tipo de falla predominante del material del casco. Como resultado de este estudio, se encontró que los cascos hechos de materiales compuestos tipo sándwich son más propensos a falla por fatiga bajo este tipo de cargas que los cascos metálicos. La vida de fatiga de los cascos tipo sándwich está limitada por los altos esfuerzos de corte que se producen en el núcleo.

## **ACKNOWLEDGMENT**

The author wants to thank the ONR Research Program (grant #N000140611043) and Dr. Y.D.S. Rajapakse for the financial support of this investigation. The continuous motivation and encouragement from faculty of the Mechanical Engineering Department at University of Puerto Rico at Mayagüez, in particular Dr. Fred Just and Dr. David Serrano, are gratefully acknowledged. Finally, I want to thank Professor A. Korobkin for his bibliographic contribution to this work.

## TABLE OF CONTENTS

<b>ABSTRACT .....</b>	ii
<b>RESUMEN .....</b>	iii
<b>ACKNOWLEDGMENT .....</b>	iv
<b>LIST OF TABLES .....</b>	vi
<b>LIST OF FIGURES .....</b>	vii
<b>CHAPTER 1. INTRODUCTION .....</b>	1
1.1 BACKGROUND.....	1
1.2 OBJECTIVES AND METHODOLOGY .....	2
<b>CHAPTER 2. LITERATURE REVIEW .....</b>	4
<b>CHAPTER 3. PROBLEM DESCRIPTION .....</b>	7
3.1 RIGID HULL SOLUTION.....	8
3.2 HYDROELASTIC MODELING OF METALLIC HULLS.....	12
3.3 WATER IMPACT OF SANDWICH COMPOSITE HULLS .....	17
<b>CHAPTER 4. FINITE ELEMENT MODELING.....</b>	18
4.1 LAGRANGIAN DESCRIPTION.....	18
4.2 EULERIAN DESCRIPTION .....	20
4.3 GENERAL ALE FORMULATION .....	22
4.3.1 <i>The Operator Splitting</i> .....	23
4.3.2 <i>The Lagrangian Step</i> .....	25
4.3.3 <i>The Eulerian Step</i> .....	27
4.3.4 <i>Fluid-Structure Interaction</i> .....	28
4.4 LS-DYNA MODELS .....	29
<b>CHAPTER 5. FE RESULTS AND DISCUSSION .....</b>	31
5.1 WATER IMPACT OF RIGID HULLS .....	31
5.2 HYDROELASTIC IMPACT OF METALLIC HULLS .....	35
5.2.1 <i>The Impact Stage</i> .....	35
5.2.2 <i>The Penetration Stage</i> .....	42
5.3 HYDROELASTIC IMPACT OF SANDWICH HULLS .....	43
<b>CHAPTER 6. FATIGUE LIFE PREDICTION FOR REPEATED IMPACTS .....</b>	46
6.1 FATIGUE LIFE PREDICTION APPROACH .....	46
6.2 TURNING POINTS SELECTION .....	47
6.3 EXTRAPOLATION ANALYSIS: PEAK OVER THRESHOLD METHOD .....	48
6.4 RAINFLOW CYCLE COUNTING METHOD .....	53
6.5 FATIGUE MODELING: DAMAGE ACCUMULATION APPROACH .....	57
6.5.1 <i>Damage Assessment for Metallic Hulls</i> .....	57
6.5.1.1 <i>Statistical Analysis of Damage Predictions (Linear Model)</i> .....	62
6.5.2 <i>Damage Assessment for Sandwich Composite Hulls</i> .....	63
<b>CHAPTER 7. CONCLUSIONS .....</b>	77
<b>CHAPTER 8. RECOMMENDATIONS .....</b>	80
8.1 SCOPE AND LIMITATIONS OF THE APPROACH .....	80
8.2 PROPOSED FUTURE WORK .....	80
<b>REFERENCES .....</b>	81
<b>APPENDIX A: MATLAB CODES .....</b>	84

## LIST OF TABLES

<b>Table 5.1.</b> Mechanical properties of sandwich composite beams. ....	44
<b>Table 6.1.</b> Absolute stress differences. ....	53
<b>Table 6.2.</b> Rainflow cycles. ....	55
<b>Table 6.3.</b> Constants for S-N curves for various ductile materials. ....	58
<b>Table 6.4.</b> Number of impacts to fatigue failure of metallic hulls. ....	61
<b>Table 6.5.</b> Stiffness degradation parameters. ....	66
<b>Table 6.6.</b> Number of impacts to failure of sandwich hulls. ....	76

## LIST OF FIGURES

<b>Figure 1.1.</b> Slamming on a U.S. Navy war ship.....	1
<b>Figure 1.2.</b> Proposed fatigue life prediction approach. ....	3
<b>Figure 3.1.</b> Definitions used in the problem of hull-water impact. ....	7
<b>Figure 3.2.</b> Wagner's solution: time history of impact pressure. ....	9
<b>Figure 3.3.</b> Wagner's solution: spatial distribution of impact pressure.....	10
<b>Figure 3.4.</b> Wagner's model versus solution of Zhao and Faltinsen. ....	11
<b>Figure 3.5.</b> Hydroelastic modeling of hull-water impact. ....	12
<b>Figure 4.1.</b> Lagrangian or material description. ....	18
<b>Figure 4.2.</b> Eulerian or spatial description. ....	20
<b>Figure 4.3.</b> Split operator. ....	23
<b>Figure 4.4.</b> Split time step into two phases. ....	25
<b>Figure 4.5.</b> Penalty coupling schematic diagram. ....	28
<b>Figure 4.6.</b> Finite element model. ....	29
<b>Figure 4.7.</b> Simplified FE model. ....	30
<b>Figure 5.1.</b> Left: water free surface elevation. Right: water pressure. ....	32
<b>Figure 5.2.</b> Pressure time history at $x = 0.107$ m ( $\beta = 20^\circ$ , $V = 5$ m/s)....	33
<b>Figure 5.3.</b> Pressure time history at $x = 0.111$ m ( $\beta = 10^\circ$ , $V = 5$ m/s)....	34
<b>Figure 5.4.</b> Propagation of the expanding pressure peak. ....	35
<b>Figure 5.5.</b> Left: Water free surface elevation. Right: Hull deflection. ....	36
<b>Figure 5.6.</b> Hull deflection time history ( $\beta = 10^\circ$ , $V = 5$ m/s)....	37
<b>Figure 5.7.</b> Maximum hull deflections. ....	37
<b>Figure 5.8.</b> Time history of the wetted length. ....	38
<b>Figure 5.9.</b> Time history of generalized coordinates.....	39
<b>Figure 5.10.</b> Deflected shapes at initial stages. ....	39
<b>Figure 5.11.</b> Deflected shapes at advanced stages. ....	39
<b>Figure 5.12.</b> Hull deflection time history ( $\beta = 10^\circ$ , $V = 5$ m/s). ....	40
<b>Figure 5.13.</b> Hydrodynamic pressure (impact stage). ....	41
<b>Figure 5.14.</b> Hull deflection for two different mesh densities ( $x = 0.1$ m)....	41
<b>Figure 5.15.</b> Hull deflection including the penetration stage. ....	42
<b>Figure 5.16.</b> Hull stresses including the penetration stage. ....	43
<b>Figure 5.17.</b> FE model of a sandwich composite hull. ....	43
<b>Figure 5.18.</b> a) Water free surface elevation, b) Core shear stresses (time = 5.5 ms).....	44
<b>Figure 5.19.</b> Sandwich hull transversal deflections ( $\zeta$ axis). ....	45
<b>Figure 5.20.</b> Core shear stresses at beam supports. ....	45
<b>Figure 6.1.</b> Fatigue life prediction approach. ....	47
<b>Figure 6.2.</b> Stress time history at mid-span for three impact events. ....	48
<b>Figure 6.3.</b> Selected turning points. ....	48
<b>Figure 6.4.</b> Maximum stress distribution for slam events [25]. ....	49
<b>Figure 6.5.</b> Randomly generated maximum stress distribution.....	50
<b>Figure 6.6.</b> Exceedances above threshold level $u_{\max}$ and below $u_{\min}$ .....	51
<b>Figure 6.7.</b> Distribution of normalized exceedances $Z/\bar{Z}$ for 10,000 impacts. ....	51
<b>Figure 6.8.</b> Original TPs history compared with extrapolated results.....	52
<b>Figure 6.9.</b> Extrapolated TPs time history for 10 impacts. ....	52
<b>Figure 6.10.</b> Extrapolated TPs labels. ....	53
<b>Figure 6.11.</b> Rainflow cycle counting method flow chart. ....	54
<b>Figure 6.12.</b> Rainflow cycles extracted from stress history. ....	55
<b>Figure 6.13.</b> Rainflow matrices for different number of impacts.....	56

<b>Figure 6.14.</b> Damage accumulation MATLAB® code flow chart.....	59
<b>Figure 6.15.</b> Damage accumulation as a function of number of impact .....	60
<b>Figure 6.16.</b> Damage as a function of $u_{\max}$ .....	61
<b>Figure 6.17.</b> Damage Distribution at 849,762 impacts with $u_{\max} = 150$ MPa. ....	62
<b>Figure 6.18.</b> Fatigue modulus definition.....	64
<b>Figure 6.19.</b> Damage accumulation for two stress levels: a) low/high, b) high/low.....	66
<b>Figure 6.20.</b> Fatigue failure and selected location for damage assessment.....	67
<b>Figure 6.21.</b> Damage as a function of number of impacts (Loc. A).....	68
<b>Figure 6.22.</b> Damage as a function of number of impacts (Loc. B).....	69
<b>Figure 6.23.</b> MATLAB® code flow chart.....	70
<b>Figure 6.24.</b> Damage convergence.....	71
<b>Figure 6.25.</b> Damage as a function of number of impacts (Loc. A).....	72
<b>Figure 6.26.</b> Damage as a function of number of impacts (Loc. B).....	73
<b>Figure 6.27.</b> Linear damage predictions (Loc. A).....	74
<b>Figure 6.28.</b> Non-linear damage predictions (Loc. A) .....	74
<b>Figure 6.29.</b> Linear damage predictions (Loc. B) .....	75
<b>Figure 6.30.</b> Non-linear damage predictions (Loc. B) .....	75

## CHAPTER 1. INTRODUCTION

### 1.1 BACKGROUND

Hydrodynamic impacts, “slamming”, are characterized by very high loads of short duration compared to the local dominant period of vibration of the structure. In rough seas, a ship hull may experience repeated impact events which may produce cyclic loading, eventually causing fatigue induced failure of the structure (Figure 1.1). Because of the considerable possibility of this type of structural damage, slamming is a serious concern in the shipbuilding industry. Thus, ship hulls must be strong and stiff enough to carry these loads and still light enough to make the ship efficient in terms of building and operational costs.



**Figure 1.1.** Slamming on a U.S. Navy war ship.

To address this problem, new developments have been made in the design and construction of marine vehicles. One of these new concepts substitutes materials commonly used in ship construction such as steel and aluminum with more sophisticated material configurations. Sandwich composites have been used recently in marine vehicles due to their extremely high flexural stiffness and light weight. But sandwich structures tend to be more flexible than other conventional structures used in vessels which makes dynamic effects such as slamming more pronounced. Therefore, better understanding of the slamming problem on sandwich hulls is a topic of interest in marine applications. Usually, the study of wave slamming on ships has been approached in the framework of the water entry problem. The hydrodynamic analysis of the impact of rigid hulls into water has been widely studied for many years. Several theoretical and numerical models have been developed to predict the interaction forces (pressure)

between fluid and structure during the impact. Many of them are still used by researchers and designers of marine vehicles. Recently, the analysis of water impact has been extended to elastic hulls leading to more complex mathematical models. However this analysis is limited to beam structures with simple boundary conditions. Therefore, water slamming modeling of actual composite structures, in particular of sandwich hulls, is a topic that still requires further investigation. Additionally, damage assessment models for metallic structures subject to arbitrary cyclic excitations have been widely studied for many years and some of them have been implemented in FE codes. The Rainflow cycle counting method combined with linear damage accumulation models (Miner's rule) have demonstrated to produce relatively accurate fatigue life predictions. But for composite materials, life prediction models have just been developed recently and they are currently being validated using numerical simulations and experimental results. Several approaches are still being tested by researchers and there is no consensus regarding the best modeling approach for this problem. Fatigue life assessment on sandwich composite hulls subject to repeated slamming loads have not been included yet in the current literature and it may be critical in the design of marine vehicles.

## 1.2 OBJECTIVES AND METHODOLOGY

The primary purpose of this thesis was to develop a predictive computational technique for fatigue life assessment of sandwich composite hulls subject to repeated slamming loads. To achieve this goal, the following objectives needed to be addressed: 1) The investigation of the physical phenomena that occur in slamming problems. In particular, the interaction forces between fluid and structure during the impact. Several theoretical models have been developed to predict the pressure distribution in the contact region. The current work focused on Wagner's model [2] and the solution proposed by Zhao and Faltinsen [6] for the impact of rigid hulls. The study of slamming on elastic structures was based on hydroelastic models developed by Korobkin [8, 9] which use the normal mode method to approximate the structural deformation; 2) The development and validation of FE models to compute the hydrodynamic loads and structural response (displacements and stresses) of rigid and elastic hulls. Different FE formulations were considered for the modeling of the three main components involved in the problem: the fluid, the structure and the coupling between fluid and structure. According to the Aquelet and Souli [14, 15], the multimaterial Arbitrary-Lagrangian-Eulerian ALE formulation and the penalty based algorithm is the modeling technique that produces the best results. This phase also included the extrapolation of the slamming cycle loading from numerical simulations of a single impact event. This means, to obtain the time history of slamming stresses to which the hull structure will be subject to during its lifetime. This was done by using extreme value theory or Peak Over Threshold (POT) [32] extrapolation analysis and

maximum stress distribution data obtained from slamming measurements on actual high-speed catamarans; 3) The implementation of existing damage accumulation models to predict fatigue life of metallic and sandwich composite hulls. The Rainflow cycle counting method [27] was used to reduce the complex slamming loading to a series of simple cyclic loadings. For each load level, the degree of cumulative damage induced in the structure was calculated from the S-N curves and the individual contributions were combined using the selected damage models. For metallic hulls linear Miner's rule was used while for sandwich hulls both linear and non-linear damage models were investigated. The selection of damage accumulation models was based on the predominant mode of failure of the structure under study; 4) The validation of the proposed fatigue life prediction approach using comparative results from previous published works and experimental tests. The proposed approach is schematically shown in Figure 1.2.

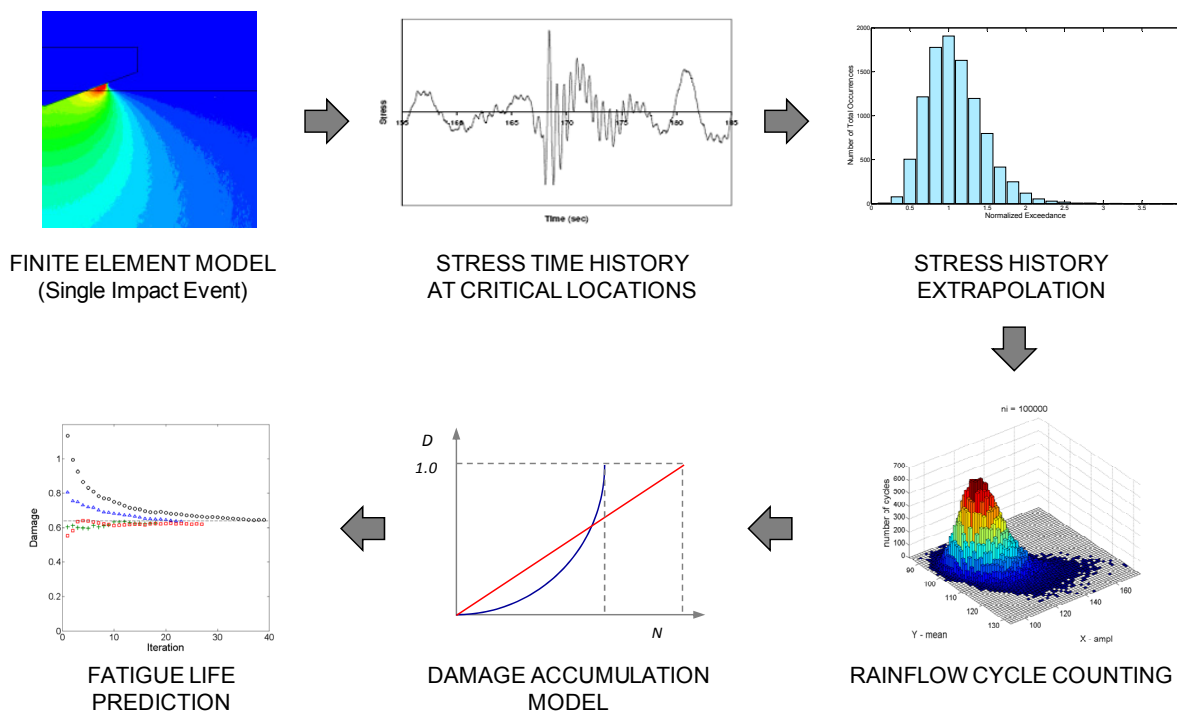


**Figure 1.2.** Proposed fatigue life prediction approach.

## CHAPTER 2. LITERATURE REVIEW

The study of hydrodynamic impacts has been of great interest for structural designers for many years. Information related to water forces occurring during the impact, particularly in the initial stage, is crucial in the design of marine vehicles. Recent investigations have included improvements in theoretical models, advances in experimental techniques and the implementation of numerical methods. The first physical model of the water impact problem was developed by Von Karman [1] to predict the forces on a two dimensional rigid wedge. Von Karman's theory was based on momentum conservation of the water-wedge system and on the concept of added mass. The work assumed that the local water surface elevation during the wedge penetration could be neglected. This unrealistic hypothesis limited the application of Von Karman's model in subsequent work. Wagner's theory, however, took into account the local up-rise of the water by approximating the wetted part of the wedge by an expanding flat plate of the same length [2]. Assuming ideal conditions, the fluid flow was described by a boundary value problem in terms of the complex velocity potential function. The hydrodynamic pressures on the body surface were calculated from Bernoulli's equation neglecting gravitational effects. Wagner's solution predicts an infinite slamming pressure at the edge of the expanding plate, which is physically impossible. In an attempt to solve this singularity, Wagner limited the maximum pressure by truncating his solution in the vicinity of the singular point. Subsequent improvements on Wagner's model included the effect of non linear jet flow in the intersection region between the wedge and the fluid free surface by matching the solution in this region with the expanding plate solution as shown by Dobrovolskaya [3], Watanabe [4], and Cointe [5].

Based on this approach, Zhao and Faltinsen [6] presented a composite solution for the pressure distribution on the body surface. This pressure solution was used in the current thesis as an initial validation of the numerical models of rigid hull impacts. On the other hand, for water impact problems in which structural deformations are significant, the rigid body approximation is no longer valid and the hydroelastic fluid-structure interaction must be considered. Usually, hydroelastic impact models combine the structural analysis with Wagner's theory. The structural analysis can be performed using the finite element method or the normal mode method. In both cases, the problem becomes coupled and non-linear. The hydrodynamic loads on the structure and the structural deformations have to be determined simultaneously, along with the length of the wetted part of the body. The time evolution of the wetted length is an important characteristic of the impact, which strongly affects the magnitude of the loads. The hydroelastic beam model has been used to study wet-deck slamming on catamarans and water entry of elastic wedges by Kvalsvoid [7] and Korobkin [8, 9]. In this model, the structure is represented by elastic

Euler beams and the normal mode method is used to approximate the beam deflection during the impact. This is a relative simple approach to calculate the elastic response of the beam, but for non-homogeneous structures such as composite panels, the normal mode method becomes impractical. In those cases, the structural model needs to be developed based on FE analysis or by composite panel-shell theory as shown by Qin and Batra [10, 37] and by Abrate [39] for the impact of a sandwich composite hull. The FE modeling of water impacts is still a topic of discussion among researchers and engineers which requires further investigation. Many FE codes have been developed to predict the hydrodynamic loads between the fluid and the structure as those by Bereznitski [11] and Korobkin [12]. The role of hydroelasticity has been studied by Bereznitski [13] using a self-developed code and other comercial software. A novel fluid-structure coupling algorithm was designed by Aquelet, Souli, and Olovsson [14, 15 and 16] to manage the interaction forces between an Eulerian and a Lagrangian mesh. A sensitivity study of the solution based on mesh density and selection of penalty coupling algorithm parameters was conducted by Stenius, Rosen, and Kuttenleuler in [17, 40] using the general purpose FE code LS-DYNA [18, 19]. LS-DYNA capabilities include pure Lagrangian, arbitrary Lagrangian-Eulerian (ALE), multimaterial and penalty based contact formulations. These particular modeling approaches have made LS-DYNA the most suitable and used FE code for the study of fluid-structure interaction problems and simulation of hydrodynamic impacts as done by Tutt [20].

The experimental investigation of water impacts has recently become of great interest for validation of FE models and prediction of hydrodynamic pressures and fatigue life as shown by Anghileri [21] and Downs-Honey [22]. Breder [23] conducted an experimental investigation of the slamming pressures on a rigid sandwich panel using a servo hydraulic slam test system which was programmed to work at a constant velocity. Several tests were performed with different deadrise angle and impact velocities. The hydrodynamic pressure, load and vertical displacement of the specimens were measured. In addition, Breder [23] suggested that similar tests should be carried out with elastic panels for more combinations of deadrise angle and impact velocity. Charca [24] performed an experimental program to study damage accumulation and failure in sandwich composites under repeated slamming. The work focused on two different material configurations: 1) carbon fiber-epoxy face sheets and polyester foam filled honeycomb sandwich and 2) carbon fiber-epoxy face sheets and polyurethane foam core sandwich. Different modes of failure were identified for both material configurations, being local core shear the most critical. Thomas [25] investigated the influence of slamming and whipping on the fatigue life of a large high-speed aluminium catamaran in order to optimize the structural design. Full-scale measurements of slam events were taken in a variety of sea conditions. The Rainflow method [26] was used to determine the number of cycles for specific stress ranges from the experimental data. The Rainflow method is a

standardized cycle counting technique as per American Society for Testing Materials (ASTM) [27]. Fatigue life was then estimated based on Miner's linear damage accumulation model [26] which was found to reduce significantly with the presence of slam events. Several life prediction programs have been developed based on the combination of the Rainflow method and Miner's rule for damage assessment of metallic structures. Moreover, some of these programs have been implemented in commercial FE codes like ANSYS [28]. In some cases this life prediction approach has been extended to non-metallic structural components such as NASALife [29] for ceramic matrix fiber-reinforced composites. The effect of fatigue on sandwich materials subjected to slamming loads was studied by Burman, Rosen and Zenkert [38] using actual response measurements on a high-speed vessel to formulate a slam fatigue loading spectrum. However, the use of linear damage accumulation models to predict fatigue life in composite materials is a topic of discussion and requires special attention. Alternatively, non-linear models have been proposed for sandwich composites materials based on strength or stiffness degradation by Sharma [30] and Clark [31]. These models tend to be less conservative than linear models for predicting fatigue life.

The work presented in this thesis is intended to extend the current state of the art in fatigue life prediction of hull structures under slamming loading. It uses a novel approach to extrapolate stress time histories from FE simulations of a single impact event to account for multiple impacts, Johannesson [32]. It also combines the Rainflow cycle counting method with Miner's rule to predict the number of impacts to failure in a steel ship hull. For sandwich composite hulls, fatigue life predictions obtained using Miner's rule are compared with results using the damage accumulation model presented by Clark [31]. Several recommendations are suggested to improve fatigue life of sandwich hulls and particular topics are proposed for future work.

## CHAPTER 3. PROBLEM DESCRIPTION

In this chapter, the two dimensional unsteady problem of a symmetrical hull-water impact is studied. The fluid flow is assumed to be irrotational and incompressible. Viscous and gravitational effects are neglected. The angle of incidence  $\beta$  between the bottom hull and the undisturbed water surface is small ( $5^\circ - 20^\circ$ ) and the impact velocity  $V$  of the body remains constant during the impact and penetration stages. The impact stage is defined as the time it takes the hull length to wet completely. A Cartesian coordinate system  $x-y$  is used to formulate the mathematical problem. The  $x$  axis corresponds to the free water surface at  $t = 0$ , where  $t$  is the time measured from the instant the keel touches the water. The hull section is symmetric about the  $y$  axis (Figure 3.1). During the impact, the water rises up in the vicinity of the intersection points  $|x| = c(t)$ . At these locations, the fluid flow field is divided into two regions: the outer and the inner region. In the outer region,  $|x| < c(t)$ , the fluid flow can be described by the velocity potential function  $\varphi(x,y,t)$  which satisfies the boundary value problem (BVP) in Eqs. (3.1)-(3.4). By definition, the derivative of the velocity potential function along any arbitrary direction  $n$ , gives the fluid velocity component in that direction.

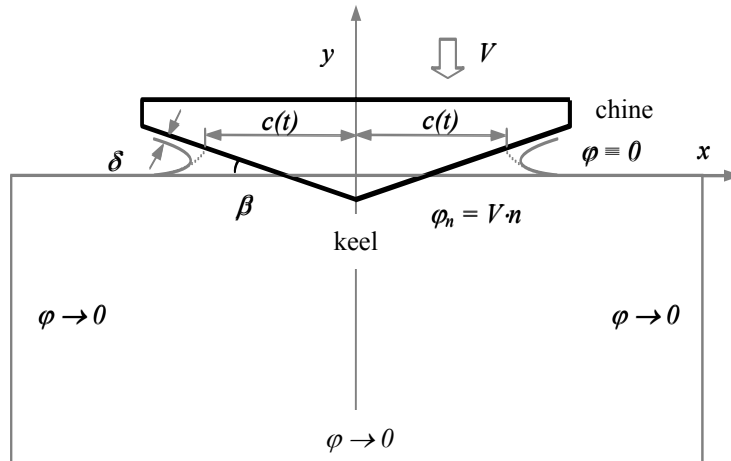


**Figure 3.1.** Definitions used in the problem of hull-water impact.

$$\varphi_{xx} + \varphi_{yy} = 0 \quad (y < 0) \quad (3.1)$$

$$\varphi = 0 \quad (y = 0, |x| > c(t)) \quad (3.2)$$

$$\varphi_n = V \cdot n \quad \text{on the contact surface} \quad (3.3)$$

$$\varphi \rightarrow 0 \quad (x^2 + y^2 \rightarrow \infty) \quad (3.4)$$

The subscripts in Eqs. (3.1) and (3.3) indicate partial derivative. Eq. (3.2) is a consequence of fluid acceleration in the vicinity of the hull dominating over gravitational acceleration during the impact. Fluid particles on the fluid free surface start at initial time with  $\varphi = 0$  and remain in that state for all time. This is because the pressure is assumed to be zero above the water surface and, according to Bernoulli's equation,  $\partial\varphi/\partial t = 0$  at that location. However, the free surface moves because  $\partial\varphi/\partial n \neq 0$ . The contact boundary condition requiring no fluid flow through the bottom hull specifies that Eq. (3.3) must be satisfied for all fluid particles in contact with the body. Where  $n$  is the unit vector normal to the bottom hull surface. Far away from the impact zone ( $x^2+y^2 \rightarrow \infty$ ), the fluid particles remain undisturbed and it can be assumed that the potential function tends to zero, Eq. (3.4). In the inner region,  $|x| > c(t)$ , potential theory is no longer valid due to non linear jet flow effects. For small deadrise angles it is possible to use matched asymptotic expansions to solve the hydrodynamic problem [3, 4 and 5]. An asymptotic formula for the pressure distribution on the body surface is available in [6] which will be used in Chapter 5 to compare with FE results. Notice that BVP (3.1)-(3.4) represents only the hydrodynamic part of the impact problem and does not include the structural formulation. The structural part of the problem is presented in the following sections.

### 3.1 RIGID HULL SOLUTION

If the bottom surface of the hull is assumed to be rigid and the deadrise angle  $\beta$  is small, the body boundary condition (3.3) can be transferred to a horizontal straight line between the coordinates  $x = -c(t)$  and  $x = c(t)$  using the Taylor expansion [2]. This means that the wetted length of the bottom hull is approximated by an expanding flat plate of width  $2c(t)$ . Eq. (3.5) represents the new boundary condition on the contact surface according to Wagner's model.

$$\varphi_y = -V \quad (y=0, |x| < c(t)) \quad (3.5)$$

Since Wagner was mostly interested in the impact pressure on the bottom of the hull, he only focused on the solution of the BVP on the contact surface (Eq. (3.6)). The hydrodynamic pressure is calculated using an approximation of Bernoulli's equation (Eq. (3.7)), where  $\rho_w$  represents the water mass density. The computation of the temporal derivative of Eq. (3.6), assuming a constant impact velocity  $V$ , gives the pressure Eq. (3.8). This pressure is associated with the rate of change of the wetted length  $dc/dt$ . In addition, Wagner derived an approximation to calculate the wetted length of the body surface  $c(t)$ , Eq. (3.9). Note that Wagner's solution predicts an infinite impact pressure at the edges of the expanding plate,

$x = \pm c(t)$ , which is physically impossible. Therefore, Wagner limited the maximum pressure on the body to  $p = p_{max}$  according to Eq. (3.10). This model is only valid in the outer region but it is widely used to represent the hydrodynamic formulation in hydroelastic impact problems.

$$\varphi = -V(c(t)^2 - x^2)^{1/2} \quad y = 0, |x| < c(t) \quad (3.6)$$

$$p = -\rho_w \frac{\partial \varphi}{\partial t} \quad (3.7)$$

$$p = \rho_w V \frac{c(t)}{(c(t)^2 - x^2)^{1/2}} \frac{dc(t)}{dt} \quad (3.8)$$

$$c(t) = \frac{\pi V t}{2 \tan \beta} \quad (3.9)$$

$$p_{max} = \frac{1}{2} \rho_w \left( \frac{dc(t)}{dt} \right)^2 \quad (3.10)$$

Wagner's solution of the impact pressure for a rigid hull (Eq. 3.8 and Eq. 3.9) with length  $L = 0.2$  m, deadrise angle  $\beta = 20^\circ$  and constant velocity  $V = 5$  m/s is shown in Figures 3.2 and 3.3. The temporal evolution of the impact pressure at three different locations on the bottom hull is illustrated in Figure 3.2. The spatial distribution of the pressure when the wetted length coincides with the selected locations is shown in Figure 3.3. The dashed lines correspond to equation (3.8) which goes to infinity at  $x = c(t)$  while the solid lines represent the same solution limited according to equation (3.10).

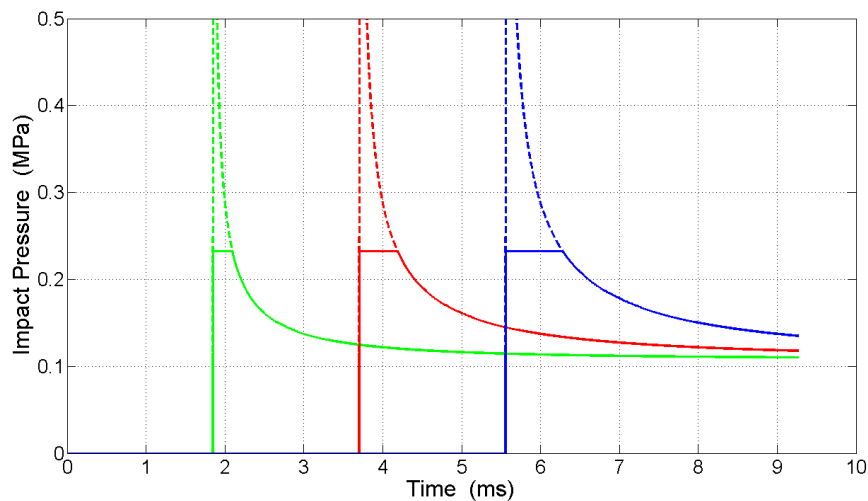


**Figure 3.2.** Wagner's solution: time history of impact pressure.

The local up rise of the water causes the pressure peak to propagate from the keel to the chine of the hull followed by a distinctly lower and relatively uniform pressure. The impact pressure is also characterized by location of the peak and the temporal and spatial extent. In this particular case, the maximum pressure was close to 0.23 MPa and the duration of the impact stage was 9.2 milliseconds (ms) approximately. The width of the pressure peak increases with time and accordingly with the  $x$  coordinate. Therefore, proper numerical modeling of the problem will require higher spatial resolution of the fluid domain close to the initial contact point  $x = 0$ . The pre-knowledge of the theoretical expanding pressure peak will be used in Chapter 4 as guidance to develop FE models.

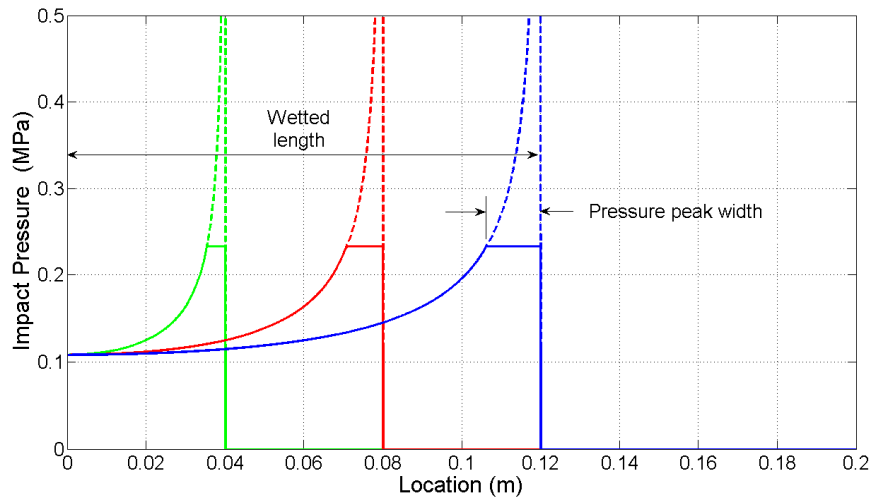


**Figure 3.3.** Wagner's solution: spatial distribution of impact pressure.

Based on Wagner's theory, Zhao and Faltinsen [6] developed a composite solution for the pressure distribution by matching the flow field around the expanding flat plate in the outer region with the flow field around a steady planning plate at an attack angle  $\beta$  in the inner region. According to Zhao and Faltinsen, in the inner region the pressure can be approximated by Eq. (3.11).

$$p_{in} = 2\rho_w \left( \frac{dc}{dt} \right)^2 |\tau|^{1/2} (1 + |\tau|^{1/2})^{-2} \quad (3.11)$$

$$\delta = \frac{\pi c V^2}{8} \left( \frac{dc}{dt} \right)^{-2} \quad (3.12)$$

The jet thickness  $\delta$  obtained by matching the inner and the outer solutions is given in Eq. (3.12). An intermediate variable  $|\tau|$  is related to the spatial coordinate  $x$  by Eq. (3.13). When  $|\tau|$  tends to 0, 1 and  $\infty$ ,  $x$  tends to  $\infty$ ,  $c(t)$  and  $-\infty$  respectively. For large values of  $|\tau|$ , Eq. (3.11) becomes  $2\rho_w(dc/dt)^2|\tau|^{-1/2}$  and Eq. (3.13) become  $-(\delta/\pi)|\tau|$ . For this condition, the pressure Eq. (3.11) can be expressed as Eq. (3.14). The composite solution valid in both the inner and the outer region is obtained by adding Eqs. (3.8) and (3.11) and subtracting Eq. (3.14).

$$x - c = \frac{\delta}{\pi} (\ln |\tau| - 4|\tau|^{1/2} - |\tau| + 5) \quad (3.13)$$

$$p_{in} = \rho_w V c \left( \frac{dc}{dt} \right) [2c(c-x)]^{-1/2} \quad (3.14)$$

$$p = \rho_w V \frac{c}{(c^2 - x^2)^{1/2}} \frac{dc}{dt} + 2\rho_w \left( \frac{dc}{dt} \right)^2 |\tau|^{1/2} (1 + |\tau|^{1/2})^{-2} - \rho_w V c \left( \frac{dc}{dt} \right) [2c(c-x)]^{-1/2} \quad (3.15)$$

The solution given by Eq. (3.15) gives a more realistic behavior of the pressure close to the intersection point (Figure 3.4). This solution will be used in Chapter 5 for comparison with FE results. The hydrodynamic pressure distribution becomes pronouncedly peaked and concentrated for smaller deadrise angles ( $\beta \leq 20^\circ$ ). Additionally, the pressure is directly related to the impact velocity according to Eqs. (3.8) and (3.15).

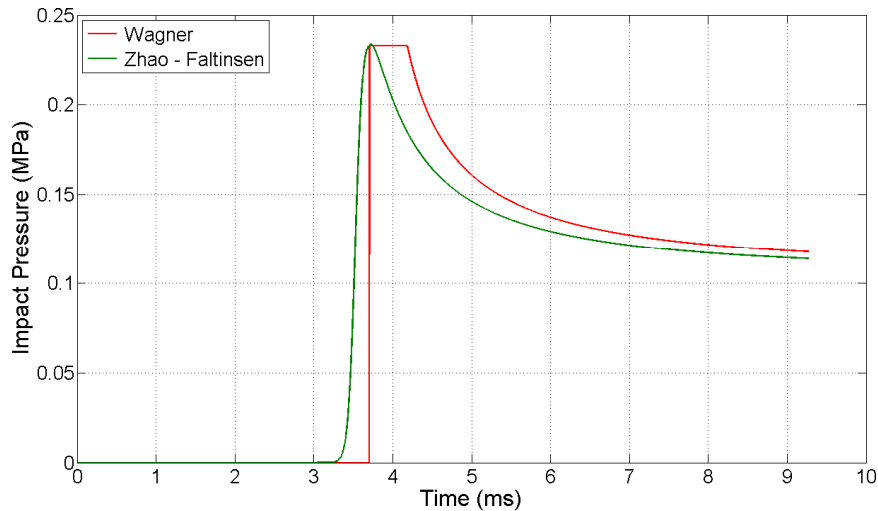


**Figure 3.4.** Wagner's model versus solution of Zhao and Faltinsen.

### 3.2 HYDROELASTIC MODELING OF METALLIC HULLS

The hydroelastic modeling of impact of metallic hulls represents the bottom hull surface as simple supported homogeneous Euler beams (Figure 3.5). The hydrodynamic loads are evaluated with the Wagner approximation. The initial position of each beam is given by the equation  $y = |x| \tan\beta$ , where  $\beta$  is the angle of the un-deformed structure. The beam supports are subjected to a constant downward velocity  $V$ . The transversal deflection of the beams is denoted by  $w(x,t)$ . Thus, the absolute velocity of impact of any point of the beam is  $-V + w_t(x,t)$ , where the subscript  $t$  indicates temporal derivative. Due to the symmetry of the problem with respect to the  $y$  axis, only the right hand side beam is considered,  $x > 0$ . The usual approach of the problem involves the use of non-dimensional variables in the mathematical formulation [8, 9 and 12]. The beam length  $L$  is taken as the length scale and the velocity  $V$  is the velocity scale for fluid particles. If the hull structure were infinite rigid and the water surface were undisturbed during the penetration, the bottom hull would be completely wetted at time  $T = (L/V) \cdot \sin\beta$  and the vertical displacement of the hull would be  $L \cdot \sin\beta$  at this time instant. The time  $T$  is taken as the time scale factor and  $L \cdot \sin\beta$  as the displacement scale factor. The product  $VL$  is the scale factor for the velocity potential and  $\rho_w V^2 / \sin\beta$  is the hydrodynamic pressure scale. Wagner's model in non-dimensional variables is given by the BVP (3.16)-(3.19).

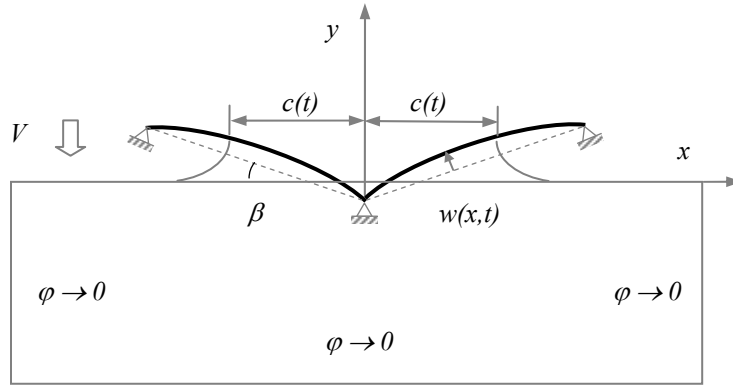


**Figure 3.5.** Hydroelastic modeling of hull-water impact.

$$\varphi_{xx} + \varphi_{yy} = 0 \quad (y < 0) \quad (3.16)$$

$$\varphi = 0 \quad (y = 0, |x| > c(t)) \quad (3.17)$$

$$\varphi_y = -1 + w_t(|x|, t) \quad (y = 0, |x| < c(t)) \quad (3.18)$$

$$\varphi \rightarrow 0 \quad (x^2 + y^2 \rightarrow \infty) \quad (3.19)$$

This BVP is complemented by the equations that govern the beam deflection, Eqs. (3.20)-(3.22). Dots indicate time derivative while Roman numerals indicate derivative with respect to  $x$ . The hydrodynamic pressure  $p(x,t)$  is given by Eq. (3.7). The non-dimensional mass and flexural stiffness are  $m = \rho_b h / \rho_w L$  and  $\alpha = EI \sin^2 \beta / (\rho_w V^2 L^3)$  respectively. Where,  $\rho_b$  is the mass density of the beam,  $h$  is the beam thickness,  $E$  is the elasticity modulus and  $I$  is the moment of inertia of the beam cross section,  $I = h^3/12$ . Eqs. (3.16)-(3.22) describe the coupled problem between fluid hydrodynamic and structural response. This means, that the solution of the BVP (3.16)-(3.19) depends on the temporal derivative of  $w(x,t)$  according to Eq. (3.18), and at the same time, the right hand side term of Eq. (3.20) depends on the velocity potential function.

$$m \ddot{w} + \alpha w^{IV} = p(x,t) \quad (0 < x < 1; t > 0) \quad (3.20)$$

$$w = w'' = 0 \quad (x = 0; x = 1; t \geq 0) \quad (3.21)$$

$$\dot{w} = \dot{w} = 0 \quad (0 < x < 1; t = 0) \quad (3.22)$$

However, the formulation of the problem is not yet complete. The dimension of the contact length  $c(t)$  is unknown so far and it must be specified in some way. A condition for  $c(t)$  was suggested by Korobkin [8] requiring no penetration of water particles into the structure, Eq. (3.23). This condition is a modification of the classical Wagner condition [2]. The function  $y_b$  describes the shape of the elastic beam in a moving deformed coordinate system. In this case,  $y_b = x - 1 \cdot t + w(x,t)$ . The unity factor multiplying the time corresponds to the scaled velocity. Thus, Eq. (3.23) becomes Eq. (3.24).

$$\int_0^{\pi/2} y_b [c(t) \sin \theta, t] d\theta = 0 \quad (3.23)$$

$$t = \frac{2}{\pi} c(t) + \frac{2}{\pi} \int_0^{\pi/2} w [c(t) \sin \theta, t] d\theta \quad (3.24)$$

The BVP (3.16)-(3.19), along with Eqs. (3.20)-(3.22) and condition (3.24) are coupled and have to be solved simultaneously. In the current analysis, the solution was found by using the normal mode method. Within this method, the beam deflection is approximated by Eq. (3.25). The functions  $\psi_n(x)$  are the eigen-functions, also known as dry modes of the beam, which are obtained by solving the homogeneous BVP (3.26)-(3.27). The coefficients  $a_n(t)$  are generalized coordinates or modal coordinates.

For a simple supported beam, the dry modes are given by Eq. (3.28) which satisfies the orthogonal Eq. (3.29) ( $\delta_{nm} = 0$  for  $n \neq m$  and  $\delta_{nn} = 1$  for  $n = m$ ).

$$w(x,t) = \sum_{n=1}^{\infty} \psi_n(x) a_n(t) \quad (3.25)$$

$$\psi_n^{IV}(x) = \lambda_n^4 \psi_n(x) \quad (0 < x < 1) \quad (3.26)$$

$$\psi_n(x) = \psi_n''(x) = 0 \quad (x = 0; x = 1) \quad (3.27)$$

$$\psi_n(x) = \sin(\lambda_n |x|) \quad \text{with} \quad \lambda_n = n\pi \quad (3.28)$$

$$\int_0^1 \psi_n(x) \psi_m(x) dx = \delta_{nm} / 2 \quad (3.29)$$

With approximation (3.25) for the beam deflection, Eq. (3.20) becomes Eq. (3.30). Multiplying the latter by any arbitrary eigenfunction  $\psi_m(x)$  and integrating over the beam length Eq. (3.31) is obtained. Note that the pressure term on the right hand side of Eq. (3.31) becomes zero for  $x > c(t)$ .

$$m \sum_{n=1}^{\infty} \psi_n(x) \ddot{a}_n(t) + \alpha \sum_{n=1}^{\infty} \psi_n^{IV}(x) a_n(t) = p(x,t) \quad (3.30)$$

$$m \sum_{n=1}^{\infty} \int_0^1 \psi_n(x) \psi_m(x) dx \ddot{a}_n(t) + \alpha \sum_{n=1}^{\infty} \int_0^1 \lambda_n^4 \psi_n(x) \psi_m(x) dx a_n(t) = \int_0^{c(t)} p(x,t) \psi_m(x) dx \quad (3.31)$$

The property of orthogonal modes (3.29) allows rewriting Eq. (3.31) in a more compact form of Eq. (3.32). The hydrodynamic pressure is given by Bernoulli Eq. (3.7) in terms of the velocity potential. Using the beam deflection approximation (3.25), the velocity potential function can be expanded as shown in Eq. (3.33), where the function  $\varphi_w(x,0,c)$  is the solution of the Wagner problem in its non-dimensional version. In this case  $\varphi_w(x,0,c) = -(c^2 - x^2)^{1/2}$  for  $|x| < c(t)$ . The functions  $\varphi_n(x,y,c)$  are the solutions of the harmonic BVP (3.34)-(3.37).

$$m \ddot{a}_m(t) + \alpha \lambda_m^4 a_m(t) = \int_{-c(t)}^{c(t)} p(x,t) \psi_m(x) dx \quad (3.32)$$

$$\varphi(x,0,t) = \varphi_w(x,0,c) + \sum_{n=1}^{\infty} \varphi_n(x,0,c) \dot{a}_n(t) \quad (3.33)$$

$$\varphi_{nxx} + \varphi_{nyy} = 0 \quad (y < 0) \quad (3.34)$$

$$\varphi_n = 0 \quad (y = 0, |x| > c(t)) \quad (3.35)$$

$$\varphi_{ny} = \psi_n(|x|) \quad (y = 0, |x| < c(t)) \quad (3.36)$$

$$\varphi_n \rightarrow 0 \quad (x^2 + y^2 \rightarrow \infty) \quad (3.37)$$

The substitution of the pressure term into the beam Eq. (3.32) leads to Eq. (3.38), where the functions  $f_m(c)$  and  $S_{nm}(c)$  are given by Eq. (3.39).

$$m \ddot{a}_m(t) + \alpha \lambda_m^4 a_m(t) = -\frac{d}{dt} f_m(c) - \frac{d}{dt} \sum_{n=1}^{\infty} S_{nm}(c) \dot{a}_n(t) \quad (3.38)$$

$$f_m(c) = \int_{-c}^c -\varphi_w(x, 0, c) \psi_m(|x|) dx, \quad S_{nm}(c) = \int_{-c}^c \varphi_n(x, 0, c) \psi_m(|x|) dx \quad (3.39)$$

The integrals  $S_{nm}(c)$  have been evaluated by Korobkin [8] for the case  $\psi_n(x) = \cos(\mu_n x)$ ,  $\mu_n = (n-1/2)\pi$ , which corresponds to the problem of wave impact on the center of an elastic Euler beam. The integrals  $S_{nm}(c)$  associated with the centered impact problem, which are denoted here by  $\hat{S}_{nm}(c)$ , are given by Eq. (3.40), where  $J_0(\mu_n)$  y  $J_1(\mu_n)$  are the zero and first order Bessel functions.

$$\begin{aligned} \hat{S}_{nm}(c) &= \frac{\pi c}{\mu_n^2 - \mu_m^2} [\mu_n J_0(\mu_m c) J_1(\mu_n c) - \mu_m J_0(\mu_n c) J_1(\mu_m c)] \quad (n \neq m) \\ \hat{S}_{nn}(c) &= \frac{\pi c^2}{2} [J_0^2(\mu_n c) + J_1^2(\mu_n c)] \end{aligned} \quad (3.40)$$

In order to evaluate the integrals  $S_{nm}(c)$  in the problem under consideration, expansion (3.41) was used. Eq. (3.41) expresses the actual mode shapes as a linear combination of those used to derive Eq. (3.40). After substitution, Eqs. (3.42) and (3.43) (matrix form) are found.

$$\psi_n(|x|) = \sum_{k=1}^{\infty} C_{nk} \cos(\mu_k x), \quad C_{nk} = \frac{2\lambda_n}{\lambda_n^2 - \mu_k^2} \quad (3.41)$$

$$S_{nm}(c) = \sum_{k=1}^{\infty} C_{nk} \sum_{s=1}^{\infty} C_{ms} \hat{S}_{ks}(c) \quad (3.42)$$

$$\mathbf{S} = \mathbf{C} \hat{\mathbf{S}} \mathbf{C}^T \quad (3.43)$$

Similarly, Eq. (3.38) can also be rewritten as Eq. (3.44) or in its matrix form, Eq. (3.45), where  $\mathbf{M}$  is the mass matrix and  $\mathbf{K}$  is the diagonal matrix with elements  $\alpha\lambda_m^4$ .  $\mathbf{S}$  is the matrix of added masses; it is symmetric and depends only on the dimension of the contact region  $c$ . The vector  $\mathbf{f}$  is associated with the Wagner hydrodynamic pressure and also depends on  $c$ .

$$\frac{d}{dt} \left[ \left( m \dot{a}_m(t) + \sum_{n=1}^{\infty} S_{nm}(c) \dot{a}_n(t) \right) - f_m(c) \right] + \alpha \lambda_m^4 a_m(t) = 0 \quad (3.44)$$

$$\frac{d}{dt} [(\mathbf{M} + \mathbf{S})\dot{\mathbf{a}} - \mathbf{f}] + \mathbf{K}\mathbf{a} = \mathbf{0} \quad (3.45)$$

Eq. (3.45) is a system of infinite ordinary differential equations (ODEs) of second order with respect to the modal coordinates  $a(t)$ .  $\mathbf{S}$  and  $\mathbf{f}$  depend on the unknown variable  $c$  but not explicitly with time  $t$ . Therefore, it is convenient to take  $c$  as the new independent variable ( $0 \leq c \leq 1$ ) instead of time  $t$ . This substitution is valid if  $dc/dt > 0$  which is the main assumption within the Wagner approach. A differential equation (3.46) for the unknown function  $t(c)$  follows from Eq. (3.24) after its differentiation with respect to  $c$ . Taking into account expansion (3.25), Eq. (3.47) is obtained. The coordinates  $a_n(t)$  are functions only of  $t$  and are considered constants in the integration along the variable  $\theta$ . Thus, Eq. (3.47) can be rewritten as Eq. (3.48). Eq. (3.49) follows after performing the derivative of the term in brackets. Finally the differential equation for the function  $t(c)$  takes the form of Eq. (3.50), where the function  $Q$  is given by Eq. (3.51).

$$\frac{dt}{dc} = \frac{2}{\pi} + \frac{2}{\pi} \frac{d}{dc} \left[ \int_0^{\pi/2} w[c(t) \sin \theta, t] d\theta \right] \quad (3.46)$$

$$\frac{dt}{dc} = \frac{2}{\pi} + \frac{2}{\pi} \frac{d}{dc} \left[ \int_0^{\pi/2} \sum_{n=1}^{\infty} \psi_n(c \sin \theta) a_n(t) d\theta \right] \quad (3.47)$$

$$\frac{dt}{dc} = \frac{2}{\pi} + \frac{2}{\pi} \frac{d}{dc} \left[ \sum_{n=1}^{\infty} \left( \int_0^{\pi/2} \psi_n(c \sin \theta) d\theta \right) a_n(t) \right] \quad (3.48)$$

$$\frac{dt}{dc} = \frac{2}{\pi} + \frac{2}{\pi} \sum_{n=1}^{\infty} \left[ \left( \int_0^{\pi/2} \psi_n^I(c \sin \theta) \sin \theta d\theta \right) a_n(t) + \left( \int_0^{\pi/2} \psi_n(c \sin \theta) d\theta \right) \dot{a}_n(t) \frac{dt}{dc} \right] \quad (3.49)$$

$$\frac{dt}{dc} = Q(c, \mathbf{a}, \dot{\mathbf{a}}) \quad (3.50)$$

$$Q = \frac{1 + \sum_{n=1}^{\infty} \left( \int_0^{\pi/2} \psi_n'(c \sin \theta) \sin \theta d\theta \right) a_n(t)}{\pi/2 - \sum_{n=1}^{\infty} \left( \int_0^{\pi/2} \psi_n(c \sin \theta) d\theta \right) \dot{a}_n(t)} \quad (3.51)$$

By introducing new variables  $\mathbf{Z}_1 = \mathbf{a}$ ,  $\mathbf{Z}_2 = (\mathbf{M} + \mathbf{S})\dot{\mathbf{a}} - \mathbf{f}$  and  $\mathbf{Z}_3 = t$ , it is possible to transform the system of ODEs of second order (3.45) and (3.50) into a new system of ODEs of first order. Although this technique increases twice the size of the system, it allows us to use numerical methods suitable for solving systems of ODEs of first order. Thus the original system becomes system (3.52)-(3.54).

$$\overset{\square}{\mathbf{Z}_1} = \mathbf{R}Q(c, \mathbf{a}, \mathbf{R}) \quad (3.52)$$

$$\overset{\square}{\mathbf{Z}_2} = -\mathbf{K}\mathbf{Z}_1 Q(c, \mathbf{a}, \mathbf{R}) \quad (3.53)$$

$$\overset{\square}{\mathbf{Z}_3} = Q(c, \mathbf{a}, \mathbf{R}) \quad (3.54)$$

Here dot indicates derivative with respect to  $c$  and  $\mathbf{R} = (\mathbf{M} + \mathbf{S})^{-1}(\mathbf{Z}_2 + \mathbf{f})$ . The initial conditions for system (3.52)-(3.54) are  $\mathbf{Z}_1 = \mathbf{Z}_2 = \mathbf{Z}_3 = 0$  for  $c = 0$ . The initial value problem (IVP) (3.52)-(3.54) was solved using the fourth-order Runge-Kutta algorithm and the results are presented in Chapter 5.

### 3.3 WATER IMPACT OF SANDWICH COMPOSITE HULLS

The current study of water impact of sandwich composite hulls was conducted entirely using FE analysis. This means that no analytical model was used to validate the FE results. Only the mathematical formulation presented by Qin and Batra in [10] for hydroelastic impact of sandwich panels was used as an initial approach to study the problem. However, FE results corresponding to rigid and metallic hulls were in fact validated using the analytical models presented in Sections 3.1 and 3.2, and FE models of sandwich composite hulls were developed directly from those existing models. Consequently, FE results of sandwich composite hulls were assumed to be correct.

## CHAPTER 4. FINITE ELEMENT MODELING

In this chapter the governing equations of the fluid-structure impact problem are presented along with a brief description of the Lagrangian, Eulerian and ALE formulations implemented in LS-DYNA. The fluid flow is solved using an Eulerian formulation on a Cartesian grid that overlaps the structural mesh. The structure is described using the classical Lagrangian approach in which the FE mesh moves with the material. ALE formulation is a general description of representing the governing equations of the problem which contains both Eulerian and Lagrangian formulations as particular cases.

### 4.1 LAGRANGIAN DESCRIPTION

Consider the body shown in Figure 4.1 [16] which occupies the domain  $\Omega_X$  in the current configuration and let  $\partial\Omega_X$  denotes its boundary. In the Lagrangian or material representation, the current coordinates  $x$  are expressed in terms of the reference coordinates  $X$  (usually the undeformed configuration) and the variation of a typical variable  $\phi$  over the domain is described with respect to the material coordinates  $X$  and time  $t$ , Eqs. (4.1) and (4.2). The time derivative of  $\phi$  is simply the partial derivative with respect to time, because the material coordinates  $X$  do not change with time, Eq. (4.3).

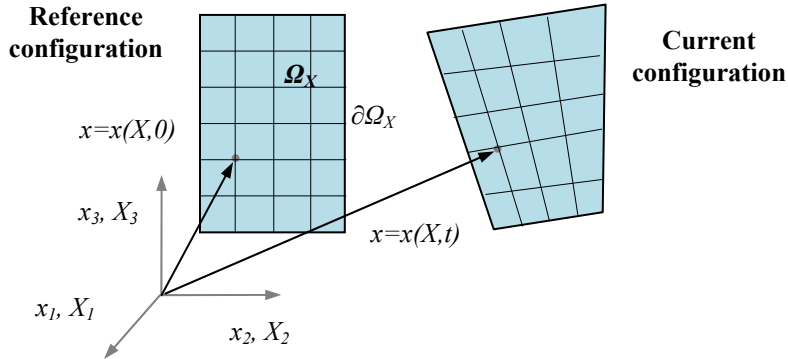


**Figure 4.1.** Lagrangian or material description.

$$x = x(X, t) \quad (4.1)$$

$$\phi = \phi(X, t) \quad (4.2)$$

$$\frac{d}{dt} \phi(X, t) = \frac{\partial}{\partial t} \phi(X, t) \quad (4.3)$$

The Lagrangian formulation for the momentum and energy of the body are given by Eqs. (4.4) and (4.5) in which  $\sigma$  and  $\epsilon$  are the stress and strain tensors respectively,  $\rho$  is the mass density,  $v$  is the material velocity,  $f$  is the force density and  $e$  is the internal energy. Dots indicates time derivative and “:” denotes the double dot product.

$$\rho \frac{\partial v}{\partial t} = \text{div}(\sigma) + f \quad (4.4)$$

$$\rho \frac{\partial e}{\partial t} = \sigma : \epsilon^{\square} \quad (4.5)$$

Solution of Eqs. (4.4) and (4.5) requires the satisfaction of displacement boundary condition (4.6) on  $\partial\Omega_X^D$  and the traction boundary condition (4.7) on  $\partial\Omega_X^T$ . The vector  $n$  is the unit normal vector oriented outward at the boundary  $\partial\Omega_X$ . At time  $t = 0$  the initial conditions are given by Eqs. (4.8) and (4.9).

$$x(X, t) = D(t) \quad \text{on } \partial\Omega_X^D \quad (4.6)$$

$$\sigma(X, t) \cdot n = T_X(t) \quad \text{on } \partial\Omega_X^T \quad (4.7)$$

$$x(X, 0) = X_0(X) \quad (4.8)$$

$$v(X, 0) = V_0 \quad (4.9)$$

The material formulation is completed with the constitutive model and the kinematics equations. For a linear elastic material, the constitutive relationship takes the form of Eq. (4.10). The constants  $K$  and  $G$  represent the bulk and the shear modulus respectively and they are defined in terms of the Young modulus of elasticity  $E$  and the Poisson ratio  $\nu$ , Eq. (4.13).  $\Delta V/V$  is the specific volumetric deformation of the solid computed as the sum of the diagonal elements of the strain tensor,  $\mathbf{I}$  is the identity matrix and  $\epsilon_d$  is the deviatoric component of the strain tensor. In the Lagrangian approach the mass conservation is trivially satisfied through the formulation of Eq. (4.14) where  $\rho_0$  is the mass density in the reference configuration and  $J$  is the determinant of the deformation gradient matrix  $\text{grad}(x) = \partial x / \partial X$ .

$$\sigma = -K \frac{\Delta V}{V} \mathbf{I} + 2G\epsilon_d \quad (4.10)$$

$$\epsilon = \frac{1}{2} [\text{grad}(x) + \text{grad}(x)^T] \quad (4.11)$$

$$\boldsymbol{\varepsilon} = \frac{1}{2} [\text{grad}(v) + \text{grad}(v)^T] \quad (4.12)$$

$$K = \frac{E}{3(1-2\nu)}, \quad G = \frac{E}{2(1+\nu)} \quad (4.13)$$

$$\rho J = \rho_0 \quad (4.14)$$

Eqs. (4.4)-(4.14) are solved using a FE mesh that moves with the material tracking the solid surfaces at each time interval. This formulation is very useful in solid mechanics where deformations are relatively small. In fluid mechanics mesh distortion associated with large deformations might result in inaccuracies and numerical instability, therefore, requiring the Eulerian description for the fluid domain.

## 4.2 EULERIAN DESCRIPTION

In the Eulerian or spatial description [16] (Figure 4.2), the motion of the body is referred to the current configuration and the variable  $\phi$  is described in terms of the current coordinates  $x$  and time  $t$ , Eq. (4.15). In those terms, the time derivative of  $\phi$ , also known as the material derivative, is given by Eq. (4.16) or equivalently by Eq. (4.17).

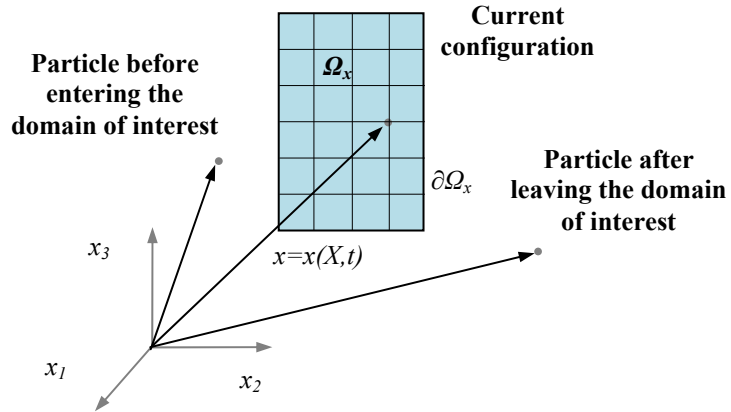


**Figure 4.2.** Eulerian or spatial description.

$$\phi = \phi(x, t) \quad (4.15)$$

$$\frac{d}{dt} \phi(X, t) = \frac{\partial}{\partial t} \phi(x, t) + \frac{\partial}{\partial x} \phi(x, t) \frac{dx}{dt} \quad (4.16)$$

$$\frac{d\phi}{dt} = \frac{\partial \phi}{\partial t} + \mathbf{v} \cdot \mathbf{grad}(\phi) \quad (4.17)$$

Assuming that  $\Omega_x$  is the domain occupied by the body particles in the current configuration with boundary  $\partial\Omega_x$ , the spatial formulation of conservation of mass, momentum and energy are presented in Eqs. (4.18), (4.19) and (4.20). Additional terms associated with the material velocity  $\mathbf{v}$  are known as convective terms. For a Newtonian viscous fluid, the stress tensor  $\boldsymbol{\sigma}$  in the reference domain can be represented according to Eq. (4.21) in which  $p$  is the pressure,  $q$  is the bulk viscosity,  $\mu$  is the dynamic viscosity and  $\boldsymbol{\epsilon}$  is the strain rate tensor.

$$\frac{\partial \rho}{\partial t} + \rho \cdot \mathbf{div}(\mathbf{v}) + \mathbf{v} \cdot \mathbf{grad}(\rho) = 0 \quad (4.18)$$

$$\rho \frac{\partial \mathbf{v}}{\partial t} + \rho \mathbf{v} \cdot \mathbf{div}(\mathbf{v}) = \mathbf{div}(\boldsymbol{\sigma}) + \mathbf{f} \quad (4.19)$$

$$\rho \frac{\partial e}{\partial t} + \rho \mathbf{v} \cdot \mathbf{grad}(e) = \boldsymbol{\sigma} : \boldsymbol{\epsilon} \quad (4.20)$$

$$\boldsymbol{\sigma} = -(p + q)\mathbf{I} + 2\mu\boldsymbol{\epsilon} \quad (4.21)$$

The pressure  $p$  is computed using an equation of state (EOS) which is defined as the relationship between the change in pressure and the change in mass density and energy,  $p = \text{EOS}(e, \rho)$ . Solution of Eqs. (4.18)-(4.21) must satisfy the velocity boundary condition (4.22) on  $\partial\Omega_x^V$  and the traction boundary condition (4.23) on the remaining part of the boundary,  $\partial\Omega_x^T$ . The solution must also satisfy the initial conditions (4.24). In fluid mechanics, the Eulerian coordinate system in a fixed mesh in space is the traditional approach. The fixed mesh eliminates the limitation on the degree of deformation allowed in the material, but introduces the additional complexity of the convective terms associated with the transport of material through the mesh elements.

$$\mathbf{v}(X, t) = \mathbf{V}(t) \quad \text{on } \partial\Omega_x^V \quad (4.22)$$

$$\boldsymbol{\sigma}(X, t) \cdot \mathbf{n} = \mathbf{T}_F(t) \quad \text{on } \partial\Omega_x^T \quad (4.23)$$

$$\mathbf{v}(\mathbf{x}, 0) = \mathbf{V}_0(\mathbf{x}) \quad (4.24)$$

### 4.3 GENERAL ALE FORMULATION

In the ALE description of motion [15, 16], an *arbitrary* reference domain  $\Omega_y$  is introduced in addition to the previous discussed material ( $\Omega_x$ ) and spatial ( $\Omega_s$ ) domains. In fact, this new reference frame corresponds to the finite element mesh in which the problem will be formulated [15]. The arbitrary movement of the reference frame along with an adequate mesh moving and advection algorithms [15, 18] allow the ALE description to deal with moving boundaries, free surface and interface contact problems. The material derivative of the variable  $\phi$  is computed using Eq. (4.25) where  $y$  is the reference coordinate,  $v$  is the material velocity and  $w$  is the velocity of the reference frame (FE mesh). Note that the ALE representation contains both Lagrangian and Eulerian formulations as particular cases. If the mesh velocity  $w = v$ , Eq. (4.25) becomes into Eq. (4.3) while if  $w = 0$ , Eq. (4.17) is obtained.

$$\frac{\partial \phi(X,t)}{\partial t} = \frac{\partial \phi(y,t)}{\partial t} + (v - w) \cdot \text{grad}(\phi(y,t)) \quad (4.25)$$

The formulation of conservation of mass, momentum and energy in the ALE description is given by Eqs. (4.26), (4.27) and (4.28). Variables, boundary and initial conditions are defined similarly as done in Sections 4.1 and 4.2. In most fluid-structure interaction problems, neither the Lagrangian nor the Eulerian formulations are optimal for the entire domain. Instead, ALE methods combine a Lagrangian formulation for the structure with an Eulerian formulation for the fluid. The interaction forces between the moving mesh and the mesh fixed in space is managed by a coupling algorithm [14, 16]. The terms related to the relative velocity  $v - w$  are usually referred to as the convective terms. The nonlinearities associated with those terms present one of the major difficulties in the time integration of ALE equations.

$$\frac{\partial \rho}{\partial t} + \rho \cdot \text{div}(v) + (v - w) \cdot \text{grad}(\rho) = 0 \quad (4.26)$$

$$\rho \frac{\partial v}{\partial t} + \rho(v - w) \cdot \text{div}(v) = \text{div}(\boldsymbol{\sigma}) + f \quad (4.27)$$

$$\rho \frac{\partial e}{\partial t} + \rho(v - w) \cdot \text{grad}(e) = \boldsymbol{\sigma} : \boldsymbol{\epsilon}^{\square} \quad (4.28)$$

The common approach followed by the computational fluid dynamic (CFD) community is to solve the fully coupled equations [15]. However, many commercial codes, including LS-DYNA, implement an alternative approach named the operator splitting method [14]. Operator splitting is a convenient technique of breaking complicated problems into a series of less complex problems. In this method, the calculations performed for each time step are divided into two phases, a Lagrangian phase followed by an advection or Eulerian phase. In the Lagrangian step, in which the mesh moves with the material, changes in velocity, pressure and internal energy due to external and internal forces are computed using an explicit time integration scheme. In the Eulerian step, the deformed mesh is remapped back to its original position and the transport of mass, momentum and energy across element boundaries are computed (Figure 4.3). A detailed discussion of these topics is presented in the following sections.

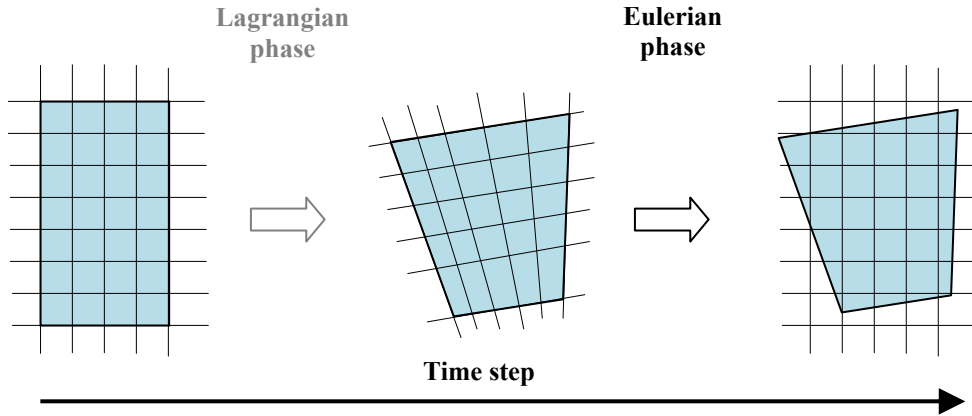


**Figure 4.3.** Split operator.

### 4.3.1 The Operator Splitting

The progression of the solution in time in ALE methods is performed by breaking the governing partial differential equations (PDEs) into a series of simpler PDEs which are solved sequentially. The basic concept of the operator splitting can be illustrated using a simple linear ordinary differential equation (ODE) [16]. Consider the IVP described in Eqs. (4.29) and (4.30).

$$\frac{d\phi}{dt} - (L_1 + L_2)\phi = 0 \quad (4.29)$$

$$\phi(t = 0) = \phi_0 \quad (4.30)$$

$$\phi(\Delta t) = e^{(L_1 + L_2)\Delta t} \phi_0 \quad (4.31)$$

In the general case,  $\phi$  can be a scalar or a vector function of  $t$  and  $L_1$  and  $L_2$  can be scalars or matrices. The solution of this problem within the interval  $\Delta t$  is given in Eq. (4.31) where  $e^{(L_1+L_2)}$  is the matrix exponential of matrix  $(L_1+L_2)$ . Suppose that instead of solving Eqs. (4.29) and (4.30) in a single time step  $\Delta t$ , the problem is divided into two simpler IVPs as shown in Eqs. (4.32) and (4.33). It is easily to demonstrate that solutions for  $\phi^1$  and  $\phi^2$  are of the form of Eqs. (4.34) and (4.35).

$$\frac{d\phi^1}{dt} - L_1 \phi^1 = 0, \quad \phi^1(0) = \phi_0 \quad (4.32)$$

$$\frac{d\phi^2}{dt} - L_2 \phi^2 = 0, \quad \phi^2(0) = \phi^1(\Delta t), \quad \phi^2(\Delta t) = \phi(\Delta t) \quad (4.33)$$

$$\phi^1(\Delta t) = e^{L_1 \Delta t} \phi_0 \quad (4.34)$$

$$\phi^2(\Delta t) = \phi(\Delta t) = e^{L_2 \Delta t} \phi^1(\Delta t) = e^{L_2 \Delta t} e^{L_1 \Delta t} \phi_0 \quad (4.35)$$

If  $L_1$  and  $L_2$  are scalars or commutative matrices ( $L_1 L_2 = L_2 L_1$ ), Eqs. (4.31) and (4.35) are identical. However, for arbitrary matrices  $L_1$  and  $L_2$ , that is not true and an error is introduced in the solution of the problem as a result of the splitting process. According to the literature [16], the order of the this error is proportional to  $(\Delta t)^3$  which is an acceptable accuracy cost considering the computational benefits. To illustrate how the operator splitting is applied to ALE formulation, consider the model Eq. (4.36). The function  $\phi$  is a generalization of the material variables ( $\rho$ ,  $\rho v$  and  $\rho e$ ) and the term  $S(x,t)$  represents the source term. Using the operator splitting, Eq. (4.36) can be rewritten as two equivalent equations, Eqs. (4.37) and (4.38). The first one has the form of the Lagrangian equation in which the relative velocity  $v - w = 0$ . This phase is called the Lagrangian step and its solution is obtained using a mesh that moves with the material velocity  $v$ .

$$\frac{\partial \phi}{\partial t} + (v - w) \cdot \text{grad}(\phi) = S(x, t) \quad (4.36)$$

$$\frac{\partial \phi}{\partial t} = S(x, t) \quad (4.37)$$

$$\frac{\partial \phi}{\partial \tau} + v \cdot \text{grad}(\phi) = 0, \quad \phi(x, 0) = \phi_0(x) \quad (4.38)$$

The second equation which contains only the convective terms is commonly referred to as the Eulerian or advection step. In this phase, the deformed mesh obtained at the end of the Lagrangian phase is remapped back to its original position using a mesh smoothing algorithm [15]. Later, the transport of mass, momentum and energy across element boundaries are computed sequentially using as initial configuration  $\phi_0(x)$  which is the solution of the Lagrangian phase at the current time step. The variable  $\tau$  in Eq. (4.38) is a fictitious time because the time step is not updated during the advection phase. The splitting process of the time step is shown in Figure 4.4.

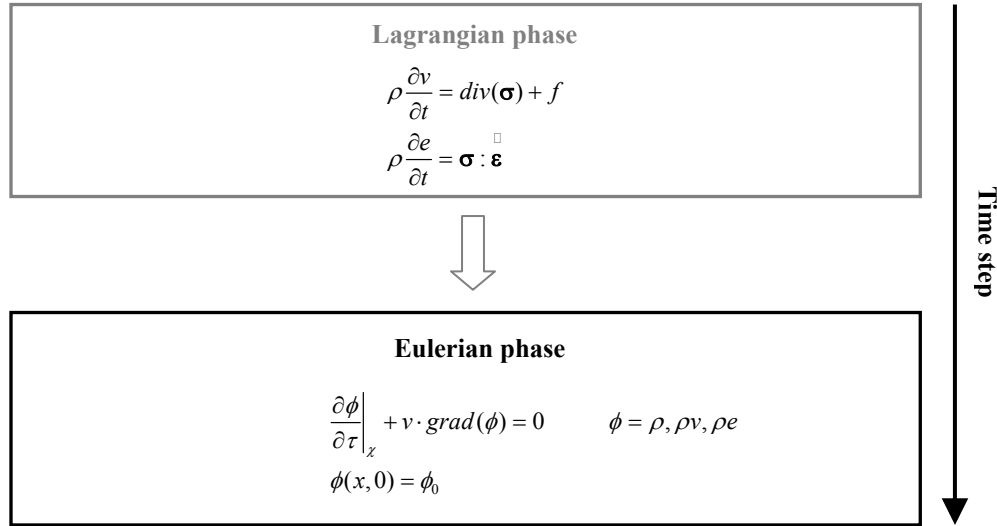


**Figure 4.4.** Split time step into two phases.

### 4.3.2 The Lagrangian Step

The principle of virtual displacements states that the virtual work of all actual forces when moving through a virtual displacement is zero if the body is in equilibrium, Eq. (4.39). The virtual displacement  $\delta x$  is arbitrary but must satisfies the constraint  $\delta x = 0$  in  $\partial\Omega_X^D$ . Using the divergence theorem Eq. (4.39) can be rewritten as Eq. (4.40) which is known as the weak form of the equilibrium equations.

$$\int_{\Omega_X} \rho \frac{\partial v}{\partial t} \delta x \, dX = \int_{\Omega_X} \operatorname{div}(\sigma) \delta x \, dX + \int_{\Omega_X} f \delta x \, dX \quad (4.39)$$

$$\int_{\Omega_X} \rho \frac{\partial v}{\partial t} \delta x \, dX = - \int_{\Omega_X} \boldsymbol{\sigma} : \boldsymbol{\delta \epsilon} \, dX + \int_{\Omega_X} f \delta x \, dX + \int_{\partial \Omega_X^T} T_X \delta x \, dS \quad (4.40)$$

Eq. (40) is solved in a Lagrangian FE mesh in which the coordinates, velocity, and virtual displacement are interpolated from their values at the nodes using the shape functions  $\chi(\xi, \eta, \zeta)$ . In Eq. (4.41),  $\xi$ ,  $\eta$  and  $\zeta$  are parametric coordinates,  $N$  is the number of nodes in defining the element and  $x_s$  are the nodal coordinates. Extending the weak form of the equilibrium equations to the  $m$  elements that form the FE mesh and considering approximation (4.41), Eq. (4.42) is derived. The term on the right hand side of Eq. (4.42) is the mass matrix, the first term on the left hand side represents the internal forces on the body and the second and third terms represent the external forces. The mass matrix  $\mathbf{M}^c$  in Eq. (4.43) is called the consistent mass matrix because its derivation is consistent with the FE method.

$$x(X, t) = \sum_{s=1}^N \chi_s(\xi, \eta, \zeta) \cdot x_s(t) \quad (4.41)$$

$$\sum_{r=1}^m \int_{\Omega_{Xr}} \rho \chi_s \chi_k a_k \, dX_r \delta x_s = - \sum_{r=1}^m \int_{\Omega_{Xr}} \chi_{s,i} \sigma_i \, dX_r \delta x_s + \sum_{r=1}^m \int_{\Omega_{Xr}} f \chi_s \, dX_r \delta x_s + \sum_{r=1}^m \int_{\partial \Omega_{Xr}^T} T_X \chi_s \, dS_r \delta x_s \quad (4.42)$$

$$M_{sk}^c = \int_{\Omega_{Xr}} \rho \chi_s \chi_k \, dX_r \quad (4.43)$$

$$F_s^{\text{int}} = \int_{\Omega_{Xr}} \chi_{s,i} \sigma_i \, dX_r \quad (4.44)$$

$$F_s^{\text{ext}} = \int_{\Omega_{Xr}} f \chi_s \, dX_r + \int_{\partial \Omega_{Xr}^T} T_X \chi_s \, dS_r \quad (4.45)$$

Using the mass matrix  $\mathbf{M}^c$  would require solving a linear system of equations for the acceleration  $\partial v / \partial t$  at each time instant, which may be computationally costly. Instead the lumped diagonal mass matrix  $\mathbf{M}$  is commonly used; Eq. (4.46). The system of equations of motion is now decoupled and for each node  $s$  the acceleration at time  $t^n$  is easily computed using Eq. (4.48).

$$M_{ss} = \int_{\Omega_{Xr}} \rho \chi_s \chi_s \, dX_r \quad (4.46)$$

$$M_{ss} a_s = -F_s^{\text{int}} + F_s^{\text{ext}} = F_s \quad (4.47)$$

$$a_s^n = \frac{F_s^n}{M_{ss}} \quad (4.48)$$

$$v_s^{n+1/2} = v_s^{n-1/2} + \Delta t \cdot a_s^n \quad (4.49)$$

$$d_s^{n+1} = d_s^n + \Delta t \cdot v_s^{n+1/2} \quad (4.50)$$

$$\Delta t \leq \frac{\ell}{c} \quad (4.51)$$

The nodal velocities and displacements are obtained using central difference time integration of the nodal accelerations and velocities respectively, Eqs. (4.49) and (4.50). In the central difference method the time step is limited by stability considerations like all explicit integration methods. The stable time step size is limited according to Eq. (4.51) in which  $\ell$  is the characteristic length of the smallest element and  $c$  is the speed of sound in the material. For a linear elastic material the speed of sound is  $c = (E/\rho)^{1/2}$ . Notice that the form of this stability limit is similar to that in transport algorithms where  $c$  is the velocity of the fluid. The physical interpretation is that the time step must be smaller than the time required for a wave to propagate through the element. For larger time steps, waves would jump elements which never would experience their effect.

### 4.3.3 The Eulerian Step

In the Eulerian step, the deformed mesh obtained from the Lagrangian calculations is remapped back to its original position and the transport of variables across element boundaries is computed. The overall flow of an advection step includes: 1) to decide which nodes to move; move the boundary nodes and then move the interior nodes and 2) to calculate the transport of the element-centered variables and compute the transport of momentum and update the velocity. The movement of the nodes relative to the material is performed using a mesh relaxation or mesh smoothing algorithm [15]. Different relaxation algorithms have been implemented in FE codes; the Equipotential method [15] which was found to be stable for a broad range of problems, the simple average algorithm, the Kikuchi's algorithm and combinations of those. The selection and implementation of the mesh relaxation algorithm is the most difficult and challenging step in ALE methods and is problem dependent. The code implemented in this thesis uses the Equipotential smoothing algorithm and the donor cell advection method [18, 19]. Both algorithms are simple, stable and accurate and have been extensively used to solve impact problems. The mathematical bases of smoothing algorithms and advection methods are not discussed here because they are beyond the scope of this work.

#### 4.3.4 Fluid-Structure Interaction

The interaction between the Lagrangian mesh and the Eulerian mesh is managed by the penalty based contact algorithm available in LS-DYNA [18, 19]. In the contact interface, the fluid nodes are allowed to penetrate a small amount  $e$  into the structural mesh. The penalty contact formulation works as a spring damper system imposing resisting forces  $F_f$  and  $F_s$  at the contact nodes [14], (Figure 4.5). The resisting forces are proportional to the penetration depth  $e$ , penetration velocity  $\dot{e}$  and user defined stiffness  $k_D$  and damping  $\xi$ . The stiffness factor  $k_D$  is calculated by LS-DYNA in terms of the bulk modulus ( $\rho \cdot c^2$ ) and the average size of the elements in contact  $dx$  using Eq. (4.52), where  $pf$  is a user defined scale factor set by default to 0.1. To avoid numerical instability  $pf$  must satisfy  $0 \leq pf \leq 1$ . According to Stenius [17], the appropriate selection of the contact properties is highly dependent on the mesh density. Too low contact stiffness leads to numerical leakage while an excessively high stiffness results in an oscillating solution.

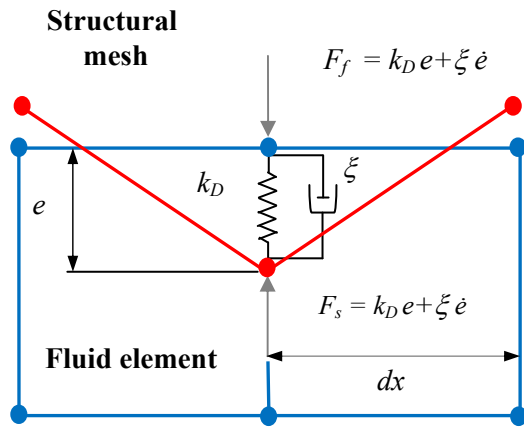


**Figure 4.5.** Penalty coupling schematic diagram.

$$K_D = \frac{p_f \cdot \rho \cdot c^2}{dx} \quad (4.52)$$

#### 4.4 LS-DYNA MODELS

FE models were developed using the commercial explicit code LS-DYNA. Explicit FE analysis is well suited for dynamic simulations of impact problems, but it may become prohibitively expensive for long time duration analyses. Therefore, this work focused on a balanced solution between accuracy and computational cost. The initial approach to model the problem is shown in Figure 4.6 which included the entire hull structure. Later, the model was simplified to take into account the symmetry of the problem and thus to reduce the FE mesh size. The hull structure was also simplified to a simple beam (Figure 4.7). The model extension in  $z$ -direction was one single element. The fluid domains, water and air, were modeled using an Eulerian mesh with solid one-point (Gauss quadrature integration) ALE multimaterial element formulation (ELFORM = 11). The pressure-volume-internal energy relationship in the fluid elements was defined using the Gruneisen EOS [18, 19], even though the theoretical models described in Chapter 3 assumed the fluid as incompressible. EOS's are required in problems involving high pressures and shock wave propagation in order to accurately simulate the material behavior. Therefore, some compressibility in the water was expected to occur during the simulations. The air domain was modeled as void which allows water material to flow through the air mesh. The beam was modeled using Lagrangian shell elements, for steel beams, and a combination of shell and solid elements, for sandwich composite beams. The analysis was restricted to two dimensions by constraining all nodes in the  $z$ -direction. Non reflecting boundary conditions were defined in the fluid borders to simulate a semi-infinite domain. The interaction between the fluid and the structure was managed by the penalty based contact algorithm described in Section 4.3.4. Numerical sensor shell elements were defined in the fluid-structure contact region in order to record the pressure data during the simulations.

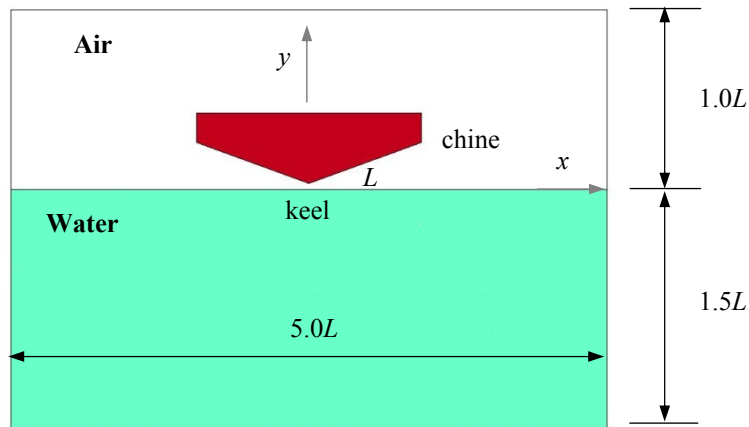


**Figure 4.6.** Finite element model.

The pre-knowledge of the expanding pressure peak obtained from theoretical models was used to design the FE mesh in order to reduce the computational time of the simulations. As a result, the fluid domain was divided into two domains: 1) an interior domain located close to the keel, where high spatial resolution was required, and 2) an exterior domain located beyond the influence of the impact. Note that these domains do not correspond to the inner and outer regions defined in Section 3.2. The interior domain was uniformly meshed while within the exterior domain an expanding mesh toward the model boundaries was used. The size of the fluid elements in the uniform meshed region was estimated based on results of a parameter study conducted on water-impact problems [17]. The objective of this study was to provide general guidance for the appropriate selection of element size and contact stiffness to capture the pressure peak with satisfactory accuracy. According to Stenius [17], the mesh density and contact stiffness are highly dependent and at least, eight elements must be used within the pressure peak to capture it with sufficient accuracy. Further elements will result in a considerable computational effort in addition to the full capture of the pressure peak is not necessary in the modeling of fluid-structure interaction. To avoid contact problems, the structural elements and the fluid elements (within the inner region) were similar in size. The contact stiffness scale factor  $p_f$  and the contact damping  $\xi$  were set as default, 0.1 and 0 respectively. These settings conducted to good correlation for the pressure peak between theoretical and numerical results as shown in the next chapter. During this investigation, it was concluded that neither  $p_f$  nor  $\xi$  had a significant effect on the solution. This was found by comparing results of different simulations with different values of  $p_f$  and  $\xi$ . Instead, it was the mesh density within the pressure peak the critical factor to be considered.

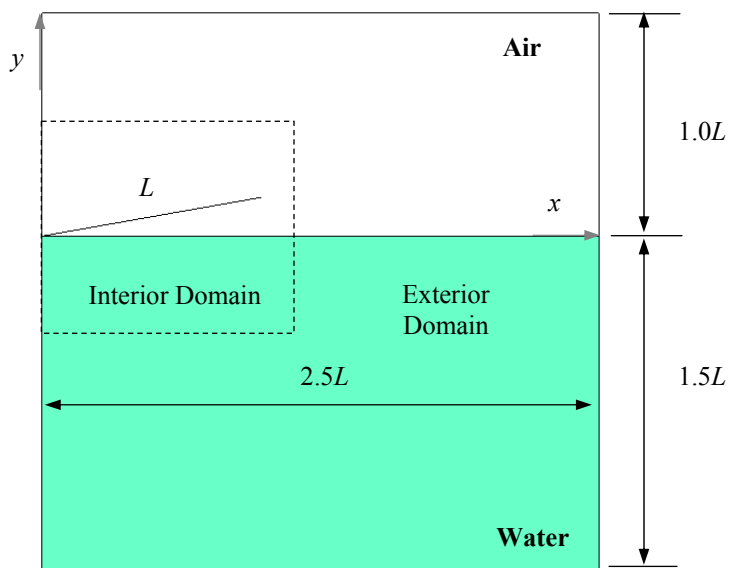


**Figure 4.7.** Simplified FE model.

## CHAPTER 5. FE RESULTS AND DISCUSSION

This chapter presents the results of FE simulations of symmetrical hull-water impacts. Three different structural models were considered for the hull structure: rigid, linear elastic (metallic) and sandwich composite. The fluid formulation and coupling method described in Chapter 4 were used. The time required to complete the impact stage depends on the characteristics of the problem under study (hull dimensions, deadrise angle, impact velocity and structural deformation). Therefore, the simulation time was estimated using analytical models [2, 8 and 9]. Hydrodynamic pressures of rigid hull impacts were verified with analytical solutions and compared with experimental data [23]. Results demonstrated to have better correlation than those published in the literature [14, 17]. The structural response of metallic hulls was validated using the hydroelastic model presented in Chapter 3. Results of sandwich composite models are discussed in Section 5.3.

### 5.1 WATER IMPACT OF RIGID HULLS

First, the impact of a rigid hull with deadrise angle  $\beta$  and vertical velocity  $V$  into water was considered. In this case, the hydrodynamic loads and the structural response can be treated separately, which simplifies the problem considerably. Impacts of rigid hulls were studied in the current work in order to get the first approach into the water impact problem. Abundant literature is available on slamming of rigid bodies which was used to validate the computational results. The hull structure was modeled in LS-DYNA using the RIGID material type. Rigid elements are computationally very cost effective since no memory is allocated for storing history variables [18, 19], only the fluid variables are computed during the impact simulation. A typical case study in the literature is the rigid hull with deadrise angle  $\beta = 20^\circ$  and vertical velocity  $V = 5$  m/s. Consequently, this case was selected for analysis in this work. The bottom hull length was  $L = 0.2$  m for all study cases. The fluid element size within the interior domain was chosen based on the pre-knowledge of the expanding pressure peak ( $dx = 0.5 \times 10^{-3}$  m). The contact stiffness, based on Eq. (4.52), was  $k_D = 4.5$  GPa/m and no contact damping was considered ( $\xi = 0$ ). The fluid density was assumed constant,  $\rho_W = 1000$  kg/m<sup>3</sup>. Based on Wagner's model, the simulation time for the penetration stage was estimated in 9.0 milliseconds (ms) approximately. In order to guarantee stability of the solution (a non-oscillatory-converged solution), the default time step calculated by LS-DYNA was scaled by a factor 0.3 [18, 19]. The computational cost of the simulation was in the order of 4 hours using a 2.66 GHz Core 2 Quad processor PC.

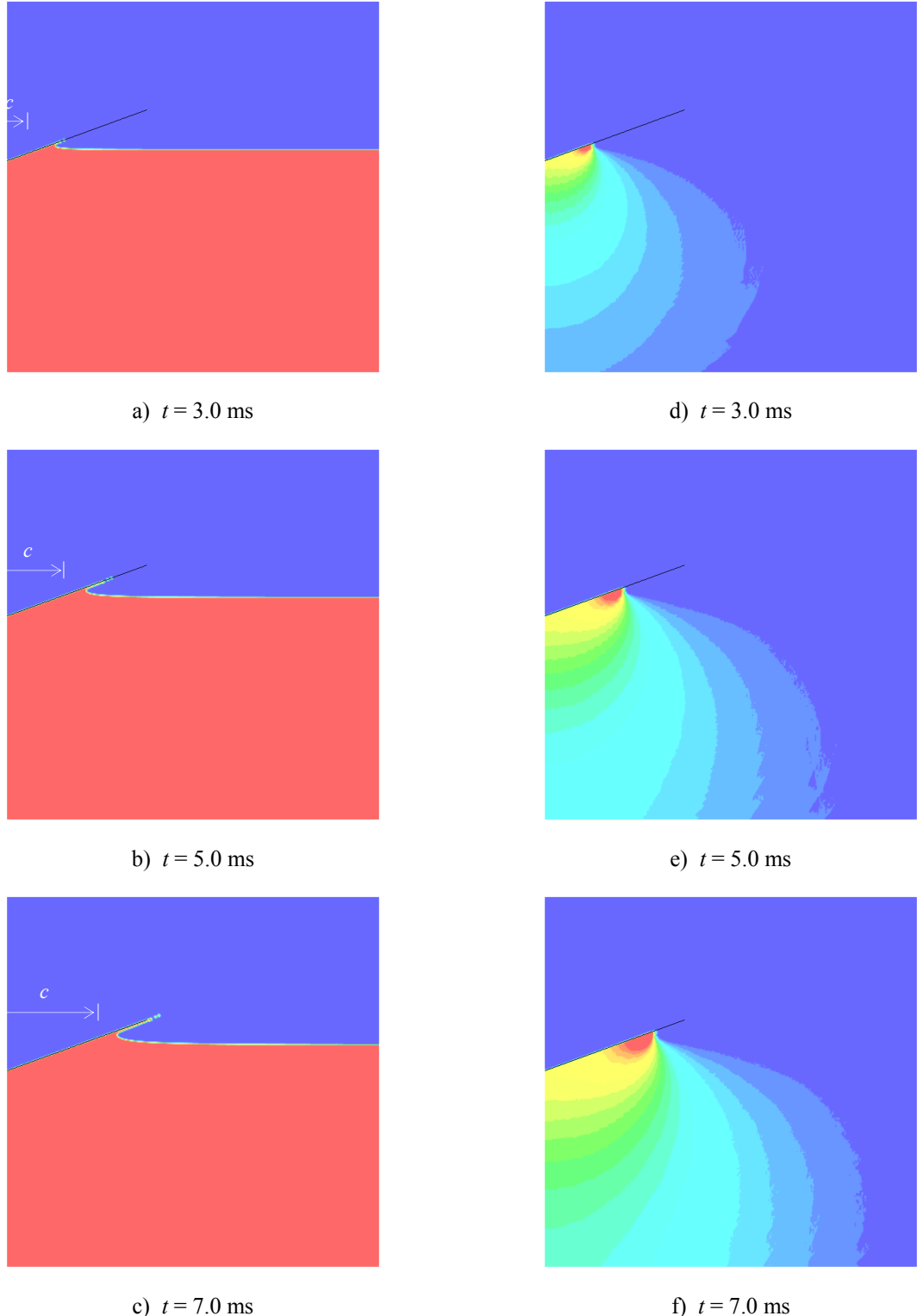


**Figure 5.1.** Left: water free surface elevation. Right: water pressure.

Elevation of the water free surface and pressure distribution were plotted in Figure 5.1 at  $t = 3.0$ ,  $5.0$  and  $7.0$  ms from the impact. Clearly, no evidence of numerical leakage was observed during the simulation. Figure 5.1 (d), (e) and (f) also show that the maximum hydrodynamic pressure, indicated as a red colored area, is located at the contact surface between the water and the structure. This pressure peak propagates from the keel to the chine of the hull during the impact stage following the contact point  $c(t)$ . Figure 5.2 depicts the local pressure time history at location  $x = 0.107$  m on the bottom hull surface measured from the keel. The temporal evolution of the pressure is characterized by a localized pressure peak at time  $t = 5$  ms approximately, at which  $x = c(t)$ , followed by a distinctly lower and relatively uniform pressure. FE results were compared with the analytical solution of Zhao and Faltinsen [6].

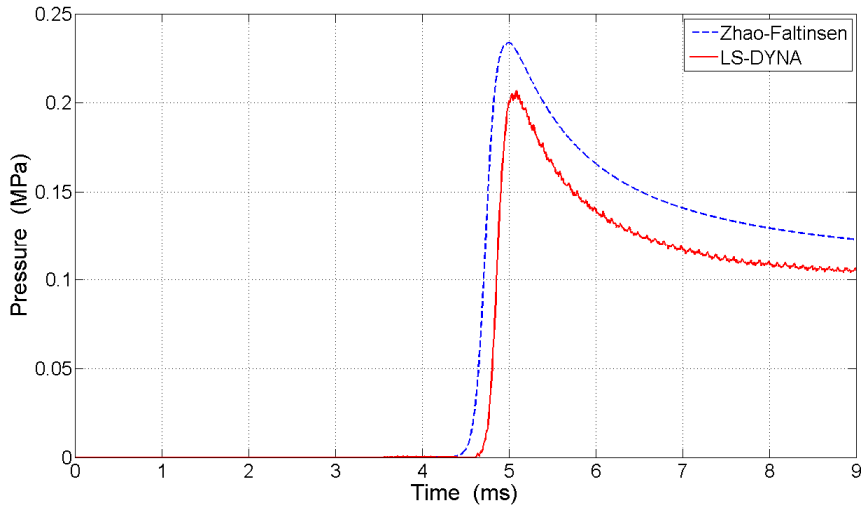


**Figure 5.2.** Pressure time history at  $x = 0.107$  m ( $\beta = 20^\circ$ ,  $V = 5$  m/s).

Notice that the theoretical pressure was slightly higher than that obtained using LS-DYNA. According to the analytical model, the maximum pressure was close to 0.23 MPa while the maximum numerical pressure was 0.20 MPa, approximately. The difference between both models was in the order of 13 % which is in accordance with the results presented in [17] for FE models with similar mesh densities. The effect of capturing the final 13 % of the pressure peak may result in a dramatic increment of the computational cost. In addition, the contribution of the very pressure peak to the dynamic structural response is thought to be small; therefore, lower mesh densities can be accepted [17]. On the other hand, experimental results [23] demonstrated that the maximum pressure measured during the impact of a rigid wedge with  $20^\circ$  at 5 m/s was in the range 0.155 - 0.208 MPa, which is consistent with the FE results.

Therefore, it was concluded that no further increase of the mesh density was required and the selected contact stiffness ( $4.5 \text{ GPa/m}$ ) and damping (0) were appropriate for this case.

Another interesting study case is the rigid hull with deadrise angle  $\beta = 10^\circ$  and vertical velocity  $V = 5 \text{ m/s}$ . This case represented a more challenging problem in terms of modeling since the pressure peak was more pronounced than that in the previous case (Figure 5.3). The increment in the pressure peak was a consequence of a smaller impact angle. As a result of the reduction of pressure peak width, the uniform fluid element size was reduced to  $dx = 0.2 \times 10^{-3} \text{ m}$ . The resulting contact stiffness was  $k_D = 11.25 \text{ GPa/m}$  and no damping was selected. The simulation time corresponding to the impact stage was 4.5 ms with a computational cost of 10 hours approximately. By comparison with analytical results, this FE model was able to capture about the 78 % of the theoretical pressure peak. The maximum experimental pressure, corresponding to this impact case, was in the range 0.523 - 0.754 MPa [23] which showed better correlation with FE results than with theoretical results. The expanding pressure peak can be observed in Figure 5.4. Notice that the pressure peak width increased with time, consistent with the analytical model (see Figure 3.2). Eventually, more and more elements are within the pressure peak width allowing the model to capture a higher percentage of the pressure peak. As a result, the maximum pressure increased from 0.7 MPa at 1.6 ms to 0.8 MPa at 3.0 ms.

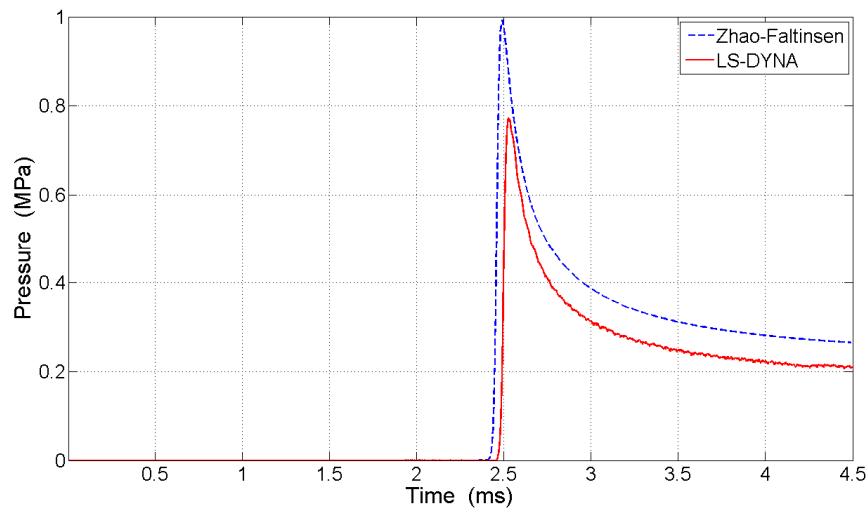


**Figure 5.3.** Pressure time history at  $x = 0.111 \text{ m}$  ( $\beta = 10^\circ$ ,  $V = 5 \text{ m/s}$ ).

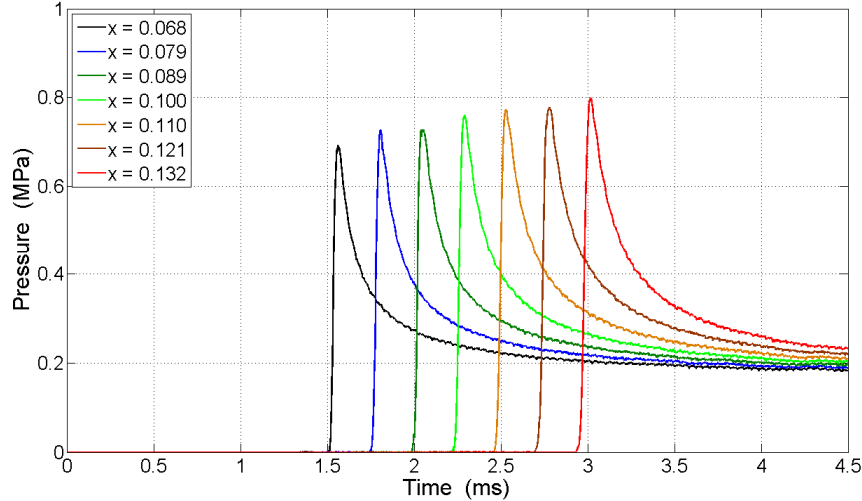


**Figure 5.4.** Propagation of the expanding pressure peak.

## 5.2 HYDROELASTIC IMPACT OF METALLIC HULLS

This section presents the results of FE simulations of water impacts of linear elastic hulls using LS-DYNA. The hull structure was modeled as an Euler beam using an isotropic ELASTIC material and simply supported boundary conditions. The beam was considered to be made of steel with mass density  $\rho_b = 7850 \text{ kg/m}^3$ , modulus of elasticity  $E = 21 \times 10^{10} \text{ N/m}^2$ , constant thickness  $h = 6 \times 10^{-3} \text{ m}$  and length between supports  $L = 0.2 \text{ m}$ . These properties were selected for comparison purposes with published results [8, 9]. The deadrise angle was  $\beta = 10^\circ$  and the impact velocity  $V = 5 \text{ m/s}$ . Mesh density, contact stiffness and damping were selected the same to those corresponding to the rigid case in Section 5.1 ( $dx = 0.2 \times 10^{-3} \text{ m}$ ,  $k_D = 11.25 \text{ GPa/m}$  and  $\xi = 0$ ). Initially, the simulation time was set in 5.0 ms (based on analytical results for the impact stage). Later, the analysis was extended to include the penetration stage. The computational cost of the simulation was in the order of 10 days.

### 5.2.1 The Impact Stage

Previously, the impact stage was defined as the time it takes the hull length to wet completely. In other words, it is the time required for the contact point ( $c(t)$ ) to travel from the left to the right beam support. When the contact point reaches the right support ( $c(t) = L$ ), the impact stage ends and the penetration stage begins. The left column of Figure 5.5 shows the water surface at  $t = 0.75, 3.0$  and  $4.75 \text{ ms}$  while the right column illustrates the corresponding structural deformation. The deflected shapes represent the displacement of the structure relative to its rigid body position (dashed line).

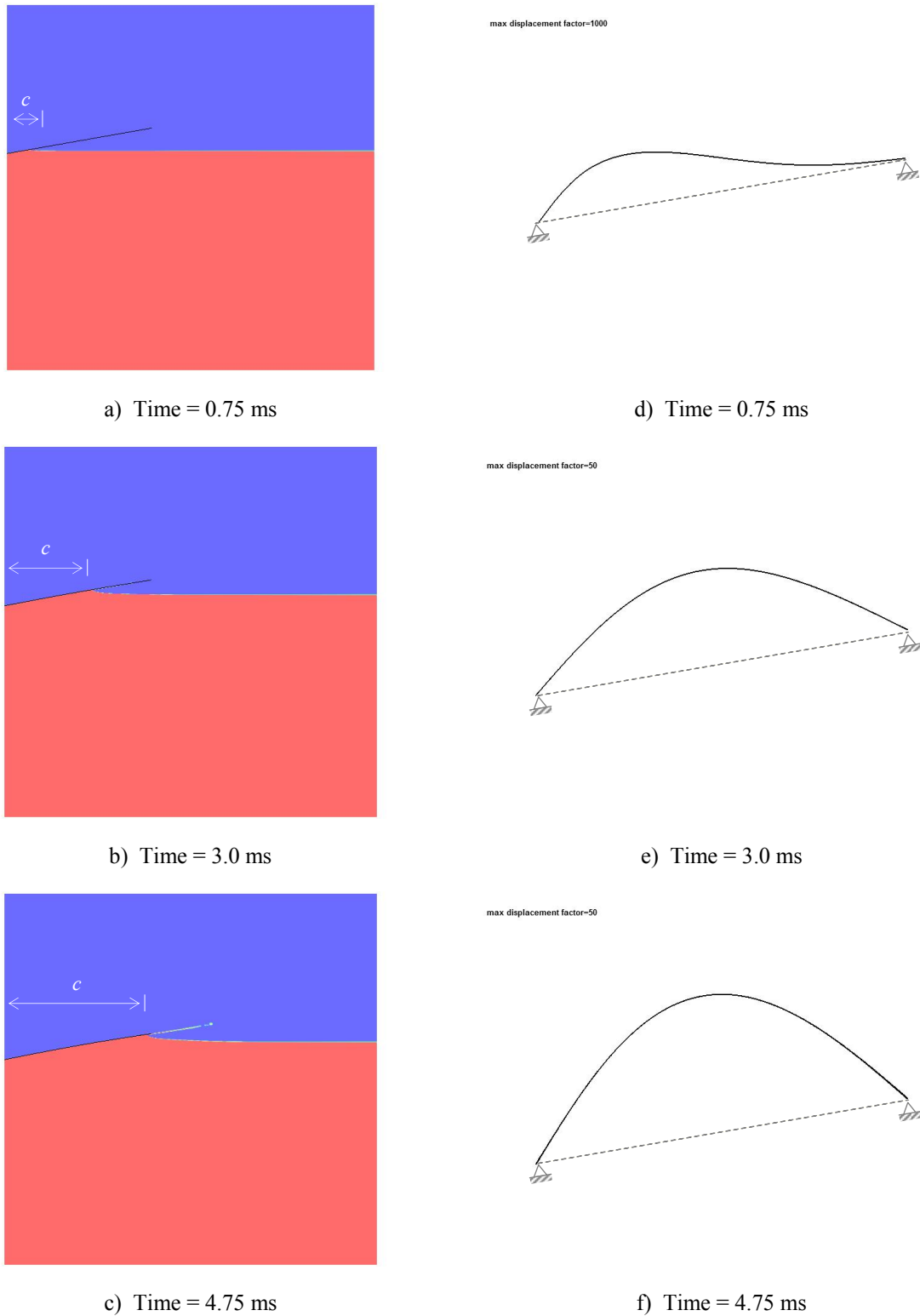


**Figure 5.5.** Left: Water free surface elevation. Right: Hull deflection (with scale factor).

Clearly, at early stages (Figure 5.5d) the hull deflection included the contribution of several free vibration mode shapes. But at advanced stages (Figure 5.5e and 5.5f) the structural deflection was governed mostly by the first mode shape. These results were verified later using the analytical model described in Chapter 3. The duration of the impact stage was estimated in 4.8 ms approximately, which corresponds to the time that the pressure peak was sensed in the model by the numerical pressure sensor located on the element at the right support (see Section 4.4). Figure 5.6 shows the time history of the hull deflection at three different locations on the hull length,  $x = 0.05, 0.10$  and  $0.15$  m, measured from the left support ( $L/4, L/2$  and  $3L/4$  respectively). The results correspond to the impact stage ( $0 \leq t \leq 4.8$  ms). As expected, the structural response was not symmetric and the maximum deflections occurred at mid-span of the beam length ( $x = 0.1$  m).

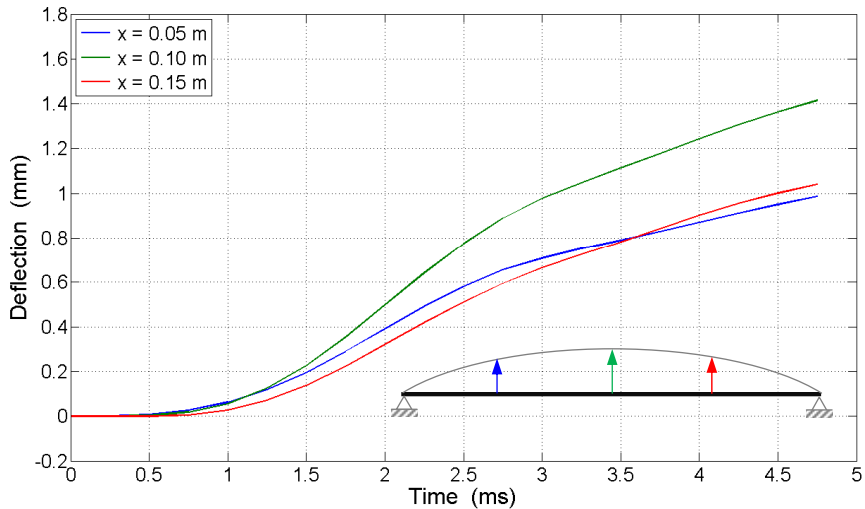


**Figure 5.6.** Hull deflection time history ( $\beta = 10^\circ, V = 5$  m/s).

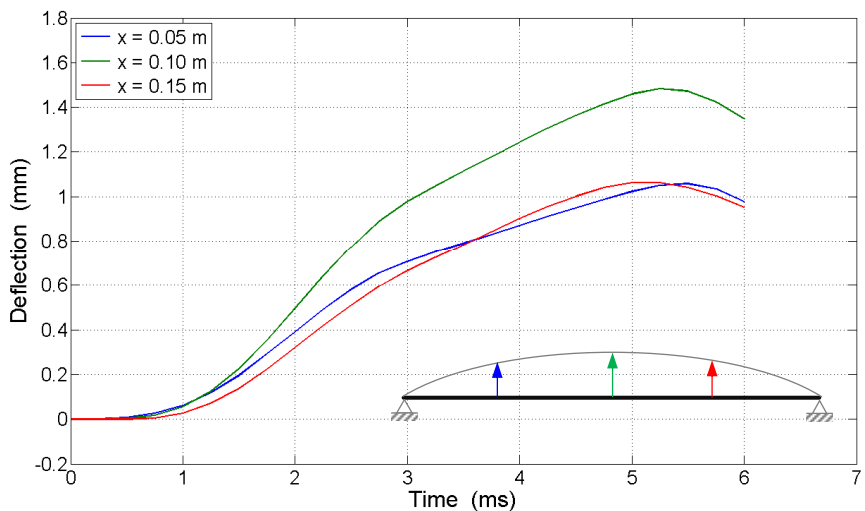


**Figure 5.7.** Maximum hull deflections.

Figure 5.7 shows the results of the previous analysis extended to 6 ms in order to demonstrate that the maximum structural deformations took place immediately after the beginning of the penetration stage, when the hull length was completely wetted ( $t = 5.3$  ms approximately). To validate these results, the hydroelastic model presented in Chapter 3 was used to solve the same impact situation. The number of terms used to approximate the hull deflection was  $n = 3$ . Results demonstrated that only the first three generalized coordinates had a significant effect in the structural response. The duration of the impact stage in terms of the wetted length was  $c = 1.0$ , in non-dimensional variables, or  $c = 0.2$  m, in dimensional variables. Note that the system of differential equations and the corresponding initial conditions derived in Chapter 3 were formulated using  $c$  as the independent variable and not time. The temporal variable  $t$  was obtained as a result of the solution of the ODE system (3.52)-(3.54), as shown in Figure 5.8. In this case, the relationship between  $t$  and  $c$  was quasi-linear which indicated a relative rigid impact. The time required to complete the impact stage was in the order of 4.6 ms which was very close to the time predicted by the FE model. The generalized coordinates  $a_n$  were plotted in Figure 5.9 as a function of time  $t$ . Clearly, the first coordinate  $a_1$  (blue line) dominated over  $a_2$  (green line) and  $a_3$  (red line). In fact,  $a_3$  was approximately zero, which confirmed that no additional terms were needed in the expansion approximations. However, at initial impact stages ( $t \leq 1.0$  ms), the three generalized coordinates were similar in magnitude. Therefore, the hull deformation included the contribution of the three dry mode shapes,  $\psi_1$ ,  $\psi_2$ , and  $\psi_3$ . This can be seen in Figure 5.10 for four different values of the wetted length,  $c = 0.02$ ,  $0.03$ ,  $0.04$  and  $0.05$  m. The small circle on each curve indicates the location of the contact point  $x = c$ .

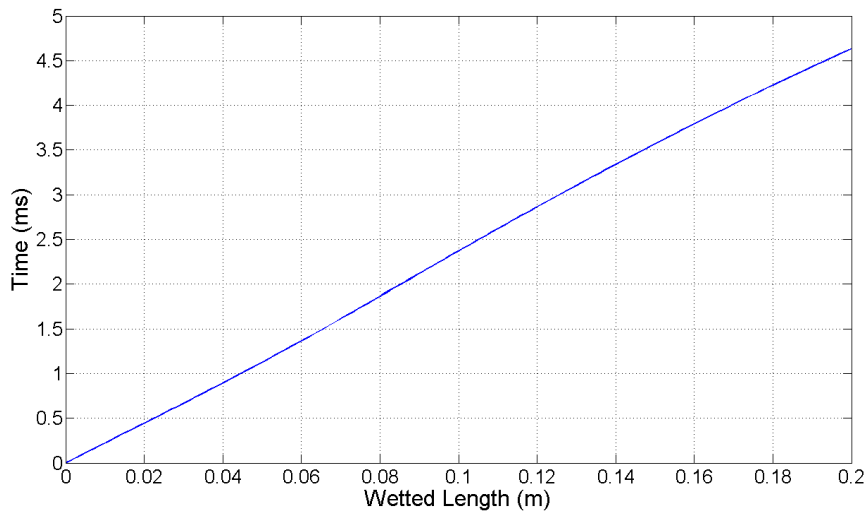


**Figure 5.8.** Time history of the wetted length.

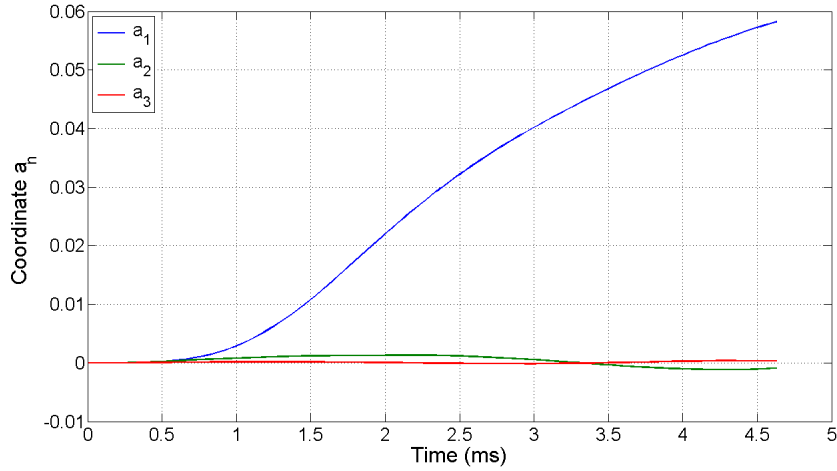


**Figure 5.9.** Time history of generalized coordinates.

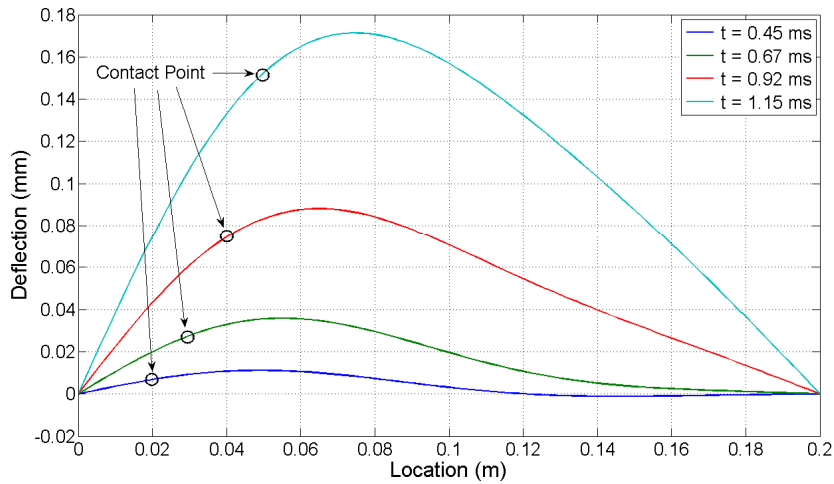


**Figure 5.10.** Deflected shapes at initial stages.

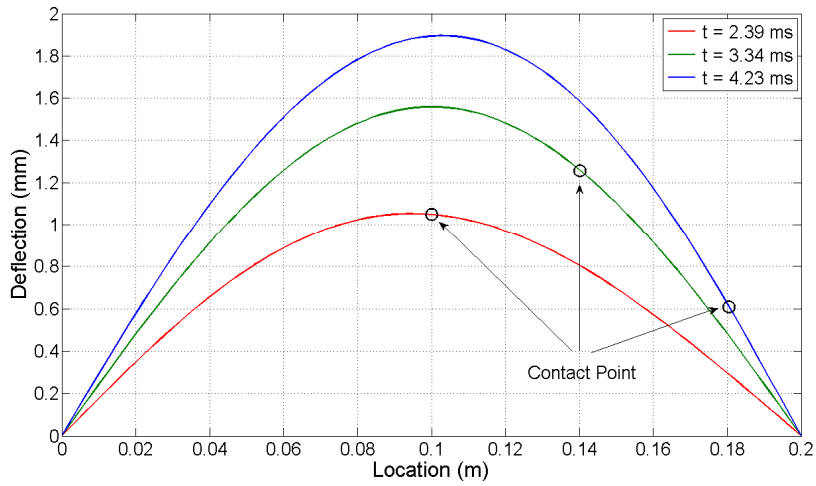


**Figure 5.11.** Deflected shapes at advanced stages.

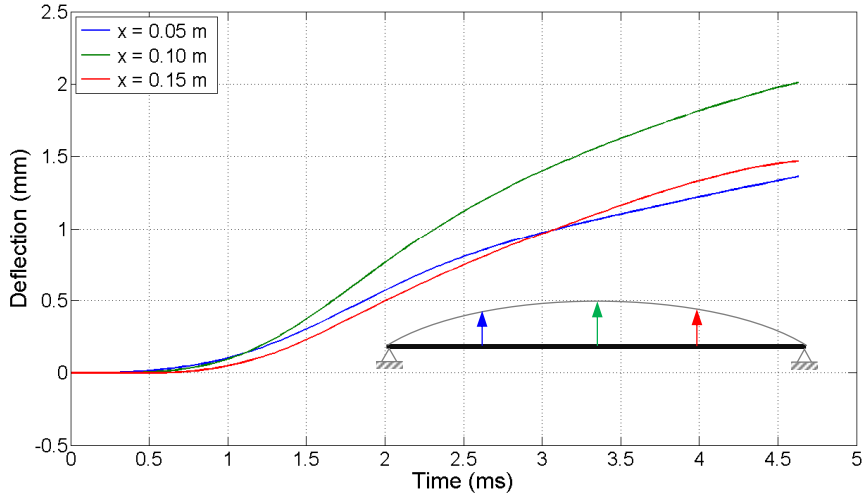


**Figure 5.12.** Hull deflection time history ( $\beta = 10^\circ$ ,  $V = 5 \text{ m/s}$ ).

On the other hand, at advanced stages ( $t > 1.0 \text{ ms}$ ), coordinate  $a_1$  dominated over  $a_2$  and  $a_3$  and the hull deformation basically adopted the shape of the first dry mode shape  $\psi_1$  (Figure 5.11). These results were in accordance with those obtained with LS-DYNA. Figure 5.12 shows the time history of the hull deflection obtained from the analytical model at  $x = 0.05, 0.10$  and  $0.15 \text{ m}$  correspondingly to Figure 5.6. These results also demonstrated good correlation with FE simulations. However, at this point two major issues required special attention: 1) the accuracy of the FE results and 2) the computational cost of the simulation. First, it was found that the structural deformations computed using Korobkin's model were slightly higher than those obtained with LS-DYNA, analogous to the impact pressure for rigid hulls. According to the theoretical model, the maximum mid-span beam deflection was close to 2 mm (Figure 5.12) while LS-DYNA predicted approximately 1.5 mm at the same location (Figure 5.6). The difference was a consequence of the calculation of the hydrodynamic pressure during the impact stage. The integral of this pressure between time  $t = 0$  and  $t$  is defined as the impulse and represents the momentum by unit area applied to the structure. Figure 5.13 illustrates the difference in the predicted impact pressure at a particular location. Clearly, the momentum applied to the FE structure during the impact was relatively lower than that applied to the beam in the analytical model. Consequently the FE deformations were significantly smaller. Second, the 10 days of computational time of this simulation was considered excessively expensive, based on the scope of this work which requires including in the analysis the penetration stage of the impact.

The most effective method to reduce the simulation time is to decrease the FE mesh density. But decreasing the mesh density in the interior domain may affect the accuracy of the numerical results; in particular the impact pressure peak might not be captured with a coarser mesh. To determine the

sensitivity of the structural response to the very pressure peak, a simple comparative analysis was conducted using a FE model with lower mesh density. The new model was developed using a uniform mesh element size 6.25 times larger than the element size used in the current model ( $0.20 \times 10^{-3}$  m). The structural deflection at  $x = 0.10$  m is shown in Figure 5.14 for both element sizes. The maximum mid-span deflection reduced from  $1.50 \times 10^{-3}$  m to  $1.25 \times 10^{-3}$  m (16 % approximately) and occurred exactly at the end of the impact stage. On the other hand, the reduction of computational time was in the order of 10 times (from 10 days to 1 day). Based on these results, it was concluded that the pressure peak had no significant effect on the dynamic response of the hull structure. Deflections can be accurately predicted using coarser meshes than that required to capture the pressure peak and the reduction of computational cost obtained by decreasing the mesh density can be very significant.

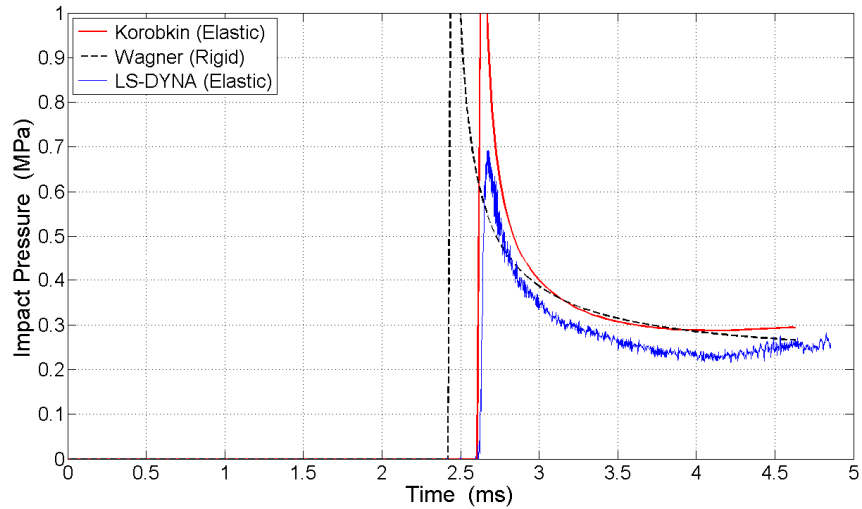


**Figure 5.13.** Hydrodynamic pressure (impact stage).

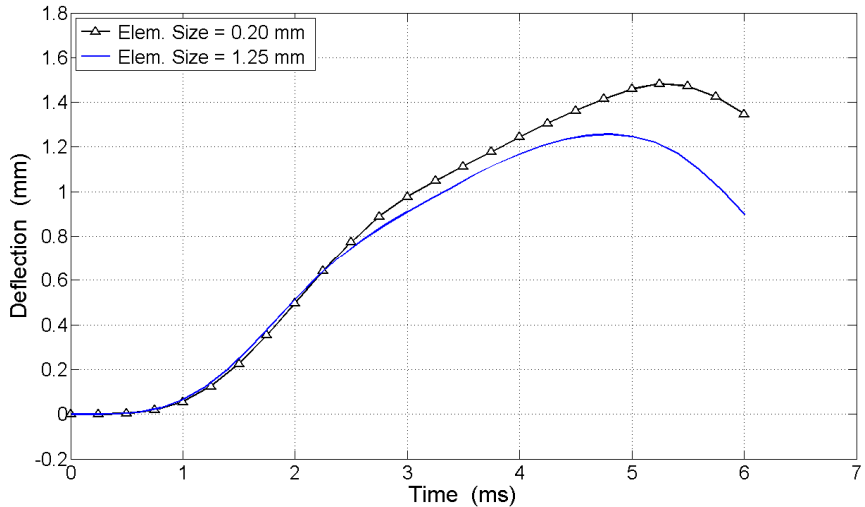


**Figure 5.14.** Hull deflection for two different mesh densities ( $x = 0.1$  m)

### 5.2.2 The Penetration Stage

In order to investigate the structural response of the elastic hull during the penetration stage, the previous FE analysis was extended to 20 ms. Figure 5.15 illustrates how after the bottom hull surface was totally wetted, the structure started to vibrate with a damped oscillatory motion. This vibration induced by the slam event is known as whipping. The damping was related to the dissipation of energy during the impact due to small changes of fluid mass density; even though this was assumed to be incompressible (no structural damping was considered). From Figure 5.15, the period of vibration of the wet structure  $T_W$  was estimated close to 6.8 ms. The damping ratio was calculated using the logarithmic decrement method which was 0.18 approximately. The period of vibration corresponding to the dry structure  $T_D$ , obtained using a single degree of freedom damped model, was 2.9 ms ( $T_W \approx 2.3 T_D$ ). The hydrodynamic loads applied to the hull structure during the impact had a similar effect of incrementing its mass about 5 times. This is known as the added mass effect. As time increased, the structural response tended to a state of constant deformation. The bending stresses induced by the impact and the hull vibration are shown in Figure 5.16. As expected, the maximum stresses occurred simultaneously with the maximum deformations. The peak stress computed at  $x = 0.1$  m was 220 MPa approximately. This was selected as the critical location in terms of maximum stresses for fatigue analysis. Results, showed in Figure 5.15 and Figure 5.16, correspond to a single impact event. Under multiple impacts or repeated impacts, as experienced in rough sea conditions, the result of structural vibrations may be more pronounced. As a consequence of these oscillating stresses, fatigue analysis on the hull structure must be conducted. In Chapter 6 a new model based on the Rainflow cycle counting method [27] and Miner's Rule [26] is proposed for the prediction of the maximum number of impacts (cycles) to fatigue failure.

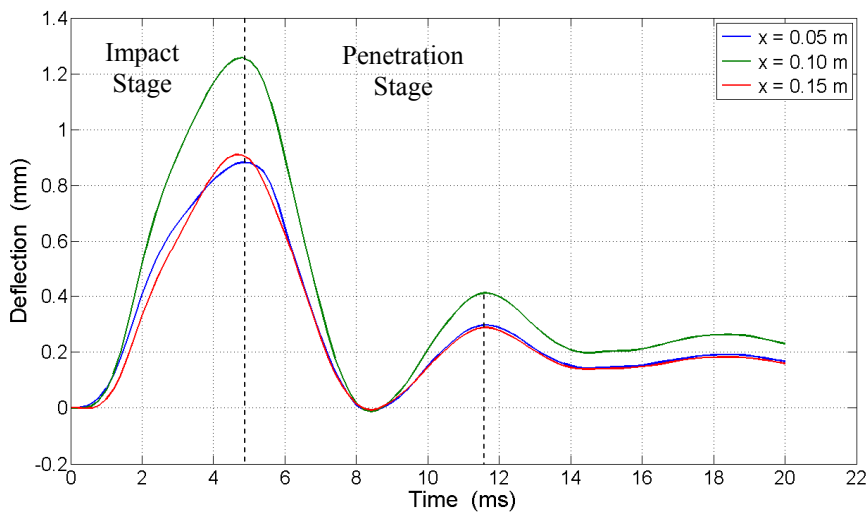


**Figure 5.15.** Hull deflection including the penetration stage.

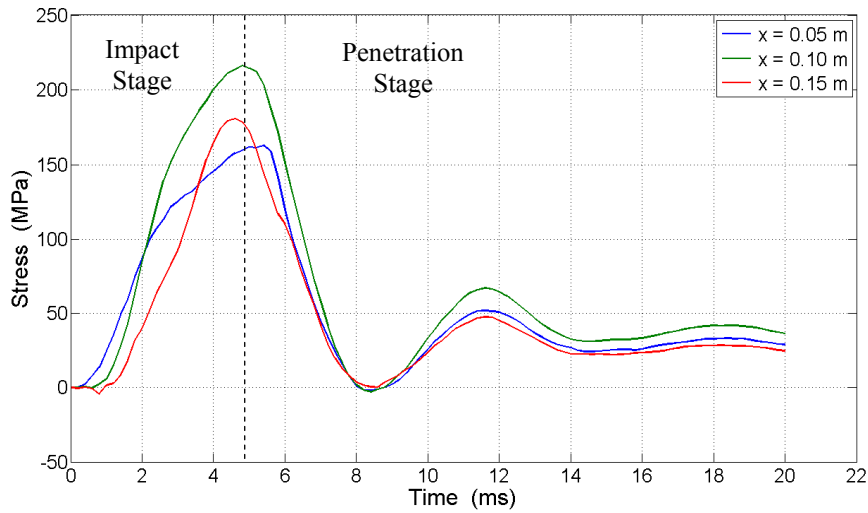


**Figure 5.16.** Hull stresses including the penetration stage.

### 5.3 HYDROELASTIC IMPACT OF SANDWICH HULLS

The sandwich composite hull FE model is shown in Figure 5.17. It consisted of two layers of 4-node shell elements (top and bottom face sheets) attached by four layers of 8-node solid elements (core). The face sheets were modeled using an orthotropic elastic material formulation while the core was assumed to be isotropic linear elastic. Mechanical properties of the sandwich composite materials in local coordinate system ( $\eta, \zeta$ ) are listed in Table 5.1.

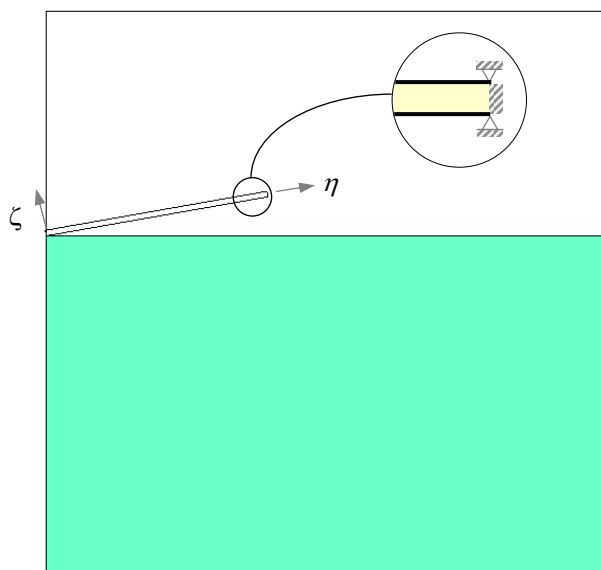


**Figure 5.17.** FE model of a sandwich composite hull.

**Table 5.1.** Mechanical properties of sandwich composite beams.

Property	Face Sheet	Core
Mass density (kg/m <sup>3</sup> )	1117	96
Longitudinal modulus of elasticity (MPa)	40000	21.5
Transversal modulus of elasticity (MPa)	40000	21.5
Shear modulus of elasticity (MPa)	10000	9.0
Poisson's ratio	0.35	0.3

Data correspond to carbon fiber-polyurethane foam core sandwich composite [24].

Boundary conditions were simply supported for the face sheets and clamped for the core (Figure 5.17). Beam's dimensions were selected similar to those described in Section 5.2 for metallic hulls: face sheet thickness  $h_f = 0.5 \times 10^{-3}$  m, core thickness  $t_c = 5 \times 10^{-3}$  m ( $2h_f + t_c = 6 \times 10^{-3}$  m), and length between supports  $L = 0.2$  m. Other parameters including deadrise angle, impact velocity, mesh density, contact stiffness and fluid properties were chosen from the previous model ( $\beta = 10^\circ$ ,  $V = 5$  m/s,  $dx = 1.25 \times 10^{-3}$  m,  $k_D = 0.18$  GPa/m and  $\xi = 0$ ). The impact stage was estimated in 5.5 ms approximately (Figure 5.18) and the total simulation time was set to 20 ms. Figure 5.19 shows the time history of transversal deflections ( $\zeta$  direction) for three different locations on the beam span. Note that the deflections were significantly larger than those in Figure 5.15 due to the lower stiffness of the materials. Also note that the whipping effect (vibration) was more pronounced in the sandwich beam, especially during the penetration stage. In this case, the time of maximum deflections became considerably different among the three locations, as a consequence of the large deformations.

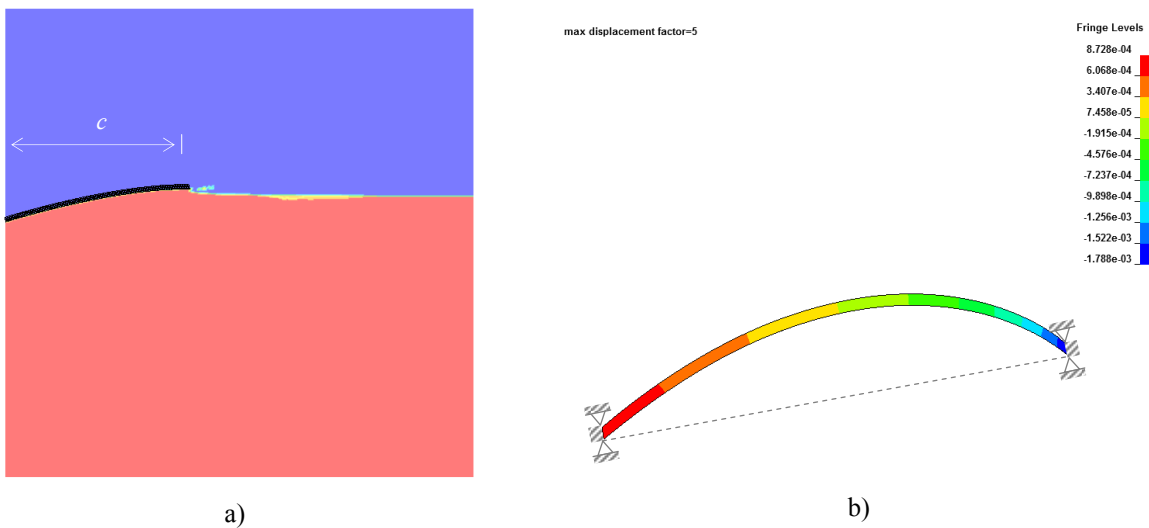


**Figure 5.18.** a) Water free surface elevation, b) Core shear stresses (MPa).

In sandwich structures, the core is assumed to carry all shear loads while the face sheets provide the stiffness in the longitudinal direction ( $\eta$  axis). Additionally, experimental results on fatigue of sandwich composites [24, 31], demonstrated that the predominant mode of failure for flexural cyclic loading was core shear. Based on that, and knowing that the maximum shear stresses in the sandwich composite beam will occur close to the supports (for these particular boundary conditions), Figure 5.20 was obtained. The critical location was identified near to the right support with a maximum shear stress of 1.8 MPa at 5.5 ms approximately. The maximum shear stress near the left support was significantly smaller, 1.3 MPa at 7.5 ms. Note that these maximum stresses took place after the impact stage, in other words, after the beam was completely wet. As a result, both locations within the sandwich core were selected for fatigue life assessment in Chapter 6.

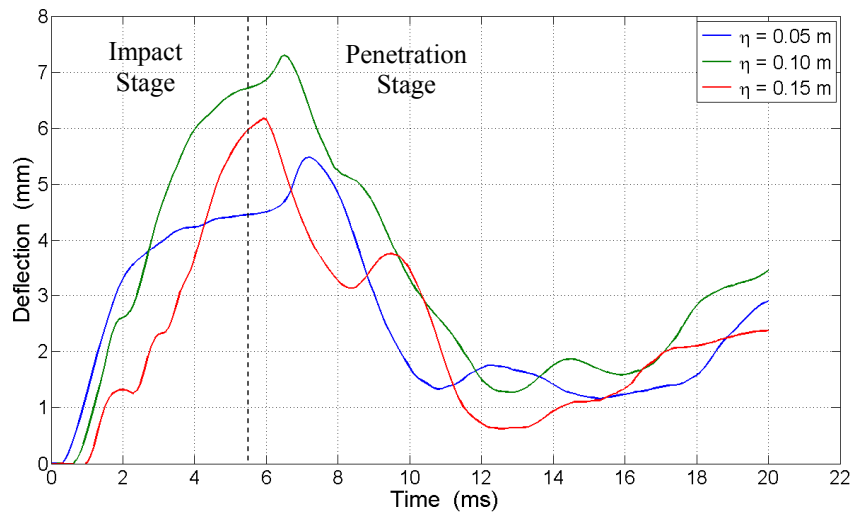


**Figure 5.19.** Sandwich hull transversal deflections ( $\zeta$  axis).

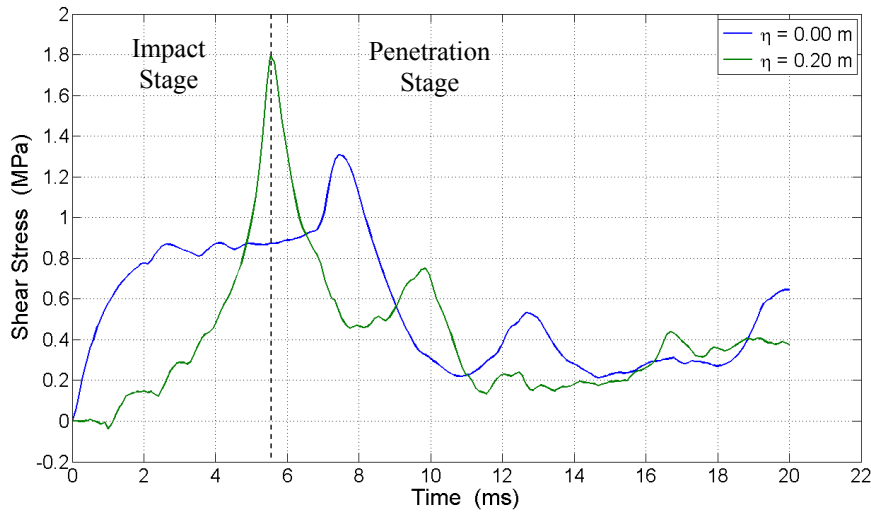


**Figure 5.20.** Core shear stresses at beam supports.

## CHAPTER 6. FATIGUE LIFE PREDICTION FOR REPEATED IMPACTS

In this chapter a new approach based on the Rainflow cycle counting method [27] and Peak Over Threshold (POT) stress extrapolation analysis [32] is proposed for the prediction of fatigue life (number of impacts to failure) of a hull structure. Fatigue life is estimated using a linear damage accumulation model and compared with a non-linear model based on fatigue modulus degradation. First, an introduction to POT analysis to extrapolate stress time histories is presented along with a brief description of the Rainflow method. Later, fatigue analysis, conducted on selected critical locations of metallic and sandwich composite structures, is discussed.

### 6.1 FATIGUE LIFE PREDICTION APPROACH

The stress time histories obtained in Chapter 5 for a single impact event can be extrapolated to account for multiple impacts of similar characteristics (deadrise angle, impact velocity, etc.). The extrapolation can be done using one of the following approaches: a) simply repeating the load history obtained from a single impact until structural failure or b) “randomly” modifying high peaks and low valley using statistical extreme value theory (POT model). Both extrapolation approaches require extracting peaks and valleys, also called turning points (TP), from the stress history. It is also recommended to remove small amplitude cycles to reduce computational cost because they are assumed to cause negligible damage. In addition, frequency content in the stress time history is not considered. In this thesis, the POT extrapolation approach was used. POT methods have the capability to incorporate in the analysis statistical data obtained from real load measurements. From the extrapolated results, stress cycles were extracted and counted using the Rainflow method. As a result, a series of cycles and half cycles with different mean and amplitude values were obtained. Then, a damage accumulation model was used to predict the fatigue life of critical locations on the hull structure. For metallic hulls, Palmgren-Miner linear law was used because its simplicity and because it has demonstrated to work properly in metals; while for sandwich composites hulls, a damage accumulation model based on fatigue (shear) modulus degradations was selected since core shear was identified to be the predominant mode of failure. The fatigue life prediction approach proposed in this thesis is summarized in Figure 6.1.

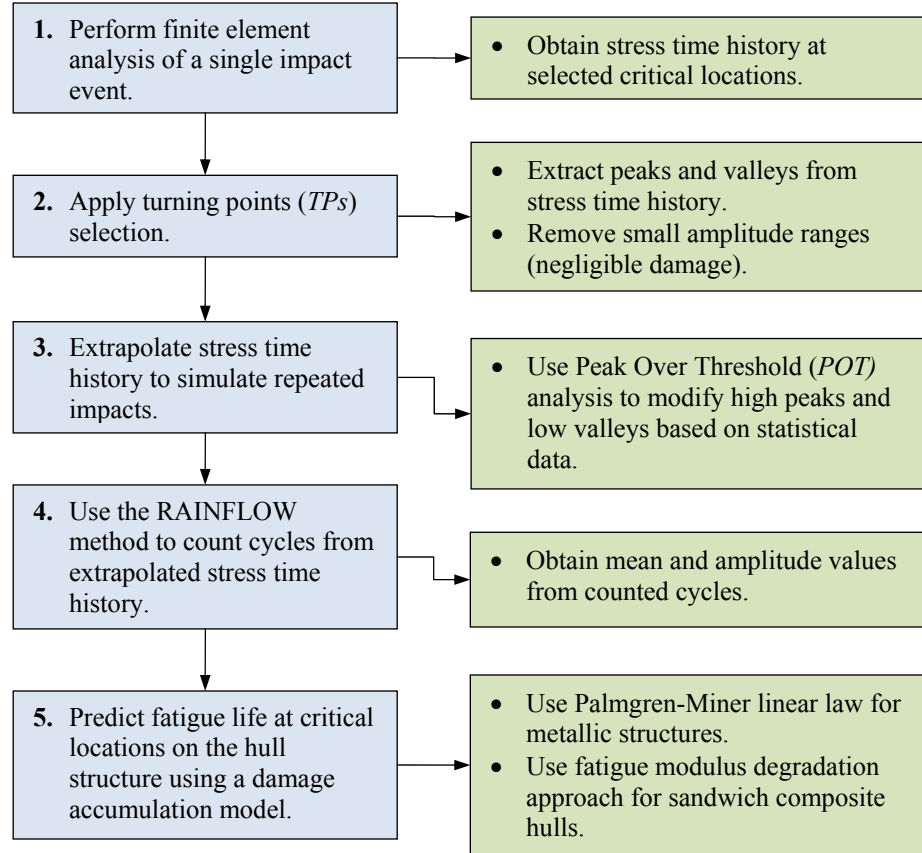


**Figure 6.1.** Fatigue life prediction approach.

## 6.2 TURNING POINTS SELECTION

The second step in the proposed life prediction approach involves the extraction of peaks and valleys (TPs) from the simulated stress history (TP filter). These TPs are simply points where the direction of the stress slope changes from positive to negative or from negative to positive. Also of interest are ranges or absolute stress differences  $|\Delta\sigma|$  between consecutive TPs. Figure 6.2 shows three repetitions or blocks of the stress time history obtained at mid-span of a steel hull hitting the water surface with  $\beta = 10^\circ$  and  $V = 5$  m/s with the corresponding TPs. The TPs associated with stress ranges smaller than 5 MPa were removed from the original data because they were assumed to cause negligible damage. Once the TPs were selected, the stress history is discarded and only the filtered data is used for subsequent steps which include extrapolation and cycle counting (Figure 6.3).

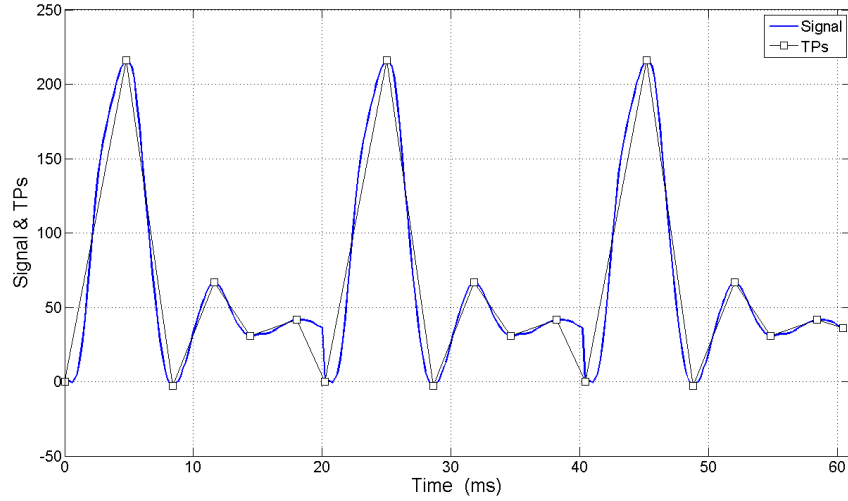


**Figure 6.2.** Stress time history at mid-span for three impact events.

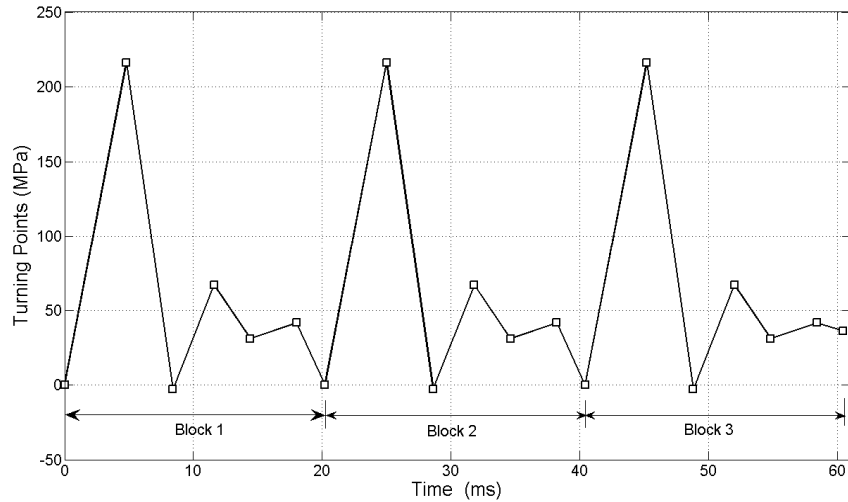


**Figure 6.3.** Selected turning points.

### 6.3 EXTRAPOLATION ANALYSIS: Peak Over Threshold Method

The stress history obtained using FE models represents only a small fraction of the structure's design life. Usually, this stress time history is repeated until failure [32]. However, this approach has the disadvantage that only the stress cycles in the FE results will appear in the extrapolation, even though other cycles might be possible. Especially, this can be critical for the most damaging large amplitude cycles. The methodology adopted in this thesis included the repetition of simulated TPs stress histories modifying maximum and minimum values. The random variation of peaks and valleys was based on

extreme value theory (POT model) and experimental data [25, 32]. The maximum stress distribution obtained from slamming measurements on high-speed aluminum catamarans follows approximately an exponential distribution (Figure 6.4). The horizontal axis corresponds to the normalized peak stress for each slam event, which was calculated as the actual peak stress  $\sigma$  divided by the mean of all peak stresses,  $\bar{\sigma}$ . The vertical axis indicates the percentage of occurrence of each normalized peak. Figure 6.4 shows that the majority of the slam events (around 70%) occurred in the range [0-1.0] of normalized peaks [32]. It also indicates that the probability of occurrence of a peak stress in the interval [1.0-2.0] is close to 20% and in the interval [2.0-3.0] close to 6%. The experimental stress distribution of Figure 6.4 was approximated using an exponential Probability Density Function (PDF) described by Equation 6.1 with a Cumulative Distribution Function (CDF) of the form of Equation 6.2. Notice that for normalized stresses, the mean value  $\bar{\sigma}$  is equal to one. The randomly generated maximum stresses are shown in Figure 6.5. The blue line corresponds to the fit equation of the form of Equation 6.1.

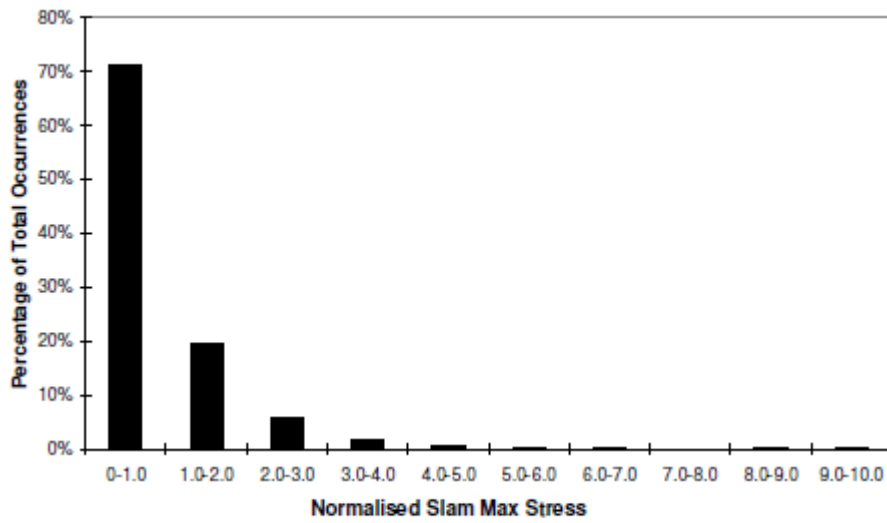


**Figure 6.4.** Maximum stress distribution for slam events [25].

$$f(\sigma) = \frac{1}{\bar{\sigma}} \exp\left(-\frac{\sigma}{\bar{\sigma}}\right) \quad (6.1)$$

$$F(\sigma) = 1 - \exp\left(-\frac{\sigma}{\bar{\sigma}}\right) \quad (6.2)$$

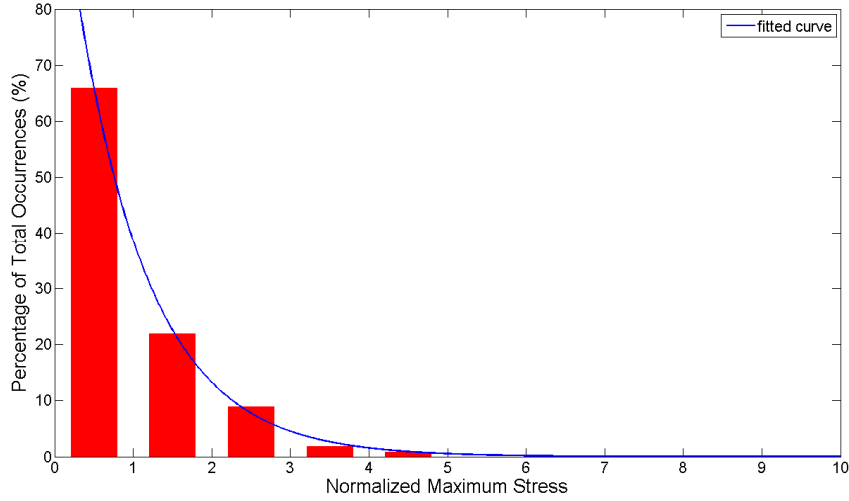


**Figure 6.5.** Randomly generated maximum stress distribution.

The exceedances above or below a certain stress level  $u$ , defined as  $Z = \sigma - u$  (Figure 6.6), can also be assumed to follow some probability distribution, for sufficient high threshold level  $u$ . Thus, normalized exceedances ( $Z/\bar{Z}$ ) were generated numerically, in this case, using a gamma distribution (Equation 6.3). The gamma distribution is a two parameter ( $k, \theta$ ) probability function widely used to model random variables in many engineering applications. The parameter  $\theta$  is the scale parameter while  $k$  is the shape parameter. The mean value is given by the product of both parameters  $\theta$  and  $k$ . For these normalized exceedances, the mean value ( $\theta \cdot k$ ) must be approximately one and the maximum value should be limited to a certain expected level. In this case, it will be assumed that no exceedances greater than 3.5 times the averaged value will occur. Based on this criteria, the parameters of the gamma distribution were selected as follow,  $\theta = 0.12$  and  $k = 9$ . Figure 6.7 shows the distribution of normalized exceedances for 10,000 impacts. Slight variations of  $\theta$  and  $k$  will produce similar distributions and the ultimate choice must be decided based on empirical data and experience. The author believes that the gamma distribution better represents the expected stress exceedances than the exponential distribution, which is a special case of the gamma distribution ( $k = 1$ ). The gamma distribution assigns the higher probability of occurrence to those exceedances that are close to the mean value and reduces the probability of those exceedances below and above the mean value, similar to a normal distribution, but not in a symmetric way. The actual stress exceedances were obtained from the normalized distribution by scaling these values with the average of all exceedances  $\bar{Z}$  (previous extrapolation). The extrapolated results were then computed as  $\sigma = u + Z$ . Threshold levels  $u_{\max}$  and  $u_{\min}$  have no physical meaning. They only define which TPs will be modified and which will remain unchanged during the extrapolation process. Therefore, the selection of

appropriate threshold levels is a difficult task which requires some engineering judgment and experience. These levels need to be chosen high enough for the extreme value theory to be a reasonable approximation, but also low enough to get a sufficient number of exceedances [32]. In this thesis, levels  $u_{\max}$  and  $u_{\min}$  were selected such that only the TPs associated with the larger stress ranges were affected (Figure 6.6). Thus, only the major and most damaging cycles will be modified during the extrapolation. As a result of this approach, an extrapolated TPs time history with random variation of its maximum and minimum values is obtained. Figure 6.8 compares the original TPs time history with the extrapolated results corresponding to  $u_{\max} = 180$  MPa and  $u_{\min} = 20$  MPa.

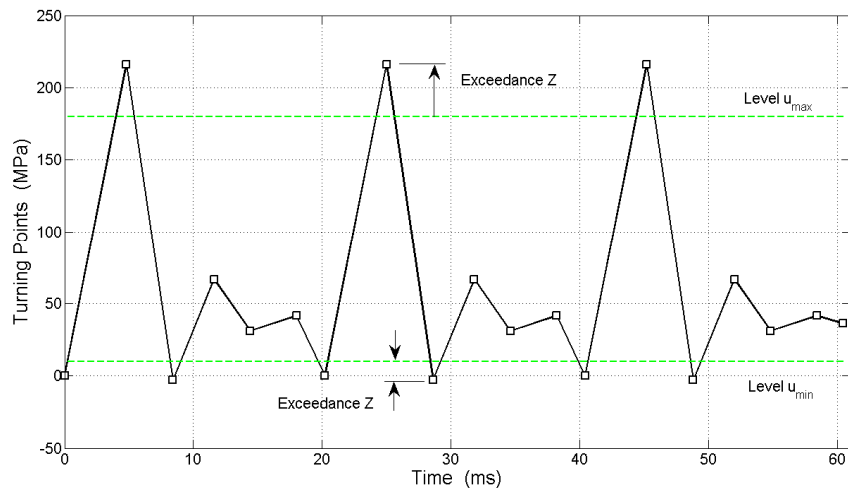


**Figure 6.6.** Exceedances above threshold level  $u_{\max}$  and below  $u_{\min}$ .

$$f(Z) = \frac{1}{\theta^k} \frac{1}{\Gamma(k)} Z^{k-1} \exp(-Z/\theta); \quad \Gamma(k) = (k-1)! \quad \text{for } Z \geq 0 \text{ and } k, \theta > 0 \quad (6.3)$$

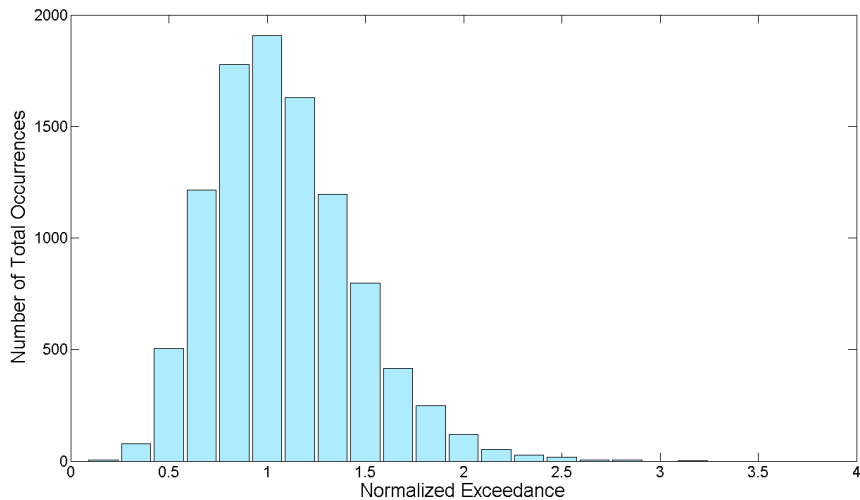


**Figure 6.7.** Distribution of normalized exceedances  $Z/\bar{Z}$  for 10,000 impacts.

Notice that two of the three TPs above the level  $u_{\max}$  increased and one decreased from their original values. The TPs below level  $u_{\min}$  were slightly affected by the extrapolation process. This is a consequence of the selected levels  $u_{\max}$  and  $u_{\min}$  which determine the magnitude of the extrapolated stresses. For instance, lower values of  $u_{\max}$  lead to higher values of extrapolated stresses. Similarly, higher values of  $u_{\min}$  also lead to higher values of extrapolated stresses. Those TPs between  $u_{\min}$  and  $u_{\max}$  remain constant during the extrapolation. As a result, a new time history is obtained by replacing the original TPs by the new extrapolated TPs. The resulting stress time history has the form of that shown in Figure 6.9 which was obtained using the same threshold levels but, in this case, for 10 impacts. This approach can be extended to include thousands of cycles, as it will be shown in the next section.

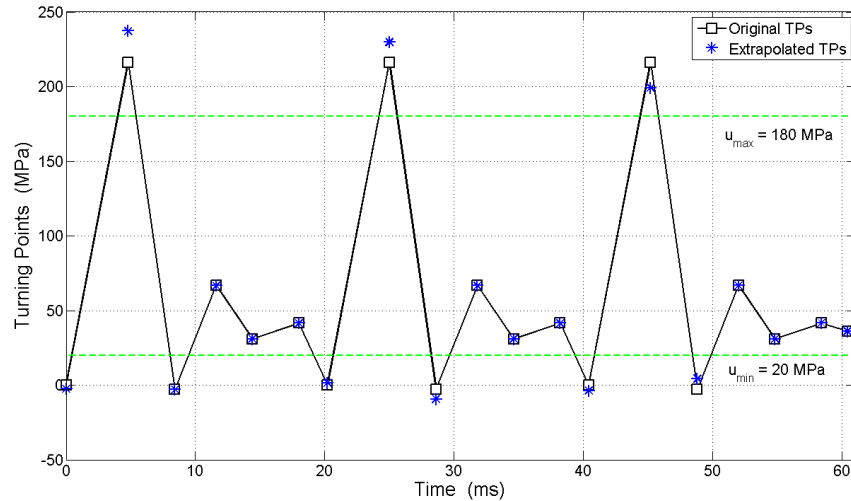


**Figure 6.8.** Original TPs history compared with extrapolated results.

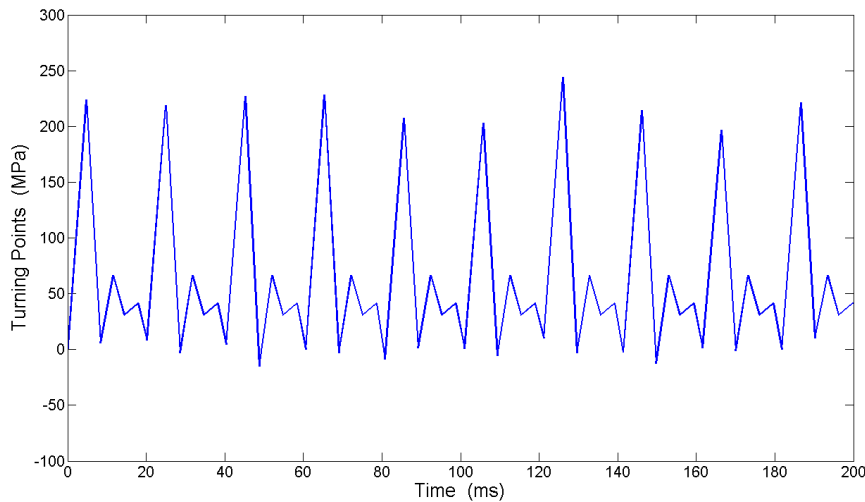


**Figure 6.9.** Extrapolated TPs time history for 10 impacts.

#### 6.4 RAINFLOW CYCLE COUNTING METHOD

The next step in the proposed life prediction approach uses the Rainflow method to count the number of cycles included in the extrapolated stress history. For irregular variations of stresses with time, such those shown in Figure 6.9, it is not clear how to isolate a cycle in terms of its mean value and amplitude so that a fatigue damage accumulation model as Miner's rule can be employed [26]. In past years, there was considerably uncertainty and debate concerning the proper procedure and a number of different methods were proposed and used. Recently, a consensus has emerged that the best approach is a procedure called Rainflow cycle counting developed in Japan around 1968 [27]. Usually, the Rainflow algorithm extracts cycles from load, stress or strain history obtained from measurements or simulations. As a result of the counting, several cycles and half cycles with different mean and amplitude values are obtained. To illustrate how the Rainflow method works, it will be used to count the number of cycles in the extrapolated stress history of Figure 6.9. For simplicity, only the first three impacts will be considered. In Figure 6.10 the TPs were labeled using capital letters (*A-T*). The ranges or absolute stress differences  $|\Delta\sigma|$  between consecutive TPs were computed and listed in Table 6.1.

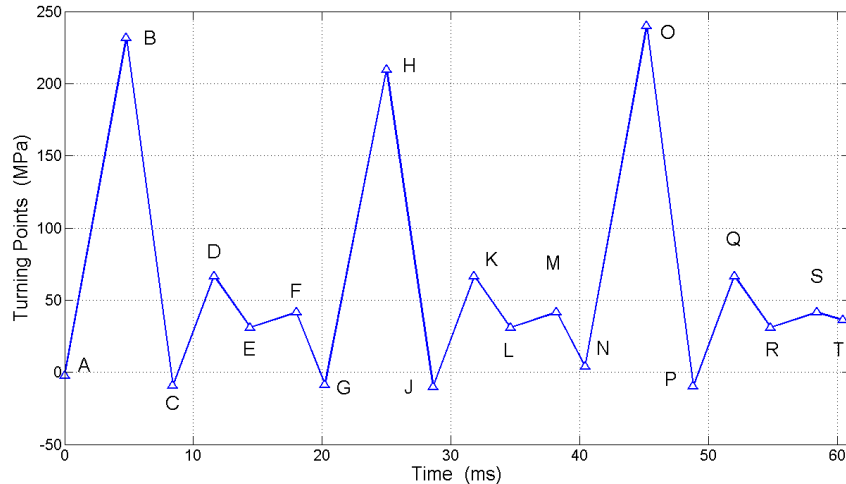


**Figure 6.10.** Extrapolated TPs labels.

**Table 6.1.** Absolute stress differences.

Event	<i>A-B</i>	<i>B-C</i>	<i>C-D</i>	<i>D-E</i>	<i>E-F</i>	<i>F-G</i>	<i>G-H</i>	<i>H-J</i>	<i>J-K</i>	<i>M-N</i>	<i>N-O</i>	<i>O-P</i>	<i>P-Q</i>	<i>S-T</i>
	<i>K-L</i>	<i>L-M</i>	<i>F-H</i>	<i>G-H</i>	<i>H-J</i>	<i>J-K</i>	<i>M-N</i>	<i>N-O</i>	<i>O-P</i>	<i>P-Q</i>				
Range (MPa)	233.9	240.4	75.6	35.7	10.6	50.0	218.3	220.1	77.0	37.4	235.9	249.7	76.2	5.4

Using these results, the counting procedure begins from the starting point  $A$  and progresses according to the following criterion: a generic valley-peak or peak-valley event  $XY$  in the stress history is counted if  $|\Delta\sigma_{XY}| \leq |\Delta\sigma_{YZ}|$ , where  $YZ$  is the following event adjacent to  $XY$ . In addition, if event  $XY$  contains the starting point, then  $XY$  is counted as half cycle otherwise it is counted as one cycle. If event  $XY$  is counted as half cycle, the first TP (peak or valley) of the event is discarded from the stress history and the starting point is moved to the next TP. If event  $XY$  is counted as one cycle, both peak and valley of that event are discarded. Every time a TP is eliminated from the history, the two adjacent TPs are automatically connected to form a new event. The remaining uncounted events are counted as half cycles at the end of the procedure. Figure 6.11 shows the Rainflow method flow chart. Note that the counting of cycles is not sequential.

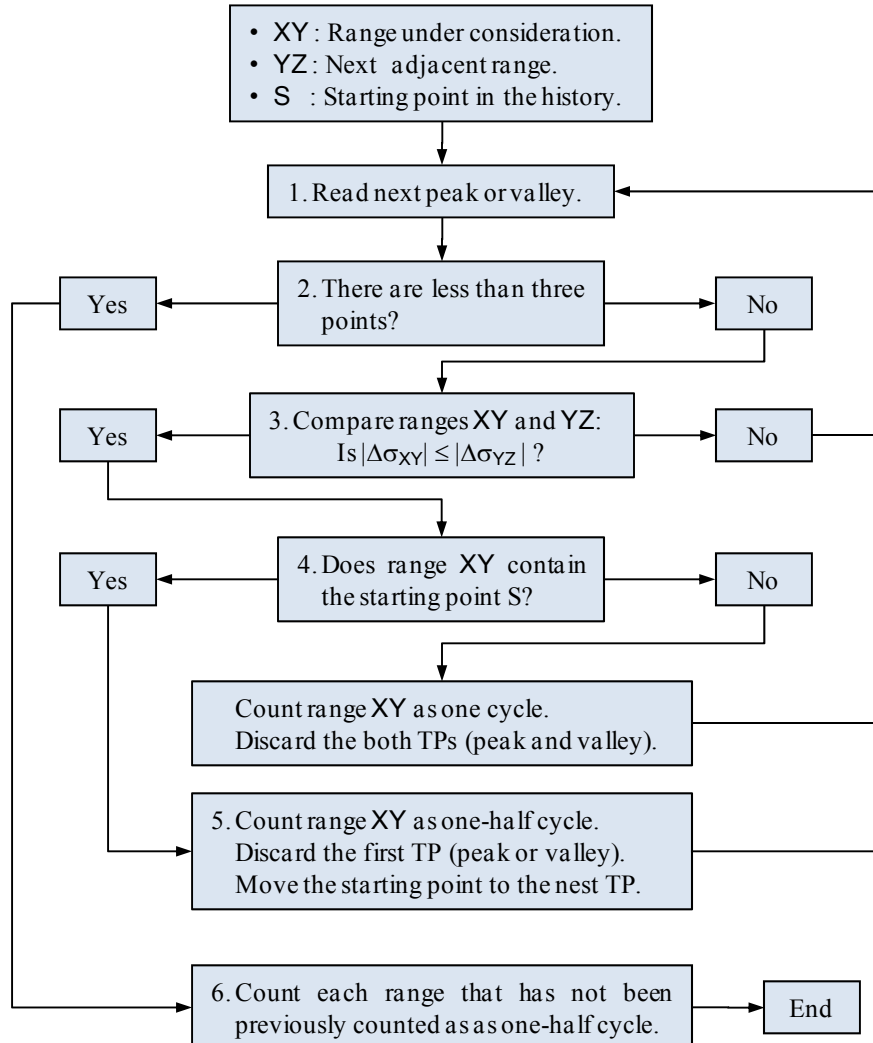


**Figure 6.11.** Rainflow cycle counting method flow chart.

For the stress history of Figure 6.10, the counting begins at the starting point *A*. Range *AB* is smaller than range *BC* (see Table 6.1), therefore, event *AB* is counted by the Rainflow method as half cycle. TP *A* is removed and the starting point is moved to *B*. On the other hand, range *BC* is greater than range *CD*; therefore event *BC* is not counted at this stage. Similarly, events *CD* and *DE* are also omitted during the first counting step. Event *EF* is counted as one cycle because range *EF* is smaller than range *FG* and it does not contain the starting point *B*. Consequently, both TPs *E* and *F* are discarded from the history, TPs *D* and *G* are connected, and the process starts again from point *B*. Figure 6.12 shows all the cycles extracted from the three impacts of Figure 6.10 using the Rainflow method. The mean and amplitude values corresponding to these cycles were summarized in Table 6.2. As a result of the counting process, five complete cycles and eight half cycles with different mean and amplitude values were extracted. For time histories with large number of impacts, it is more appropriate to use the Rainflow matrix to graphically represent the counted cycles (Figure 6.13). The Rainflow matrix is a three dimensional plot of the data listed in Table 6.2. The Rainflow matrix also shows the distribution of the extracted cycles in terms of their amplitudes and mean values.

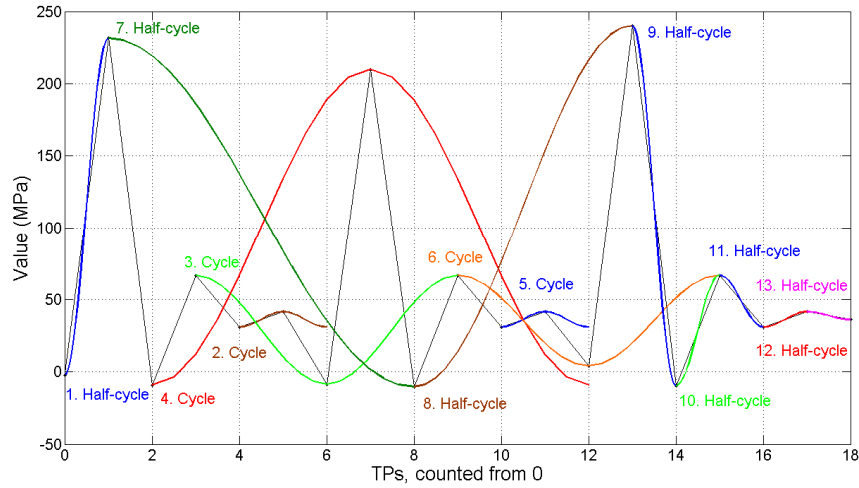


**Figure 6.12.** Rainflow cycles extracted from stress history.

**Table 6.2.** Rainflow cycles for three impacts time history.

Event	1	2	3	4	5	6	7	8	9	10	11	12	13
Mean (MPa)	114.5	36.2	29.0	100.4	36.2	35.4	110.6	114.9	115.2	28.5	48.8	36.2	38.8
Amplitude (MPa)	116.9	5.3	37.6	109.4	5.3	31.3	120.9	125.3	124.8	38.1	17.8	5.3	2.7
Nº Cycles	0.5	1.0	1.0	1.0	1.0	1.0	0.5	0.5	0.5	0.5	0.5	0.5	0.5

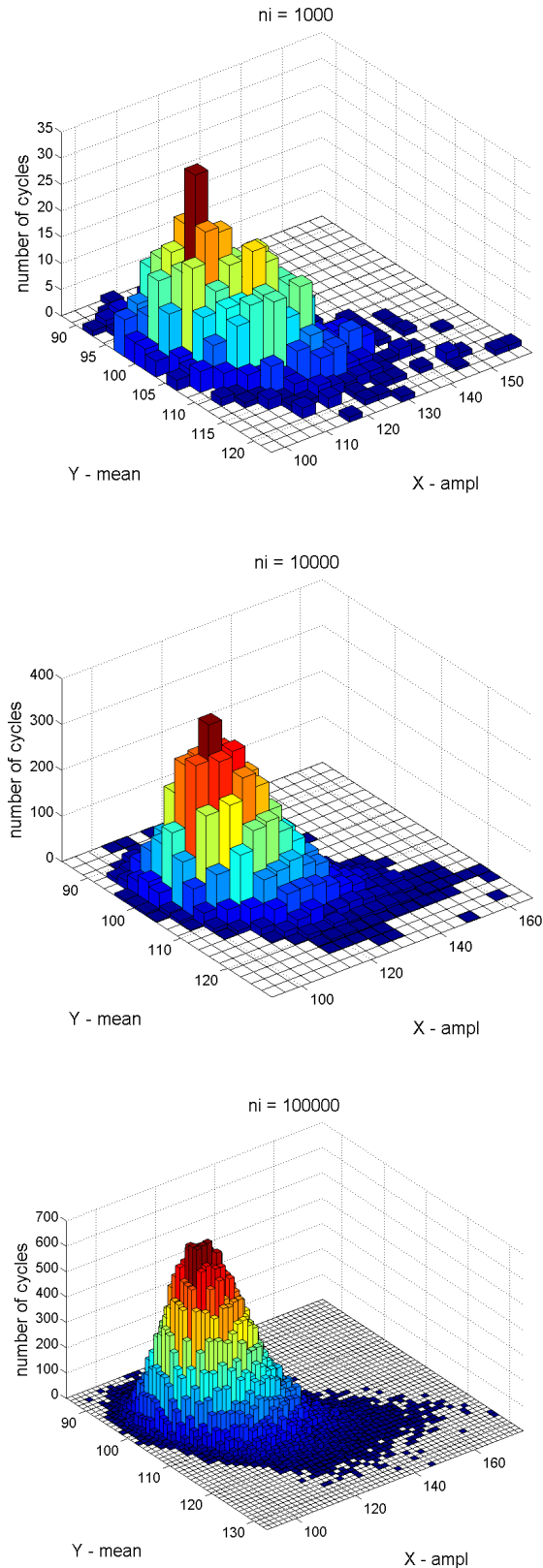


**Figure 6.13.** Rainflow matrices for different number of impacts.

The Rainflow matrices of Figure 6.13 only include those cycles modified during the extrapolation (major cycles). The damage induced in the structure by these equivalent cyclic stresses can be estimated using an appropriate damage accumulation model, depending on the material of the structure. For metallic structures Miner's Law works properly giving relatively accurate results but for composite structures, in particular those made of sandwich composite material, more complex models are needed. These topics are discussed in the next section.

## 6.5 FATIGUE MODELING: Damage Accumulation Approach

The extrapolation analysis described in previous sections can be extended to include thousands of repetitions of the simulated stress time history at a particular location. In fact, it is possible to extrapolate these stresses as many times as needed to make the structure fail at that location. To measure the effect of cyclic stresses on the structural life, several analytical models have been developed. These models are typically based on either stress versus number of cycles (S-N curves), strength degradation, stiffness reduction, cumulative damage modeling, or a combination of these approaches [30]. In this section, the fatigue life of steel and sandwich composite hulls is estimated based on two different damage accumulation models.

### 6.5.1 Damage Assessment for Metallic Hulls

For metallic structures, the most common approach used is the Palmgren-Miner criterion, or linear damage accumulation law [26]. In this approach damage is assumed to be linearly proportional to the fractional life used by different cyclic stress levels and fatigue is assumed to occur when the sum of these fractions exceeds unity. The criterion is expressed in equations 6.4 and 6.5 where  $D$  is called the damage parameter,  $N_i$  is the number of cycles at the stress level  $\sigma_i$  and  $N_f$  is the number of cycles to cause fatigue failure at the that stress level.

$$\begin{aligned} D &= 0 \quad \text{at} \quad N = 0 \\ D &= 1 \quad \text{at} \quad N = N_f \end{aligned} \tag{6.4}$$

$$D = \sum_{i=1}^n \frac{N_i}{N_f} \quad \text{for} \quad 0 < N_i < N_f \tag{6.5}$$

For non-zero mean stresses, Gerber's model (Equation (6.6)) can be used. The number of cycles to failure is given by equation 6.7, where  $\sigma_a$  and  $\sigma_m$  are the amplitude and mean stresses respectively,  $\sigma_u$  is the static strength and  $\sigma_f'$  and  $b$  are experimentally determined parameters. In equation 6.6,  $\sigma_{am}$  is the equivalent stress amplitude with zero mean value which causes the same effect that  $\sigma_a$  and  $\sigma_m$ . Typical values for common metallic materials from tests at zero mean stress on un-notched axial specimens are listed in Table 6.3 [26]. Additionally, the American Bureau of Shipping (ABS) [34] and the Standard Specifications for Structural Steel for Ships [33], require that the minimum tensile properties for ordinary strength hull structural steels must be 235 MPa and 400 MPa for yielding and tensile strength respectively. These values are relatively close to those listed in Table 6.3 for the AISI 1015 normalized steel. Thus, similar values of  $\sigma_f'$  and  $b$  were assumed for a structural steel for ship hull applications.

$$\frac{\sigma_a}{\sigma_{am}} + \left( \frac{\sigma_m}{\sigma_u} \right)^2 = 1 \quad (6.6)$$

$$N_f = \frac{1}{2} \left[ \frac{\sigma_a}{\sigma_f'} \frac{1}{1 - (\sigma_m/\sigma_u)^2} \right]^{1/b} \quad (6.7)$$

**Table 6.3.** Constants for S-N curves for various ductile materials.

Material	Yield Strength $\sigma_y$ (MPa)	Ultimate Strength $\sigma_U$ (MPa)	$\sigma_f'$ (MPa)	A (MPa)	$b = B$
<i>a) Steels</i>					
AISI 1015 (normalized)	227	415	976	886	-0.14
Man-Ten (hot-rolled)	332	557	1089	1006	-0.115
RQC-100	683	758	938	897	-0.0648
AISI 4142 (Q&T, 450 HB)	1584	1757	1937	1837	-0.0762
AISI 4340 (aircraft quality)	1103	1172	1758	1643	-0.0977
<i>b) Other Metals</i>					
2024-T4 Al	303	476	900	839	-0.102
Ti-6Al-4V	1185	1233	2030	1889	-0.104

For a specific number of impacts  $n_i$ , a series of cyclic stresses with mean values  $\sigma_m$  and amplitudes  $\sigma_a$  were obtained following the methodology described in Sections 6.3 and 6.4. These stresses were used in Eq. 6.7 to calculate the required numbers of cycles to failure ( $N_f$ ) of each individual pair of data ( $\sigma_m, \sigma_a$ ). Finally, the individual damage contributions were combined using Eq. 6.5 to obtain the total

accumulated damage. This procedure was programmed in a MATLAB® code (Appendix A) which also included the extrapolation of stresses and the cycle counting. The code receives as inputs a spreadsheet file with the stress time history of a single impact event, the number of impacts of interest  $n_i$  and the threshold levels  $u_{\min}$  and  $u_{\max}$ . The values of  $n_i$ ,  $u_{\min}$  and  $u_{\max}$  are user defined. In this analysis, three different case scenarios were considered:  $u_{\max} = 150$  MPa;  $u_{\max} = 160$  MPa; and  $u_{\max} = 180$  MPa. The objective was to determine the sensitivity of the damage results to the selection of  $u_{\max}$ . The code follows the four steps shown in Figure 6.14 and produces the following outputs: the extrapolated stress time history, the Rainflow matrix of major cycles for  $n_i$  impacts, and the predicted damage for that number of impacts. Initially, the number of impacts was set in  $10^5$  and subsequently it was increased until the critical damage ( $D = 1$ ) was exceeded. As a result, the damage plots of Figure 6.15 were obtained. A linear fit equation was used to measure the linearity of the predicted results. In each case, the inverse of the slope of the fit equation was used to estimate the fatigue life (number of impacts to failure) of the location of interest. Notice that number of impacts was used in the x-axis instead of number of cycle; each impact contains several cycles and half cycles with different amplitudes and means values. Figure 6.16 compares these results with the damage predicted for extrapolated stresses based on Single Block Repetitions (without TPs modification). The effect of  $u_{\max}$  on the damage results is evident, the lower the value of  $u_{\max}$  the lower the number of impacts required for fatigue failure. The fatigue life for each case scenario was estimated and listed in Table 6.4.

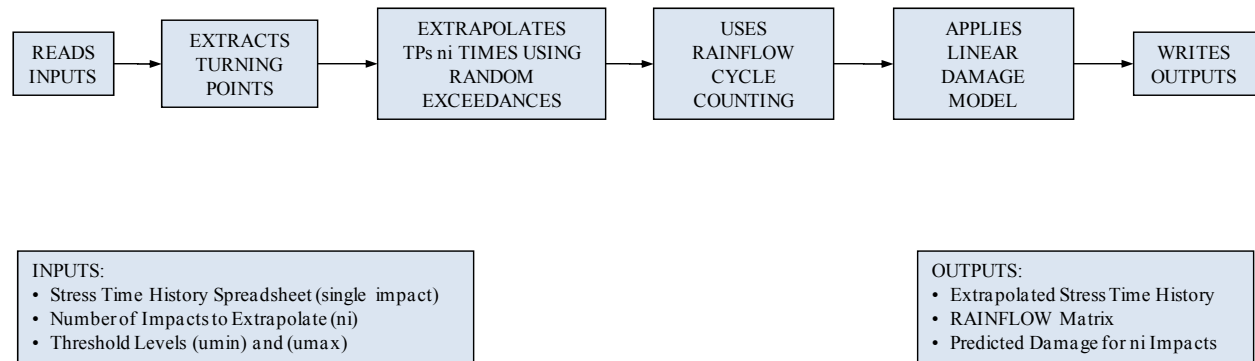


**Figure 6.14.** Damage accumulation MATLAB® code flow chart.

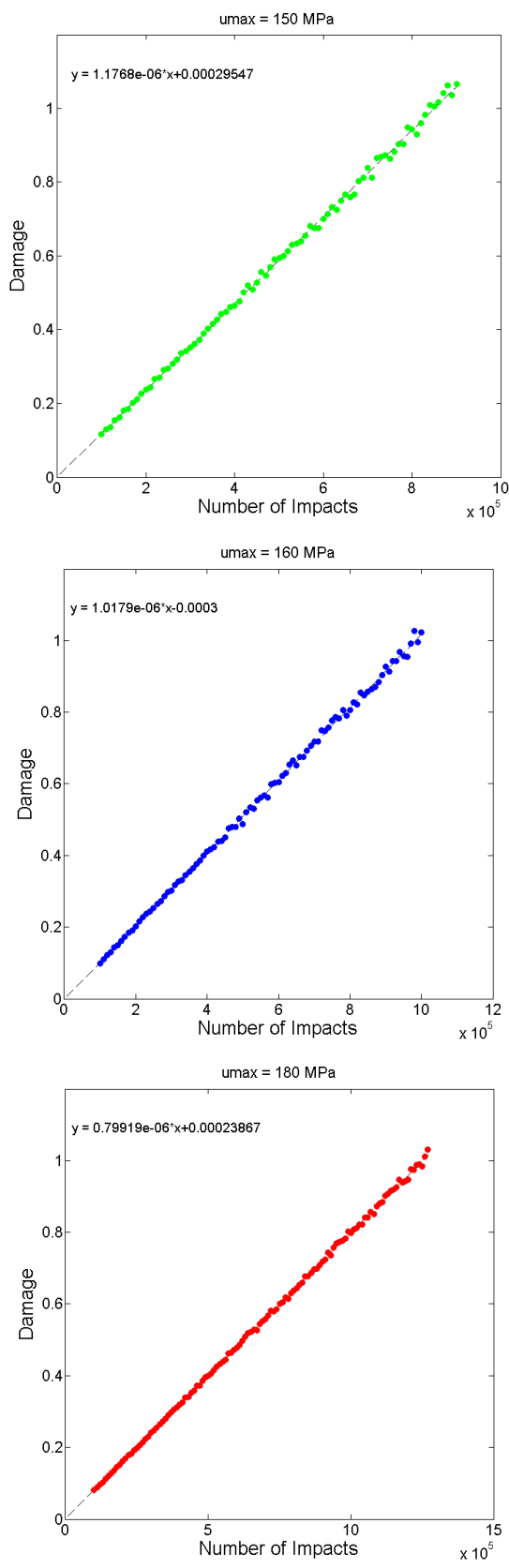


**Figure 6.15.** Damage accumulation as a function of number of impact

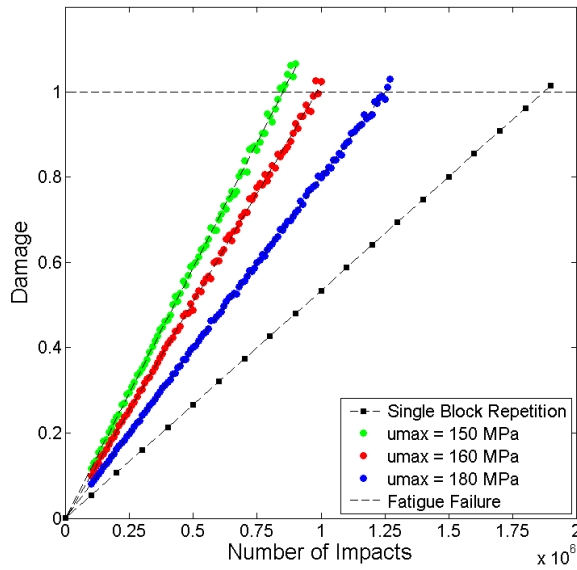


**Figure 6.16.** Damage as a function of  $u_{\max}$ .

Notice the significant reduction in fatigue life as a consequence of the extrapolation method. The fatigue life decreased from 1,871,292 impacts for single block repetition (SBR) to 849,792 impacts for POT extrapolation with threshold level  $u_{\max} = 150$  MPa. This represents the 45.41% of the original life. Even the case with  $u_{\max} = 180$  MPa reduced the fatigue life to 1,251,266 impacts (66.87%). Thus, it was demonstrated that the life predictions were highly dependent to the selected threshold levels. Therefore, it is strongly recommended to choose  $u_{\max}$  above the 80% of peak stress. However, the proposed approach is presented as a conservative method to assess fatigue life in those cases when only stresses for a limited period of time (from FE simulations or experimental data) are available.

**Table 6.4.** Fatigue life at location of interest.

Extrapolation Method	Number of Impacts
a) Single Block Repetition	1,871,292
b) POT (Threshold Level)	
$u_{\max} = 180$ MPa	1,251,266 (66.87%)
$u_{\max} = 160$ MPa	982,414 (52.50%)
$u_{\max} = 150$ MPa	849,762 (45.41%)

(Steel hull impact:  $\beta = 10^\circ$  and  $V = 5$  m/s)

### 6.5.1.1 Statistical Analysis of Damage Predictions (Linear Model)

As a result of the random generated exceedances, some degree of variance was expected in the damage predictions. In other words, the MATLAB® program described in Figure 6.14 does not produce the same exact output result for the same input data. The variance of the damage predictions is very important to determine the confidence of the results of the proposed approach. In order to evaluate this variance, the case with  $u_{\max} = 150$  MPa and 849,762 impacts was ran multiple times. This case was thought to be the worst case scenario in terms of damage variation because it produced the highest exceedances. Figure 6.17 shows the distribution of the damage predictions associated with this case. Notice that the results followed approximately a normal distribution with mean value 1.002 and standard deviation 0.015069, even though the exceedances were generated using a gamma distribution (see Figure 6.7). Also notice that the 97% of the predictions lied within the three standard deviation interval. This indicates that the damage and fatigue life predictions of the linear model are consistent and do not require further analysis. However, this will not be the case for non-linear models, as discussed in the next section.

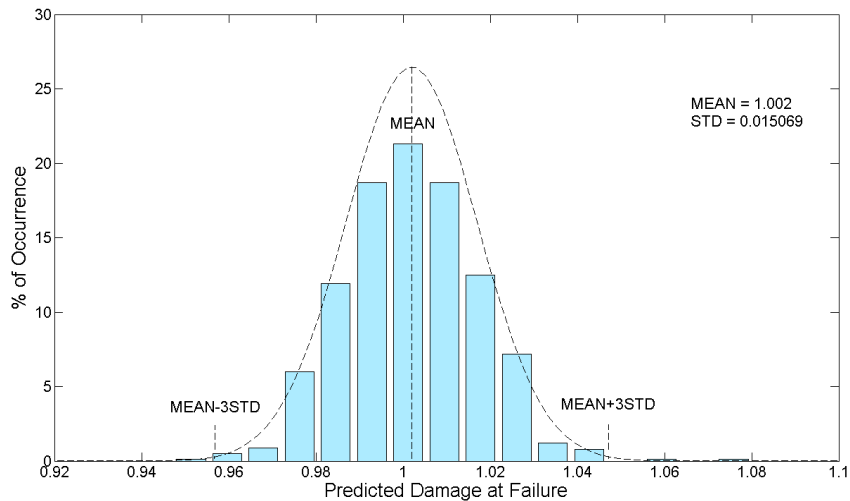


**Figure 6.17.** Damage Distribution at 849,762 impacts with  $u_{\max} = 150$  MPa.

## 6.5.2 Damage Assessment for Sandwich Composite Hulls

Fatigue damage assessment in sandwich composite structures, and other related materials, has been modeled using one of the following approaches: a) strength degradation or b) stiffness degradation. In the strength degradation approach, the residual strength of the structure is determined from a static test after fatigue loading, therefore, a series of tests are required to determine a single strength degradation curve [30, 31]. Stiffness degradation methods, though, allow measurement of effective stiffness during cyclic loading without destruction of the specimen so that a stiffness degradation curve can be obtained from a single test. Smaller numbers of specimens are required and average results can be used to characterize the fatigue strength of the structure. These advantages make the stiffness degradation approach more suitable for fatigue damage modeling and prediction; therefore it was the approach adopted in this thesis.

### 6.5.2.1 Stiffness Degradation Approach

In this approach, stiffness is defined as a modulus term which is obtained from the stress-strain curve at different number of cycles. For polymer foams structures, where core shear is the predominant mode of failure under flexural cyclic loading [24, 31], stiffness reduction is usually modeled based on the fatigue modulus concept  $G_f(n)$  (Equation 6.8). During fatigue loading, the stress-strain curve of the core material changes causing a reduction of fatigue modulus. The fatigue modulus at a specific load cycle  $n$ , is represented on the stress-strain curve by a line drawn from the origin to the resultant strain at the applied stress level (Figure 6.18). As the number of cycles increases, at an applied shear stress level  $\tau_a$ , the resultant shear strain  $\gamma(n)$  becomes larger until it reaches the failure shear strain  $\gamma_u$ . It is assumed that when failure occurs  $\gamma(N_f) = \gamma_u$  where  $N_f$  is the number of cycles to failure at stress level  $\tau_a$ . Note that knowledge of the stress-strain curve at every cycle number is not required since measurement of the fatigue modulus can be made directly from the strain or deflection time history for the given material. Additionally, it has been demonstrated [31] that the fatigue process consists of an initiation period, in which no damage is observed, followed by a period of damage progression. The number of cycles defining the initiation of fatigue damage is given by  $n_{if}$ .

$$G_f(n) = \tau_a / \gamma(n) \quad (6.8)$$

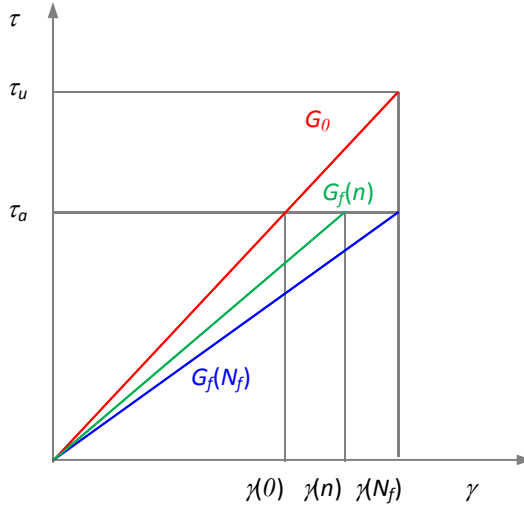


**Figure 6.18.** Fatigue modulus definition.

The fatigue modulus degradation model is given by an exponential function which describes the decrease in modulus from an initial static value  $G_0$ , (Equation 6.9), where  $A$  and  $C$  are material constants to be determined experimentally. A non-linear S-N model can be derived from Equation 6.9 in terms of the applied stress ratio  $r = \tau_a/\tau_u$  and the fatigue modulus at failure  $G_f(N_f) = \tau_a/\gamma_u$  (Equation 6.10). At failure ( $n = N_f$ ), the non-linear S-N model is given by Equation 6.11 which can be used to predict the number of cycles at failure for different applied stress levels. In order to consider the effect of non-zero mean stresses  $\tau_m$ , a similar approach to that described in Equation 6.6 for metallic structures can be assumed for sandwich composites. Thus, the stress ratio is computed by  $r = \tau_{am}/\tau_u$  where  $\tau_{am}$  is the equivalent shear stress amplitude with zero mean value which causes the same effect on life that  $\tau_a$  and  $\tau_m$  combined.

$$\begin{aligned} G_f(n) &= G_0 & n \leq n_{if} \\ G_f(n) &= G_0 - A \exp[(n - n_{if})C] & n > n_{if} \end{aligned} \quad (6.9)$$

$$\frac{G_f(N_f)}{G_0} = \frac{\tau_a/\gamma_u}{\tau_u/\gamma_u} = \frac{\tau_a}{\tau_u} = r \quad (6.10)$$

$$N_f = n_{if} + \frac{1}{C} \ln \left[ \frac{G_0}{A} (1 - r) \right] \quad (6.11)$$

Similarly, the fatigue damage coefficient  $D$  is defined by Equation 6.4. It accumulates from an initial damage state, equal to zero, at  $n_{if}$  cycles to a final failure value, equal to unity at  $N_f$ . However, different forms of the damage accumulation model can be selected depending on the degree of linearity of the degradation response. In this section, two models were investigated: *Model I*) Palmgren-Miner linear cumulative damage model based on the number of cycles; and *Model II*) a non-linear model based on changes of fatigue modulus. In both models, damage is assumed to initiate when fatigue damage is first observed ( $n = n_{if}$ ). Models I and II are expressed by Equations 6.12 and 6.13, respectively.

$$\text{Model I : } D(n) = \frac{(n - n_{if})}{(N_f - n_{if})} \quad n > n_{if} \quad (6.12)$$

$$\text{Model II : } D(n) = \frac{G_0 - G_f(n)}{G_0 - G_f(N_f)} = \frac{\exp[(n - n_{if})C]}{\exp[(N_f - n_{if})C]} \quad n > n_{if} \quad (6.13)$$

For non-linear models (*Model II*) loading sequence has a significant impact in the damage accumulation coefficient. To illustrate this effect, assume that *Model II* will be used to calculate the damage accumulation for two different stress levels  $r_1 > r_2$  applied sequentially. In addition, to simplify the analysis, also assume that fatigue damage initiates at zero cycles ( $n_{if} = 0$ ). The damage accumulation curves for  $r_1$  and  $r_2$  are shown in Figure 6.19. First, consider that  $n_2$  cycles are applied at stress level  $r_2$  causing a damage  $D_{21}$  (Figure 6.19 a). This damage is equivalent to that caused by  $n_{21}$  cycles at stress level  $r_1$ . Then  $n_1$  cycles are applied at stress level  $r_1$  which are added to  $n_{21}$  resulting in an accumulated damage  $D_1$ . In the second case (Figure 6.19 b),  $n_1$  cycles are applied at stress level  $r_1$  with a damage  $D_{12}$  equivalent to that caused by  $n_{12}$  cycles at stress level  $r_2$ . Subsequently,  $n_2$  cycles are applied at stress level  $r_2$  which are counted from  $n_{12}$  cycles. As a result of this stress loading sequence, a total accumulated damage  $D_2$ , greater than  $D_1$ , is obtained showing that a high-low loading sequence is more damaging than a low-high loading sequence. To consider the load sequence effect and to represent the worst case scenario, the stresses were sorted in descending order previous to damage calculation.

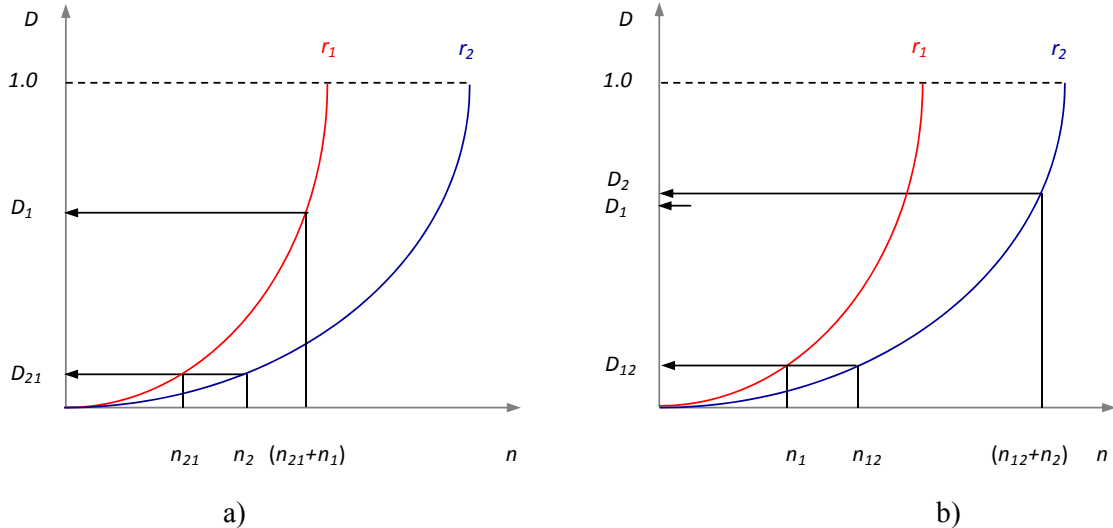


**Figure 6.19.** Damage accumulation for two stress levels: a) low/high, b) high/low.

In Figure 6.19, it was assumed that fatigue damage initiated at the zero cycles but, in practice, it has been observed that the initiation of fatigue damage is highly dependent of the stress level ( $n_{if} = n_{if}(r)$ ) [31]. At higher stress levels, the number of cycles necessary to initiate fatigue damage is much smaller than for lower stress levels. The relationship between  $r$  and  $n_{if}$  can also be determined experimentally and curve fitting can be used to develop a mathematical equation. However, the fatigue life prediction approach proposed in this thesis does not include the modeling of the number of cycles to damage initiation and therefore, it is assumed to initiate at the first cycle. This is a very conservative approach which will provide the most severe damage case scenario. In addition, experimental results [31] have demonstrated that the material constants  $A$  and  $C$  in Equations 6.9 and 6.11 are also a non-linear function of the stress ratio  $r$ . Table 6.5 summarizes the parameters and relations used in the current stiffness degradation approach for damage assessment.

**Table 6.5.** Stiffness degradation parameters for sandwich core.

Parameter	Assumed Value/Model
Static shear modulus ( $G_0$ )	9.0 MPa
Static shear strength ( $\tau_u$ )	1.9 MPa
Material parameter ( $A$ )	$0.0014\exp(8.497r)$
Material parameter ( $C$ )	$5 \times 10^{-7}\exp(13.656r)$
Number of cycles for damage initiation ( $n_i$ )	0
Number of cycles to fatigue failure ( $N_f$ )	$n_i + (1/C)\ln[G_0(1 - r)/A]$
Linear damage accumulation coeff. ( $D$ ) (Model I)	$(n - n_i)/(N_f - n_i)$
Non-linear damage accumulation coeff. ( $D$ ) (Model II)	$\exp[(n - n_i)C]/\exp[(N_f - n_i)C]$

The principal mode of failure observed in sandwich structures under cyclic flexural loads has been through thickness core shear at the locations of maximum shear stresses. In the case of the sandwich beam of Figure 6.20 the maximum shear stresses occur near the supports. Therefore, locations A and B were identified as critical in terms of fatigue life and were selected for damage assessment.

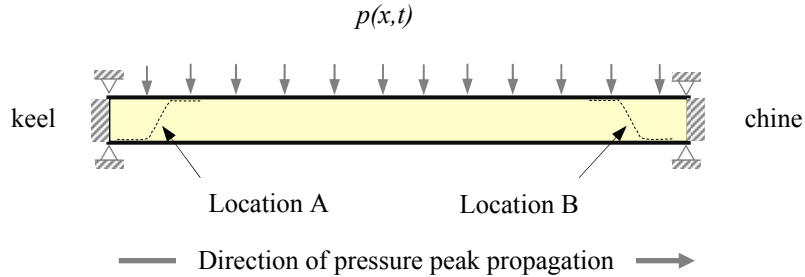


**Figure 6.20.** Fatigue failure and selected location for damage assessment.

In this case, damage was computed using a code written in MATLAB® (Appendix A) similar to that described in Figure 6.14 but with the option to select between two different damage models: a linear model (Eq. 6.12) or an exponential model (Eq.6.13). Three case scenarios ( $u_{\max}$  values) were considered for each location based on the maximum stress at that location. Results are shown in Figure 6.21 and Figure 6.22. As in Section 6.5.1, damage predictions were highly dependent on the selected threshold level  $u_{\max}$ . Notice that, in general, the linear model predicted more damage than the exponential model for small number of impacts. However, the exponential model predicted that the critical damage ( $D = 1$ ) and fatigue failure is reached much earlier when compared with the linear model. The difference in fatigue life between both models is very significant. But before discussing fatigue life predictions, it is important and necessary to take a look in more detail at the damage results plotted in Figure 6.21 and Figure 6.22. Notice that damage results, obtained using the exponential model, were very scattered in comparison with the results of the linear model. In fact, some points seemed to be inconsistent with the remaining exponential results. These “apparently” inconsistent points are called outliers and required further analysis. One alternative to deal with outliers is simply to remove or modify them from the results. But before taking any action, the cause or causes of the possible outliers should be investigated. It was found that those inconsistent damage results arose from low probability values from the exceedances distribution function (those values on the tail of the gamma distribution) but they were perfectly valid.

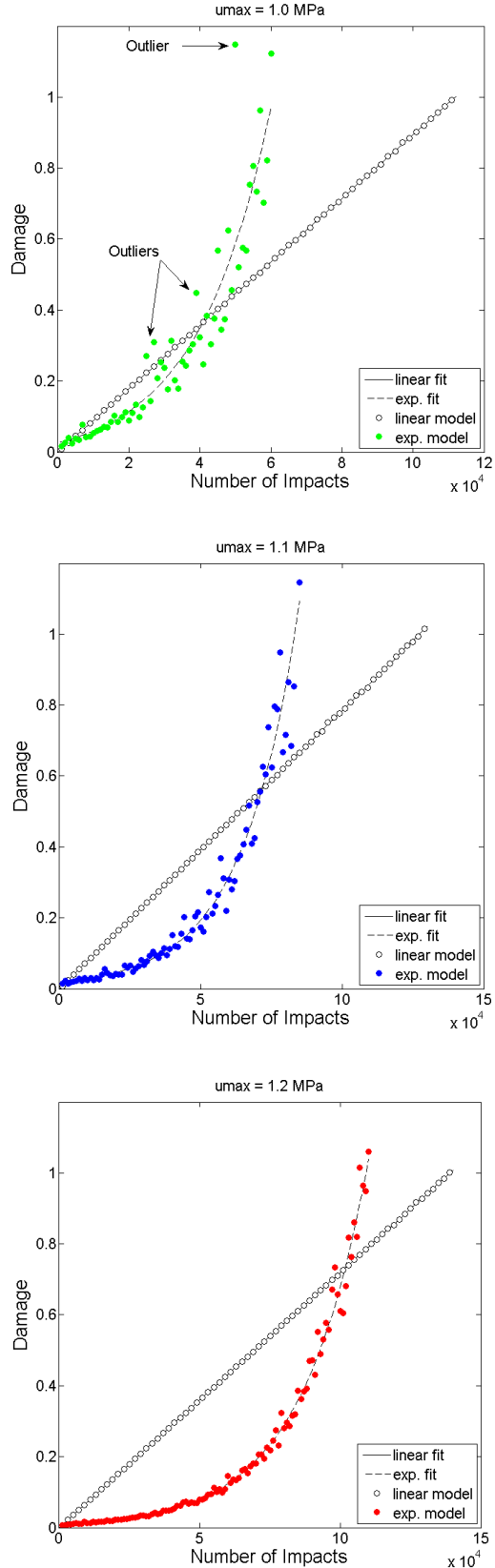


**Figure 6.21.** Damage as a function of number of impacts (Loc. A).

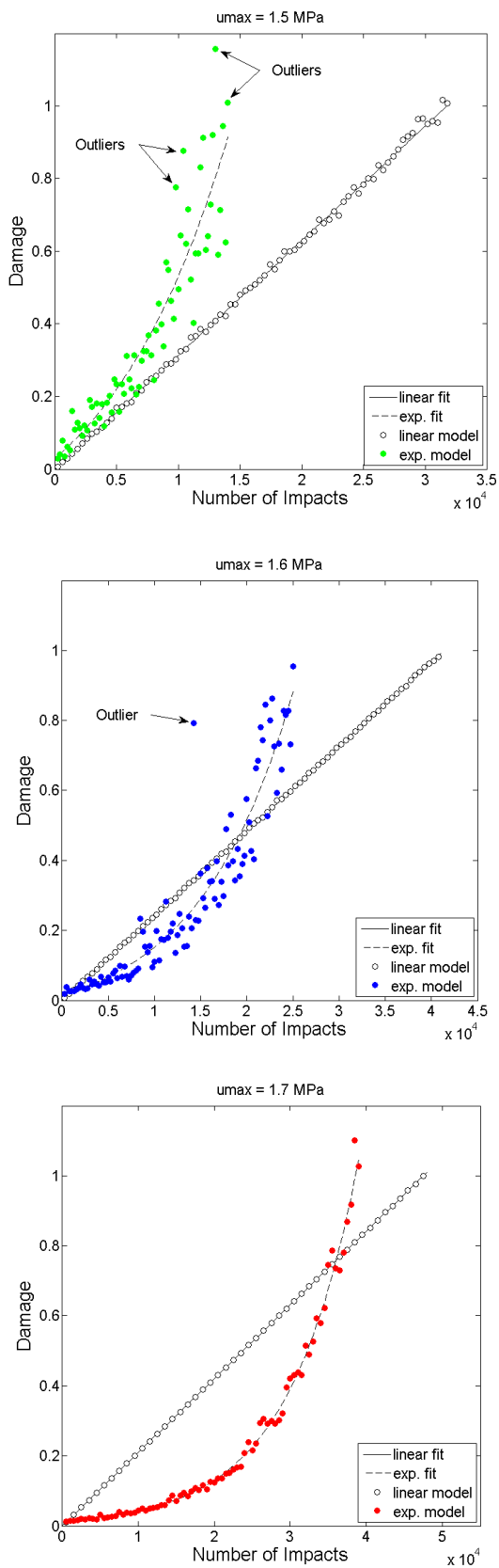


**Figure 6.22.** Damage as a function of number of impacts (Loc. B).

Additionally, it was observed that the effect of low probability exceedances on damage results was magnified by the exponential behavior of the non-linear model. Finally, it was also found that both the variance of the damage results and the occurrence of outliers were highly dependent on the selected value of  $u_{max}$ . Lower values of  $u_{max}$  produced more inconsistent results and consequently, increased the number of outliers. This was also a consequence of high exceedances values obtained from low threshold levels. In order to minimize the effect of low probability (high) exceedances on the damage results and to eliminate outliers, a simple but effective iterative approach is proposed in this thesis. This approach was based on damage mean value calculation, for a particular number of impacts, until convergence criteria were satisfied (Figure 6.23). The first convergence criterion defines the minimum number of damage points to be included in the mean calculation. The second, and more important, criterion establishes the minimum value that the damage residual must reach in order consider a converged solution. The residual was calculated as the absolute difference in damage mean value between two consecutive iterations (Eq. 6.15). Both convergence criteria are user defined inputs. For example, the damage results shown in Figure 6.24 were obtained using a minimum of ten points and a convergence value of 0.1% of the mean value for the residual (Eq. 6.14). Figure 6.24 shows four different damage convergence plots for the same event (34,000 impacts at Location B with  $u_{max} = 1.7$  MPa). Notice that, initially the predicted damage (first iteration) ranged from 0.55 to 1.15 approximately but eventually it converged to 0.64. Ultimately, this was the damage level associated with that event.

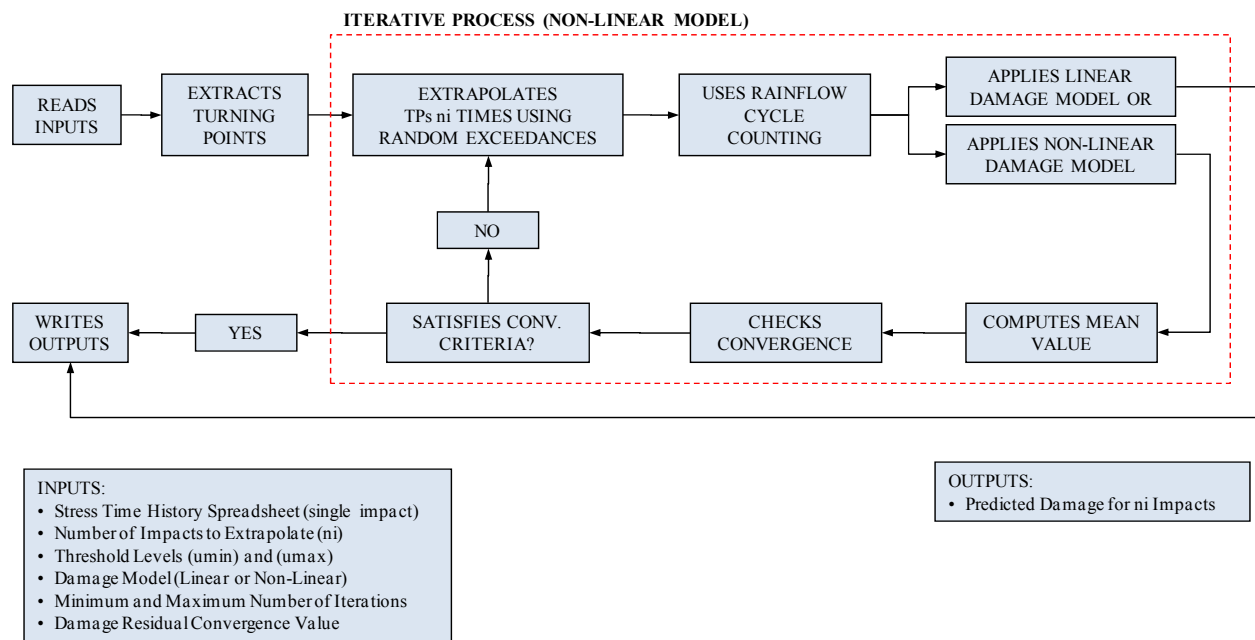


**Figure 6.23.** MATLAB<sup>®</sup> code flow chart.

$$D_{conv} = 0.001 \times D_{mean} \quad (6.14)$$

$$D_{residual} = \text{abs} \left[ D_{mean}^{(i)} - D_{mean}^{(i-1)} \right] \leq D_{conv} \quad (6.15)$$

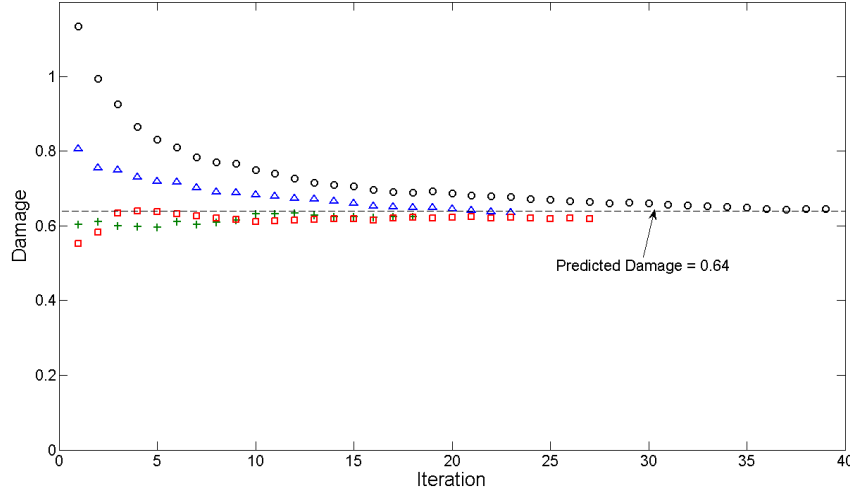


**Figure 6.24.** Damage convergence.

Figure 6.25 and Figure 6.26 show how the proposed iterative approach improved the reliability of the damage results and helped minimize, and in some cases, eliminate outliers. The effect of extrapolated stresses on linear and exponential damage predictions can be seen in Figure 6.27 and Figure 6.28 respectively, (Location A). Similarly, Figure 6.29 and Figure 6.30 for Location B. Results were compared with the case of extrapolated stresses with zero exceedances or Single Block Repetition (SBR). In the SBR case, the extrapolated stresses were obtained by simple repetition (without TPs modification) of the FE stress time history. Damage associated with this case was significantly lower than damage calculated from POT extrapolated stresses, especially for the non-linear model. Based on these damage results, fatigue life or the number of impacts to failure was predicted as a function of  $u_{max}$  (Table 6.6). In each case, fatigue life was calculated using the corresponding fit equation. The failure point was defined as the point at which the fitted curve interested the critical damage ( $D = 1$ ).

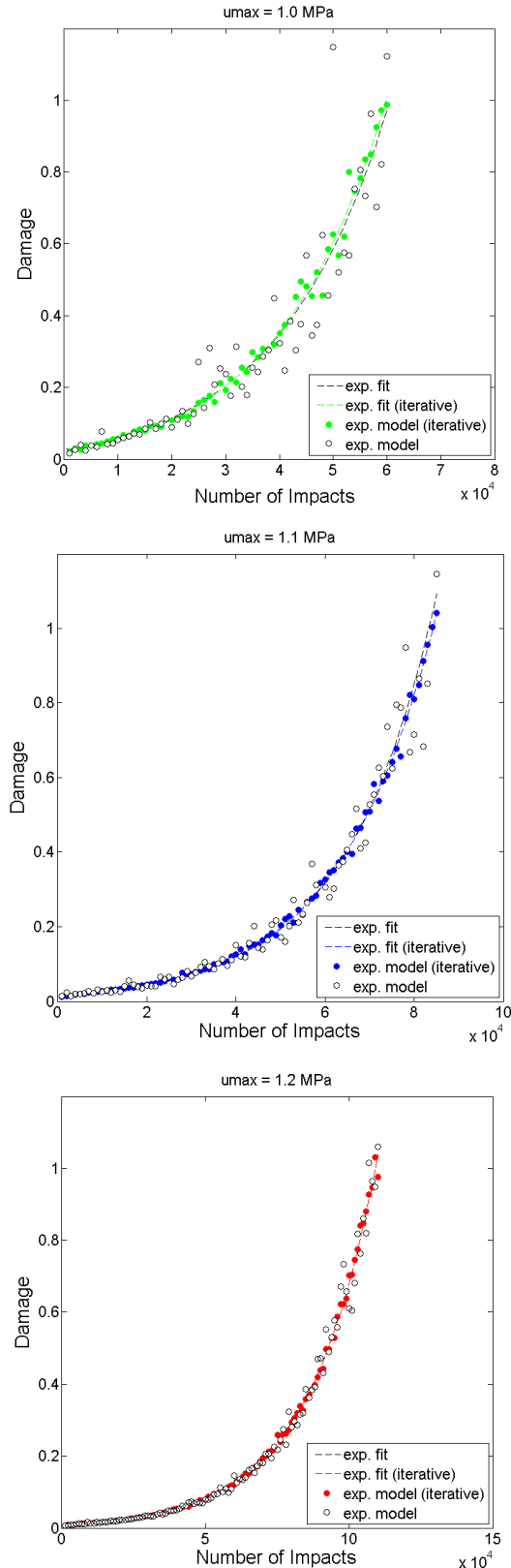


**Figure 6.25.** Damage as a function of number of impacts (Loc. A).

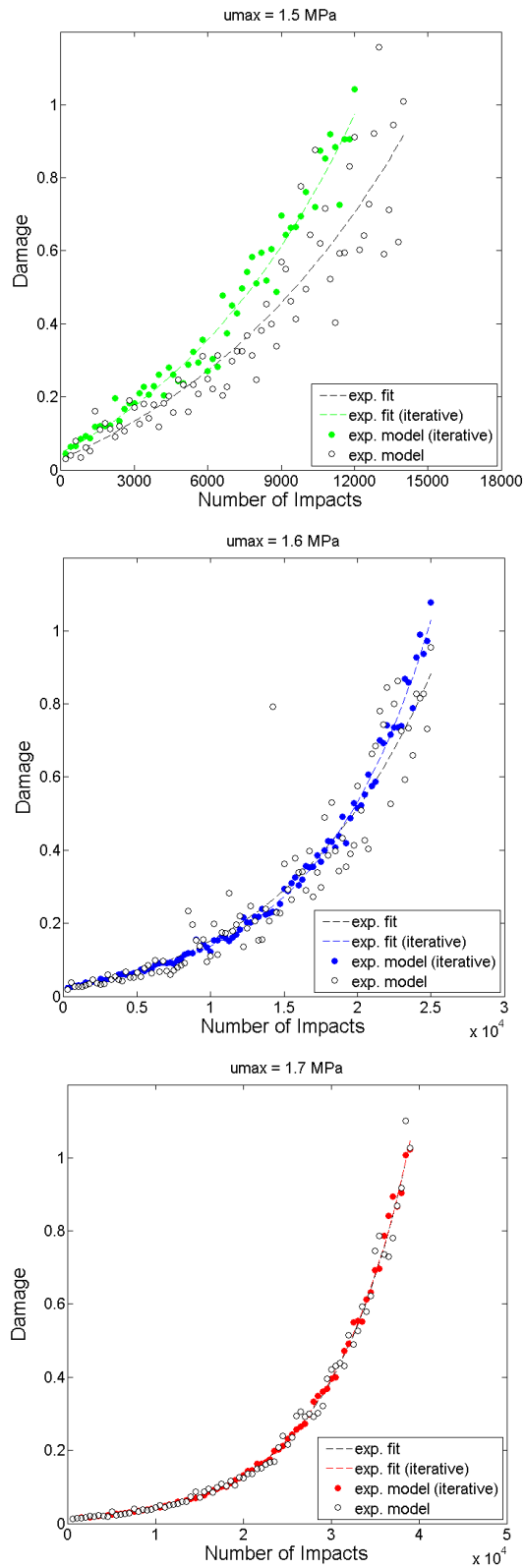


**Figure 6.26.** Damage as a function of number of impacts (Loc. B).

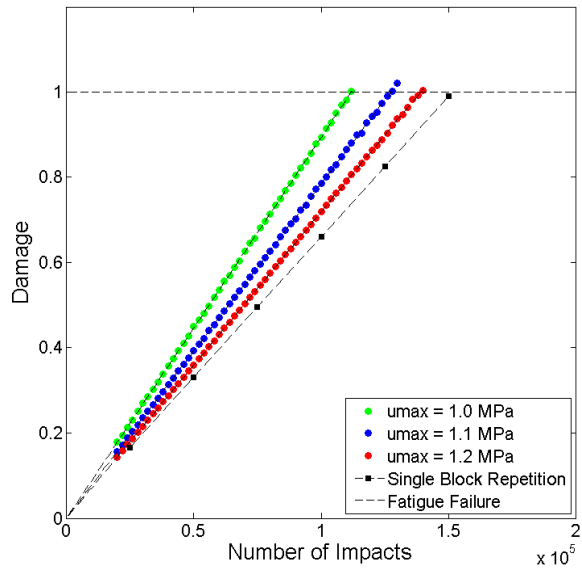


**Figure 6.27.** Linear damage predictions (Loc.A).

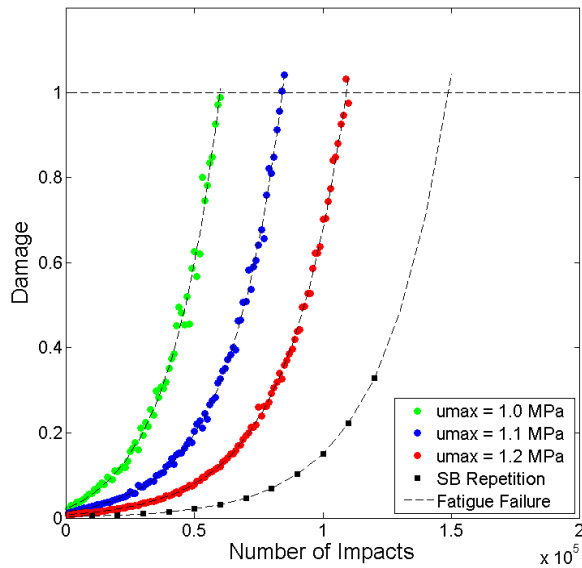


**Figure 6.28.** Non-linear damage predictions (Loc. A).

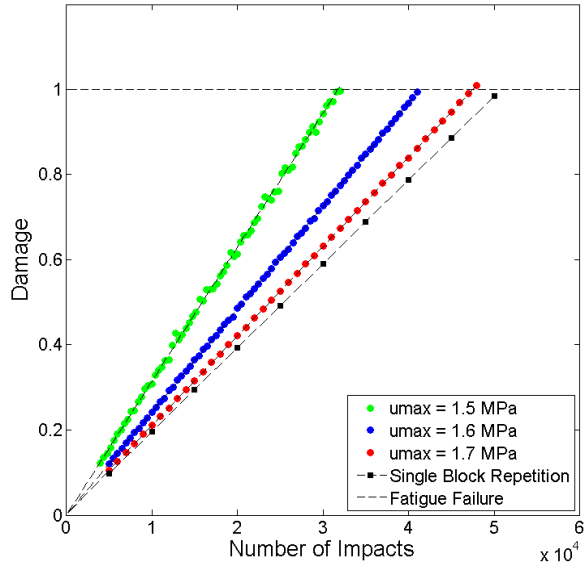


**Figure 6.29.** Linear damage predictions (Loc. B).

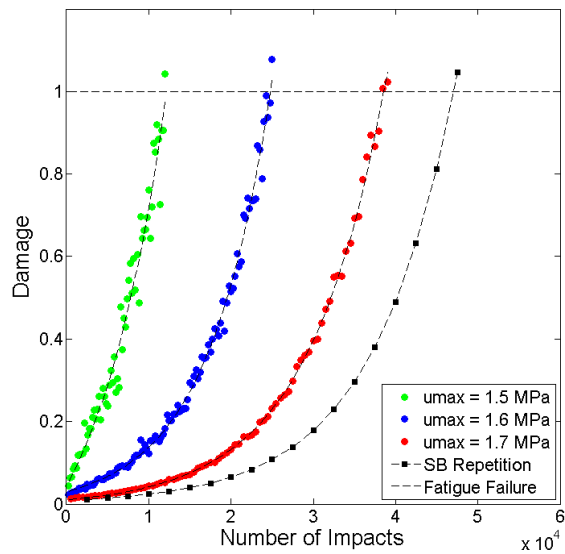


**Figure 6.30.** Non-linear damage predictions (Loc. B).

**Table 6.6.** Fatigue life at locations of interest.

Location	<b>Damage Model I</b> (Linear)	<b>Damage Model II</b> (Non-linear)
A) POT Threshold Level		
$u_{max} = 1.00 \text{ MPa}$	111,842	59,817 (53.48%)
$u_{max} = 1.10 \text{ MPa}$	127,372	84,143 (66.06%)
$u_{max} = 1.20 \text{ MPa}$	139,030	109,085 (78.46%)
Single Block Repetition	151,417	148,903 (98.33%)
B) POT Threshold Level		
$u_{max} = 1.50 \text{ MPa}$	31,731	12,487 (39.5%)
$u_{max} = 1.60 \text{ MPa}$	41,301	24,776 (59.98%)
$u_{max} = 1.70 \text{ MPa}$	47,529	38,562 (81.13%)
Single Block Repetition	50,738	47,069 (92.76%)

(Sandwich hull impact:  $\beta = 10^\circ$  and  $V = 5 \text{ m/s}$ )

For SBR extrapolated stresses, both the linear model and the non-linear model predicted a similar fatigue life, 151,417 and 148,903 impacts at Location A and 50,738 and 47,069 impacts at Location B. For POT extrapolated stresses, on the other hand, the non-linear model predicted a significantly lower fatigue life than the linear model. The worst case scenario was at Location B with  $u_{max} = 1.50 \text{ MPa}$ . The linear model predicted that the fatigue life at that location is 31,731 impacts while the exponential model predicted 12,487 impacts, which represents more than 60% reduction in fatigue life. Clearly, the difference in fatigue life results between both models reduced as  $u_{max}$  approached to the maximum stress at that location, in which case there are no exceedances and the extrapolated stresses coincide with those obtained using the SBR approach.

## CHAPTER 7. CONCLUSIONS

The work outlined in this thesis presents a computational methodology for the fatigue life assessment of sandwich composite hulls subject to repeated slamming loads. The approach included the following objectives and conclusions:

1) The investigation of the hydrodynamic pressure and structural deformation during the impact: Two theoretical models were selected from the literature and used for validation purposes. The Zhao and Faltinsen model [6] was used to predict the pressure distribution in the contact region of rigid hulls. The pressure distribution was characterized by a concentrated peak which propagated from the keel to the chine following the contact point. The magnitude of the pressure showed to be related to the deadrise angle and impact velocity. The time required for the pressure peak to reach the chine of the hull (impact stage) was used to determine the simulation time of FE models. Additionally, the width of the pressure peak showed to expand during the impact which indicated that an expanding mesh was required in order to capture the pressure peak with sufficient accuracy. The study of slamming on metallic hulls was based on the hydroelastic model developed by Korobkin [8, 9]. This model combines an elastic structural formulation with Wagner's theory to predict hull deflections. The method was programmed using MATLAB and the resulting first order ODE system was solved using the Runge-Kutta algorithm. Results demonstrated that hull deflections can be successfully approximated using only the first three dry mode shapes. Maximum deflections occurred between the end of the impact stage and the beginning of the penetration stage.

2) The development and validation of FE models to obtain stress time histories for a single impact event: the modeling included the multimaterial ALE formulation and the penalty based contact algorithm. The results of the analysis showed to be highly dependent on the mesh density and not on the contact stiffness and damping. The pre-knowledge of the expanding pressure peak was used to determine the FE mesh within the fluid domain. As a result, the fluid domain was divided into two domains: 1) an interior domain located near the keel, where high mesh density was required, and 2) an exterior domain located beyond the influence of the impact. The interior domain was meshed with a uniform element size while within the exterior domain an expanding mesh toward the model boundaries was used. High mesh density was required to capture the pressure peak in rigid hull impacts. Later, it was demonstrated that hull deflections and stresses can also be accurately predicted using coarser meshes because the effect of the pressure peak on the dynamic response of the hull structure was not very important. This notably reduced the computational cost of the simulations. FE models showed to under-predict impact pressure and

structural deformations when compared with analytical results. However, FE results showed better correlation with experimental data than analytical results. During the penetration stage of elastic hulls, a damped oscillatory response was observed and cyclic stresses were obtained. Based on these stresses, critical locations were selected for lifing assessment. The predominant mode of failure of the hull's material under flexural cyclic loading was also considered for the selection of critical locations, maximum bending stresses for metallic hulls and maximum core shear for sandwich composite hulls. Then, Peak Over Threshold (POT) analysis was conducted to extrapolate stresses time histories. Exceedances were numerically predicted by assuming that they follow a gamma distribution.

3) The implementation of existing damage accumulation models to predict fatigue life of metallic and sandwich composite hulls: the Rainflow cycle counting method was used to reduce the complex slamming loading to a series of simple cyclic loadings. For each load level, the degree of cumulative damage induced in the structure was calculated from the S-N curves and the individual contributions were combined using a damage accumulation model. For metallic hulls, linear Miner's rule was used. Damage results demonstrated to be highly dependent on the selection of the threshold levels during the extrapolation analysis. Using the proposed approach, the fatigue life at the critical location of a steel hull with deadrise angle  $\beta = 10^\circ$  and impact velocity  $V = 5$  m/s was estimated between 850,000 and 1,250,000 impacts. Unfortunately, up to this point of this investigation, there was no experimental data available to verify these results. For sandwich composite hulls two damage models were applied: Miner's rule, based on number of cycles, and non-linear stiffness degradation approach, based on reduction of fatigue (shear) modulus. Non-linear damage models are dependent on loading sequence; a high-low loading sequence is more damaging than a low-high loading sequence. To consider the load sequence effect, the stresses were sorted in descending order previous to damage calculation. Miner's rule showed to be very conservative for small number of impacts, but eventually, the stiffness degradation model predicted a significantly lower fatigue life. In this case, damage results were also highly dependent on the selection of the threshold levels. As a consequence of low probability high stresses, non-linear damage predictions were very scattered and, in some cases, apparently inconsistent with the set of results. In order to eliminate those outliers and improve the reliability of our damage results a simple but effective iterative approach was proposed and implemented. This approach was based on damage mean value calculation for a particular number of impacts. As a result, fatigue life at selected critical locations of the sandwich hull was estimated. The limiting location was found to occur within the sandwich core near the chine with a fatigue life between 12,500 and 38,500 impacts.

4) The validation of the proposed fatigue life prediction approach using comparative results from experimental tests: Ultimately, fatigue life predictions presented in this thesis were intended to be validated with previous results published in [24]. However, the author concluded that a comparative analysis of results was not possible due to the following reasons: a) The experimental setup of the slamming tests was incompatible with the boundary conditions assumed in the FE modeling of the problem. For instance, the test specimens were simply supported in the impact direction (direction of pressure peak propagation) and not in the perpendicular direction. A very different modeling approach was followed in this thesis, boundary conditions were always assumed at the keel and at the chine of the hull. In this way, the problem could be modeled using two dimensional symmetric models. This has been the usual approach in the numerical modeling of impacts of elastic hulls [8, 9, 10, and 17]. To reproduce the same impact conditions as in [24], more complex three dimensional models are required, which are beyond the scope of this thesis. b) Some material properties required for the proposed life prediction model were not provided in [24], in particular for the foam core. Therefore, they were assumed based on data published in the literature for similar materials. These properties included the static shear modulus, static shear strength, and material constants ( $A$  and  $C$ ), among others. Consequently, fatigue life results reported in this thesis have not been experimentally validated.

## CHAPTER 8. RECOMMENDATIONS

### 8.1 SCOPE AND LIMITATIONS OF THE APPROACH

Fatigue life predictions obtained as a result of the proposed approach are primarily intended to be used for design of structural components on ship hulls subject to repeated loading. Additionally, fatigue life results may be used for other applications, such as maintenance planning and damage inspection scheduling of possible critical locations. Thus, fatigue initialization can be detected at early stages and parts can be repaired or replaced before catastrophic failure. However, the methodology presented in this thesis is limited to those cases in which the simplified models and assumptions apply. The success of the approach also depends on the engineering judgment and experience of the user. Therefore, the resulting fatigue life may differ from actual values and some variations of the method may be required. To address these limitations, the following topics are recommended as additional work.

### 8.2 PROPOSED FUTURE WORK

The author strongly recommends that further investigation related to the fatigue life assessment presented in this thesis should include:

- Perform 3D FE analysis using actual ship hull geometries.
- Extend FE simulations to include several impact events and different conditions (deadrise angle and impact velocity).
- Develop regression models based on FE results to predict high stresses at critical locations for non-simulated impact conditions.
- Improve high stress exceedances models using experimental data measured on actual structural components under similar sea loading conditions to obtain more representative stress time histories.
- Include in the proposed approach other modes of failure such as core tearing and local buckling to identify additional critical locations in sandwich composite hulls for life assessment.
- Validate the methodology presented in this thesis using experimental fatigue life results.
- Incorporate a crack growth and propagation model to estimate fracture life on sandwich composites hulls.

## REFERENCES

- [1] Von Karman, T. (1929) The impact of seaplane floats during landing. NACA TN 321; National Advisory Committee for Aeronautics, Washington, USA.
- [2] Wagner, H. (1932) Über stoß- und gleitvogänge an der oberfläche von flüssigkeiten. Zeitschrift für Angewandte Mathematik und Mechanik, 12, 4; 193-215.
- [3] Dobrovolskaya, Z. N. (1969) On some problems of similarity flow of fluid with a free surface. Journal of Fluid Mechanics; 36, 805-829.
- [4] Watanabe, I. (1986) Analytical expression of hydrodynamic impact pressure by matched asymptotic expansion technique. West Japan Society of Naval Architecture; 71, 77.
- [5] Cointe, R. (1989) Two-dimensional water solid impact. Journal of Offshore Mechanic Arctic Engineering; 111:109-14.
- [6] Zhao, R, Faltinsen, O. (1993) Water entry of two-dimensional bodies. Journal of Fluid Mechanics; 246:593-612.
- [7] Kvalsvold, J., Faltinsen, O. M. (1995) Hydroelastic modeling of wet deck slamming on multihull vessels. Journal of Ship Research; 39, 3, 225-239.
- [8] Korobkin, A.A. (1998) Wave impact on the center of an Euler beam. Journal of Applied Mechanics and Technical Physics; 39, 770-781.
- [9] Korobkin, A. A. (2000) Elastic wedge impact. Lecture 1, Lecture Notes, INSEAN - Marine Technology Research Institute.
- [10] Qin, Z., Batra, R. C. (2009) Local slamming impact of sandwich composite hulls. International Journal of Solids and Structures; 46, 2011-2035.
- [11] Bereznitski, A., Boon, B., Postnov, V. (2001) Hydroelastic formulation in order to achieve more accurate prediction of hydrodynamic loads. Eleventh International Offshore and Polar Engineering Conference, Stavanger, Norway.
- [12] Korobkin, A. A., Gueret R., Malenica S. (2006) Hydroelastic coupling of beam finite element model with Wagner theory of water impact. Journal of Fluids and Structures; 22, 493-504.
- [13] Bereznitski, A. (2001) Slamming: The role of hydroelasticity. Delft University of Technology, Faculty of Design, Enginnering and Production, Ship Structures Laboratory, Delft, The Netherlands. International Shipbuilding Progress; 48, 4, 333-351.
- [14] Aquelet, N., Souli, M., Olovsson, L. (2005) Euler-Lagrange coupling with damping effects: Application to slamming problems. Computer Methods in Applied Mechanics and Engineering.
- [15] Souli, M., Ouahsine, A., Lewin, L. (2000) ALE formulation for fluid-structure interaction problems. Computer Methods in Applied Mechanics and Engineering; 190, 659-675.

- [16] Souli, M., Benson, D. (2010) Arbitrary Lagrangian-Eulerian and fluid-structure interaction, Numerical simulations. Editorial WILEY-ISTE.
- [17] Stenius, I., Rosen A., Kuttenkeuler J. (2006) Explicit FE modeling of fluid-structure interaction in hull-water impacts. International Shipbuilding Progress; 53, 103-121.
- [18] LS-DYNA, Theory manual 2007; Livermore Software Technology Corporation; Version 971.
- [19] LS-DYNA, Keyword user's manual 2007; Livermore Software Technology Corporation; Version 971.
- [20] Tutt, B., Taylor, A. The use of LS-DYNA to simulate the water landing characteristic of space vehicles. 8<sup>th</sup> International LS-DYNA Users Conference.
- [21] Anghileri, M., Spizzica, A. (1995) Experimental validation of finite element models for water impacts. Proceedings of the Second International Crash Users Seminar, Cranfield, UK.
- [22] Downs-Honey, R., Edinger, S., Battley, M. (2006) Slam testing of sandwich panels. SAMPE Journal, 42,4.
- [23] Breder, J. (2005) Experimental testing of slamming pressure on a rigid marine panel. Master thesis, Naval Systems KTH Aeronautical and Vehicle Enginering, Stockholm, Sweden.
- [24] Charca, S. (2009) Experimental study of wave slamming of sandwich composite panels. Doctoral thesis; Civil Engineering and Surveying Department, University of Puerto Rico at Mayagüez, PR.
- [25] Thomas, G., Davis, M., Holloway, D., Roberts, T. (2005) The influence of slamming and whipping on the fatigue life of a high-speed catamaran. International Conference on Fast Sea Transportation FAST 2005, St. Petersburg, Russia.
- [26] Dowling, N. E. (1999) Mechanical behavior of materials, Prentice Hall.
- [27] American Society for Testing Materials, E1049-85 (2005) Standard practices for cycle counting in fatigue analysis. ASTM International.
- [28] ANSYS Fatigue Module. 2012 ANSYS Inc.
- [29] Murthy P. L. N., Mital S. K., Gyekenyesi J. Z. NASALife – Component fatigue and creep life prediction program and illustrative examples.
- [30] Sharma, N., Gibson, R., Ayorinde, E. (2006) Fatigue of foam and honeycomb core composite sandwich structures: A tutorial. Journal of Sandwich Structures and Materials; 8, 263-319.
- [31] Clark, S. D., Shenoi, R. A., Allen, H. G. (1999) Modeling the fatigue behavior of sandwich beams under monotonic, 2-step and block-loading regimes. Composite Science and Technology; 59, 471-486.
- [32] Johannesson, P. (2006) Extrapolation of load histories and spectra, Fatigue and Fracture of Engineering Materials and Structures; 29, 3, 201-207.

- [33] American Society for Testing Materials (2008), A 131/A 131M-08 Standard specification for structural steel for ships. ASTM International.
- [34] American Bureau of Shipping (ABS). (2012) Rules for building and classing steel vessels. [www.eagle.org](http://www.eagle.org).
- [35] Nieslony, A. (2009) Rainflow for MATLAB, Version date: 12.11.2009. Department of Mechanics and Machine Design, Opole University of Technology, Opole, Poland.
- [36] MATLAB® Version R2007a, The Language of Technical Computing. The Mathworks Inc.
- [37] Das, K., Batra, R. (2011) Local Water Slamming Impact on Sandwich Composite Hulls. *Journal of Fluid and Structures*; 27, 523-551.
- [38] Burman M., Rosén A., Zenkert D. (2010) Spectrum Slam Fatigue Loading of Sandwich Materials for Marine Structures. 9<sup>th</sup> International Conference on Sandwich Structures, ICSS9, CalTech, Pasadena, USA.
- [39] Abrate, S. (2011) Dynamic Response of Composite Sandwich Panels during Hull Slamming. 9<sup>th</sup> Symposium on High Speed marine Vehicles (HSMV), Naples, Italy.
- [40] Stenius, I., Rosen, A., Kuttenkeuler, J. (2011) Hydroelastic Interaction in Panel-Water Impacts of High-Speed Craft. *Journal of Ocean Engineering*; 38, 2-3, 371-381.

## APPENDIX A: MATLAB CODES

```
% ----- Program FatigueLifev2.m -----
%
% Calculates fatigue life of a steel structure.
%
%
% Andres Cecchini
% Civil Engineering Department - Mayaguez. University of Puerto Rico
%
clc; clear all; format short g; close all;

% ----- Results from LS-DYNA %

disp(' ---> Initializing ...')

path = 'C:\Andres\UPRM\Thesis\Matlab Programs\Fatigue Analysis\';

filename = 'stresses';

[NUM,TXT] = xlsread([path filename]);

disp(' ---> Reading input data ...')

[m n] = size(NUM);

t = NUM(:,1);                                % time vector: ms
tf = t(length(t));                           % final time: ms
dt = t(2)-t(1);

ssi = NUM(:,3)*1e3;                           % single impact stresses MPa

% ----- Impact Deadrise Angle and Impact Velocity %
V = 5;                                         % impact velocity: m/s
be = 10;                                        % wedge deadrise: degrees
msr = 5;                                         % minimum stress range to count: MPa

% ----- Number of Impacts %

num_imp = 10000;
Bf_imp = 1;

ni = num_imp;
Bf = Bf_imp;

% ----- Threshold Levels %

smax = 150;
smin = 20;

% ----- (Multiple Impacts) %

disp(' ---> Extracting turning points ...')

ssi = ssi + 1e-6;
tmi = t(1):dt:ni*dt+(ni-1)*dt;
smi = repmat(ssi,ni,1);
```

```

[tp tpt] = sig2ext(smi,dt);
ntp = tp.*logical([1;abs(diff(tp)) >= msr]);
ind = find(ntp ~= 0);

ntp = ntp(ind);
ntpt = tpt(ind);

% ----- (Extrapolation of Turning Points) -----
disp(' ---> Extrapolating stresses for defined number of impacts ...')

zmax = ntp - smax;
zmin = ntp - smin;

logimax = logical(zmax > 0);
logimin = logical(zmin < 0);

zmax = zmax.*logimax;
zmin = zmin.*logimin;

indmax = find(zmax);
indmin = find(zmin);

indmaxe = isempty(indmax);
indmine = isempty(indmin);

if (indmaxe == 0);
mean_vall1 = zmax(indmax(1));
else
indmax = 1;
mean_vall1 = 0;
end

if (indmine == 0);
mean_val2 = zmin(indmin(1));
else
indmin = 1;
mean_val2 = 0;
end

mmax = mean(zmax(indmax))*logimax;
mmin = mean(zmin(indmin))*logimin;

% ----- Gamma function parameters -----
k = 9;
theta = 0.12;

entp1 = mmax.*random('gam',k*logimax,theta*logimax);
entp2 = -mmin.*random('gam',k*logimin,theta*logimin);

entp = ntp;

if (indmaxe == 0);
entp(indmax) = smax;
else
end
if (indmine == 0);
entp(indmin) = smin;
else
end

entp = entp + entp1 - entp2;

```

```

entp = repmat(entp,Bf,1);
ntp = repmat(ntp,Bf,1);
ntpt_c = ntpt;

if (Bf == 1)
else
for kk = 2:Bf;
ntpt_a = ntpt+ntpt_c(end);
ntpt_c = cat(1,ntpt_c,ntpt_a);
end
end

% ----- (Cycle Counting of Turning Points) -----
disp(' ---> Applying Rainflow cycle counting ...')

% entpm = sig2ext(entp);
% rf = rainflow(entp);

sa = rf(1,:); % stress amplitudes
sm = rf(2,:); % stress means
Nc = rf(3,:); % number of cycles or half cycles

% ----- Fatigue Life Calculation -----
% (Material: Steel AISI 1015 normalized)
%
su = 415; % ultimate strength: MPa
sf = 976;
b = -0.14;

sam = sa./(1-(sm/su).^2); % Gerber's equation

Nf = 0.5*((1/sf)*(sam)).^(1/b); % number of cycles to
% failure using Gerber's
% equation

cNf = isreal(Nf);

[Dt_sort Dt_ind] = sort(Nc./Nf,2,'descend');

sa_sort = sa(Dt_ind);
sm_sort = sm(Dt_ind);
Nc_sort = Nc(Dt_ind);

Dt_sort_ind = find(Dt_sort > 1e-7);

sa_rfa = sa_sort(Dt_sort_ind);
sm_rfa = sm_sort(Dt_sort_ind);
Nc_rfa = Nc_sort(Dt_sort_ind);

clear rfa;

rfa(1,:) = sa_rfa;
rfa(2,:) = sm_rfa;
rfa(3,:) = Nc_rfa;

disp(' ---> Computing total damage accumulation ...')

if (cNf == 1) % damage accumulation
Dt = sum(Nc./Nf);
else
Dt = 0;
end
disp(' ---> Analysis completed ...')

```

```

disp(' ')
disp('Total Accumulated Damage for # Number of Impacts')
disp('-----')
disp(' ')
disp(['Number of impacts = ' num2str(ni*Bf)])
disp(['Predicted damage accumulation = ' num2str(Dt)])
disp(['Critical damage (Failure) = 1.0'])
disp(' ')

% ----- Plot -----
%
figure(1);
p3 = plot ( ntpt_c, entp, 'b-', ...
            ntpt_c, smin*ones(length(ntpt_c),1), 'k--', ...
            ntpt_c, smax*ones(length(ntpt_c),1), 'k--');
set (p3, 'Linewidth', 1.0, 'Markersize', 6 , 'MarkerFaceColor', 'w' );
xlabel('Time (ms)');
ylabel('Turning Points (MPa)');
title(['Hull stresses - Repeated impacts - V = ' num2str(V) ...
        ' m/s - \beta = ' num2str(be) '^o']);
legend(['Extrapolated Time History'], ['Threshold Levels'], ...
        'Location','SouthEast');
axis([0 ntpt_c(end) -100 400])
set(gca,'PlotBoxAspectRatio',[5 2 1])

figure(2);
rfmatrix(rfa,20,20);
set(gca,'PlotBoxAspectRatio',[1 1 1])

% ----- End -----
%

```

```

% ----- Program FatigueLifev3.m -----
%
% Calculates fatigue life of foam core sandwich composites
%
%
% -----
% Andres Cecchini
% Civil Engineering Department - Mayaguez. University of Puerto Rico %
% -----



clc; clear all; format short g; close all;

% ----- Results from LS-DYNA -----
path = 'C:\Andres\UPRM\Thesis\Matlab Programs\Fatigue Analysis\';

filename = 'stresses_core';

[NUM,TXT] = xlsread([path filename]);

[m n] = size(NUM);

t = NUM(:,1);                                % time vector: ms
tf = t(length(t));                          % final time: ms
dt = t(2)-t(1);

ssi = NUM(:,3)*1e3;                           % single impact stresses MPa

disp(' ')
disp('           <predicted>    <convergence>      ')'
disp('           <damage>       <value>          <residual> ')'
disp(' -----')'
disp(' Starting damage iteration ...        ')'

% ----- Impact Deadrise Angle and Impact Velocity -----
V = 5;                                         % impact velocity: m/s
be = 10;                                        % wedge deadrise: degrees
msr = 0.020;                                     % minimum stress range to count: MPa

min_iter = 1;                                    % minimum number of iterations

% ----- Number of Impacts -----
num_imp = 34000;

counter = 1;

for count = 1:1e3;

ni = num_imp;
Bf = 1;

% ----- Threshold Levels -----
smax = 1.7;
smin = 0.10;

% ----- (Multiple Impacts) -----
clear tmi smi tp tpt ntp ind ntp ntpt

ssi = ssi + 1e-6;

```

```

tmi = t(1):dt:ni*tf+(ni-1)*dt;
smi = repmat(ssi,ni,1);

[tp tpt] = sig2ext(smi,dt);

ntp = tp.*logical([1;abs(diff(tp)) >= msr]);
ind = find(ntp ~= 0);

ntp = ntp(ind);
ntpt = tpt(ind);

ntpt = repmat(ntpt,Bf,1);

% ----- (Extrapolation of Turning Points) -----
clear zmax zim logimax logimin indmax indmin indmaxe indmine mmax mmin
clear ent entp1 entp2

zmax = ntp - smax;
zmin = ntp - smin;
logimax = logical(zmax > 0);
logimin = logical(zmin < 0);

zmax = zmax.*logimax;
zmin = zmin.*logimin;
indmax = find(zmax);
indmin = find(zmin);
indmaxe = isempty(indmax);
indmine = isempty(indmin);

if (indmaxe == 0);
mean_val1 = zmax(indmax(1));
else
indmax = 1;
mean_val1 = 0;
end

if (indmine == 0);
mean_val2 = zmin(indmin(1));
else
indmin = 1;
mean_val2 = 0;
end

mmax = mean(zmax(indmax))*logimax;
mmin = mean(zmin(indmin))*logimin;

entp = ntp;

if (indmaxe == 0);
entp(indmax) = smax;
else
end
if (indmine == 0);
entp(indmin) = smin;
else
end

% ----- Gamma function parameters -----
k = 9;
theta = 0.12;

```

```

entp1 = mmax.*random('gam',k*logimax,theta*logimax);
entp2 = -mmin.*random('gam',k*logimin,theta*logimin);

entp = entp + entp1 - entp2;

entp = repmat(entp,Bf,1);
ntp = repmat(ntp,Bf,1);

ntpt_c = ntpt;

if ( Bf == 1)
else
for kk = 2:Bf;
ntpt_a = ntpt+ntpt_c(end);
ntpt_c = cat(1,ntpt_c,ntpt_a);
end
end

% ----- (Cycle Counting of Turnin Points) -----
clear rf sa sm Nc

rf = rainflow(entp);

sa = rf(1,:)'%; stress amplitudes
sm = rf(2,:)'%; stress means
Nc = rf(3,:)'%; number of cycles or half cycles

% ----- Fatigue Life Calculation -----
clear sam r r_ind ra nra Nca nif A B C Nf

su = 2.30; % shear strength: MPa
G0 = 9.00; % shear modulus: MPa

sam = sa./(1-(sm/su).^2); % Gerber's equation

r = sam/su; % stress ratio

[r r_ind] = sort(r,1,'descend');

Nc = Nc(r_ind);

[ra nra] = count_unique(r);
cnra = cumsum(nra);

Nca = zeros(length(ra),1);
cindex = 1;
for index = 1:length(ra);
Nca(index,1) = sum(Nc(cindex:cnra(index)));
cindex = cnra(index)+1;
end

r = ra;
Nc = Nca;

nif = zeros(length(r),1); % cycles to damage initiation

% ----- Material Constants -----
A = 0.0014*exp(8.497*r); % parameter A
B = G0./A; % parameter B
C = (5e-7)*exp(13.656*r); % parameter C

```

```
% ----- Damage Model ----- %

Nf = nif + (1./C).*log(B.*(1-r)); % number of cycles to failure

dam = 0; % damage model = 0: exponential
           % -1: linear

if (dam == 1)

Da = Nc./Nf; % linear damage model
Dt = cumsum(Da); % damage accumulation

nir(counter,1) = ni;
Dtr(counter,1) = Dt(end);

else

Ne = zeros(1,length(r));
Dt = zeros(1,length(r));

for j = 1:length(r)-1;
Dt(j) = (exp((Nc(j)+Ne(j))*C(j)))/ ... % non-linear damage model
        (exp(Nf(j)*C(j)));
Ne(j+1) = log(Dt(j)*exp(Nf(j+1)*C(j+1)))/C(j+1);
end
Dt = Dt';

nir(counter,1) = ni;
Dtr(counter,1) = Dt(j-1);

end

mean_Dtr(counter) = mean(Dtr);
std_Dtr(counter) = std(Dtr);

mean_Dtr(counter);

if (counter <= 2)
else

iter = counter-2;

% ----- Convergence Check ----- %

residual = abs(mean_Dtr(counter)-mean_Dtr(counter-1));
conv_val = (1e-3)*mean_Dtr(counter-1);

disp([' iter ---> ' num2str(iter,'%6.0f') ' '
      num2str(mean_Dtr(counter),'%6.5f') ' ' ...
      num2str(conv_val,'%6.5e') ' ' num2str(residual,'%6.5e') ])

if ( residual <= conv_val);
break
else
end

end
counter = counter + 1;

end
```

```
disp(' Damage iteration completed. ')
```

```
x1 = linspace(min(Dtr),max(Dtr),10);  
[n1,xout1] = hist(Dtr,x1);
```

```
figure(1);  
bar(x1,n1,'b')  
hold on;  
p4 = plot(mean_Dtr(end)*[1 1],max(n1)*[0 1],'g-');  
set(p4, 'LineWidth', 1.0, 'MarkerSize', 6, 'MarkerFaceColor', 'w' );  
axis([min(Dtr) max(Dtr) 0 max(n1)+1])
```

```
% ----- Plot ----- %
```

```
figure(1);  
p0 = plot(1:1:length(mean_Dtr),mean_Dtr,'bo', [0 length(mean_Dtr)], ...  
mean_Dtr(end)*[1 1], 'r--');  
set(p0, 'LineWidth', 1.0, 'MarkerSize', 6, 'MarkerFaceColor', 'w' );  
axis([0 length(mean_Dtr)+1 0 1.2])
```

```
% ----- End ----- %
```